



## **Terms and Conditions of Use of Digitised Theses from Trinity College Library Dublin**

### **Copyright statement**

All material supplied by Trinity College Library is protected by copyright (under the Copyright and Related Rights Act, 2000 as amended) and other relevant Intellectual Property Rights. By accessing and using a Digitised Thesis from Trinity College Library you acknowledge that all Intellectual Property Rights in any Works supplied are the sole and exclusive property of the copyright and/or other IPR holder. Specific copyright holders may not be explicitly identified. Use of materials from other sources within a thesis should not be construed as a claim over them.

A non-exclusive, non-transferable licence is hereby granted to those using or reproducing, in whole or in part, the material for valid purposes, providing the copyright owners are acknowledged using the normal conventions. Where specific permission to use material is required, this is identified and such permission must be sought from the copyright holder or agency cited.

### **Liability statement**

By using a Digitised Thesis, I accept that Trinity College Dublin bears no legal responsibility for the accuracy, legality or comprehensiveness of materials contained within the thesis, and that Trinity College Dublin accepts no liability for indirect, consequential, or incidental, damages or losses arising from use of the thesis for whatever reason. Information located in a thesis may be subject to specific use constraints, details of which may not be explicitly described. It is the responsibility of potential and actual users to be aware of such constraints and to abide by them. By making use of material from a digitised thesis, you accept these copyright and disclaimer provisions. Where it is brought to the attention of Trinity College Library that there may be a breach of copyright or other restraint, it is the policy to withdraw or take down access to a thesis while the issue is being resolved.

### **Access Agreement**

By using a Digitised Thesis from Trinity College Library you are bound by the following Terms & Conditions. Please read them carefully.

I have read and I understand the following statement: All material supplied via a Digitised Thesis from Trinity College Library is protected by copyright and other intellectual property rights, and duplication or sale of all or part of any of a thesis is not permitted, except that material may be duplicated by you for your research use or for educational purposes in electronic or print form providing the copyright owners are acknowledged using the normal conventions. You must obtain permission for any other use. Electronic or print copies may not be offered, whether for sale or otherwise to anyone. This copy has been supplied on the understanding that it is copyright material and that no quotation from the thesis may be published without proper acknowledgement.

# Spin Valves and their Application

by

**Emma Kerr**

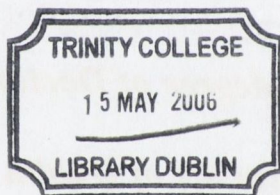
*A thesis submitted for the degree of Doctor of Philosophy in the  
University of Dublin*

Department of Physics

Trinity College Dublin

2006





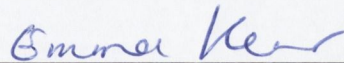
THESIS  
7800

## **Declaration**

This thesis is submitted by the undersigned for examination for the degree of Doctor of Philosophy at the University of Dublin. It has not been submitted as an exercise for a degree at any other university.

This thesis, apart from the advice, assistance and joint effort mentioned in the acknowledgments and in the text, is entirely my own work.

I agree that the library may lend or copy this thesis freely on request.

A handwritten signature in blue ink, appearing to read 'Emma Keir', is written above a horizontal line.

2006



## Summary

The discovery of giant magnetoresistance (GMR) in the late 1980's resulted in massive interest in the deposition and characterisation of artificial layered magnetic structures. Spin valves were discovered in 1991 and have been the subject of intense interest due to their suitability for application in magnetoresistive read heads in magnetic hard disk drives. The basic element of a spin valve is two ferromagnetic layers separated by a non-magnetic spacer. The electrical resistance of the structure is low when the magnetisation directions of the ferromagnetic layers are aligned parallel and high when they are antiparallel. One of the ferromagnetic layers, the free layer, switches magnetisation direction close to zero field. The other layer, the pinned layer, is grown next to an antiferromagnet and its magnetisation direction is pinned at low fields. Switching of the free layer at low fields, therefore, results in a transition from the parallel to antiparallel state and a linear change in resistance. Hence the spin valve is a highly sensitive magnetic field sensor and can be used in several applications. Spin valves can also be considered as one of the fundamental building blocks necessary for developing more complicated spin electronic devices.

In this work, several aspects of spin valves have been investigated. Chapter 1 is an introduction to spin valves and describes the fundamental physical principles involved as well as the main applications. Chapter 2 describes the experimental techniques used in this work to deposit, characterise and pattern spin valves.

In Chapter 3, the characterisation of top-pinned IrMn spin valves using polarized neutron reflectometry is presented. This powerful technique allowed precise determination of the spin valve layer thicknesses and magnetic moments to be determined. In addition, the stability of the pinned layer as a function of applied field and temperature has been assessed. This suitability of these structures for sensor applications is discussed.



In general, spin valves require a post-deposition magnetic anneal to establish exchange bias. Chapter 4 presents a study of the effect of the strength of the magnetic annealing field on parameters such as exchange bias and GMR in spin valve structures. A specifically designed furnace allowed magnetic annealing of spin valves to be performed in a superconducting magnet at fields up to 5.5 T. A magnetic field effect was found in bottom pinned structures and is discussed in terms of a re-alignment of the IrMn pinned spin moment.

Interest in patterning magnetic nanostructures using the Focussed Ion Beam (FIB) has increased in recent years. However, implantation of  $\text{Ga}^+$  ions from the beam can have adverse effects on the magnetic and electrical properties of magnetic thin films and multilayers. In chapter 5, the effects of  $\text{Ga}^+$  ion implantation in IrMn spin valves is presented and the feasibility of using FIB milling as a tool for nano-patterning spin valves assessed.

Finally, an interesting application of a spin valve is presented in Chapter 6. The mixed sensor consists of a superconducting loop with a micron-sized constriction. A spin valve sensor is deposited above or below the constriction. In perpendicular applied fields, supercurrents in the loop create a locally enhanced in-plane magnetic field above the constriction. This field can be detected by the spin valve. The optimisation of the spin valve structure for this specific application is discussed and results for a mixed sensor prototype presented. The sensitivity of the prototype is comparable to that of high  $T_c$  SQUIDS. Possible applications are discussed.

## Acknowledgements

I would like to thank Prof. Coey for giving me the opportunity to work in his group and for his supervision and guidance during the last four years. Even with his hectic schedule, he always makes time to see his students. I was also lucky enough to have Sebastiaan van Dijken on hand who provided guidance on a daily basis. His expertise, both in the lab and with writing up was a huge help. During my work I was involved in collaboration with Claude Fermon and Myriam Pannetier in Paris. It was a great experience for me to be involved with this work and to visit another lab. Thanks for the hospitality and for the help with the write-up. Thanks also to Frederic Ott for his help with the neutron work.

Thanks to all the people who have passed through the CINSE lab and improved it on their way: Steve Sebastien, Jerome and Kentaro for example. Thanks to Mazhar for all work in keeping the CINSE lab going and to Venki, who keeps everything running smoothly on the other side. And to the current group members, Richard for his help with the FIB, Plamen, Lucio, Fernando, Greg, Adriele, Chris, Cathy, Matt, Gen Feng, Eoin, Robbie, Karl, Zhu and everybody in the group. And to past members like Ciara, Oscar and Cora. The technical and administrative teams play a huge role in the day to day running of the lab. Thanks to Jackie, John Kelly, Joe, Ken, Nigel, Mick, Dave, Ciaran Clinton while he was there and now Mike Finneran for all the technical support. Thanks to Tracey, Susan and Sandra for all the administrative support. Thanks to everyone at SFI. Thanks to all the friends who helped me along the way. To Ken and Greg for all the coffee breaks and pints. All the girls from Wicklow for supportive e-mails and non-physics weekends. To Dave and all that gang for dinners and nights out in Dublin. Special thanks to Rowena, Ruairi and Roisin for encouragement and for all leaving the country! Thanks to my parents for everything they have done for me. Thanks to Ronan for looking after me.



# Table of Contents

## Chapter 1

Introduction .....	10
1.1 Spin Electronics .....	10
1.2 Giant Magnetoresistance.....	11
1.3 Spin valve structures.....	17
1.3.1 Interlayer coupling in spin valves.....	20
1.4 Exchange bias .....	22
1.4.1 Exchange bias materials and properties.....	28
1.5 Spin valve designs .....	31
1.6 Spin valves devices.....	34
1.6.1 Spin valves as magnetic-field sensors .....	36
1.6.2 Spin valves in read heads.....	37
1.6.3 Spin valves in MRAM .....	40
1.7 References.....	41

## Chapter 2

Experimental Techniques.....	45
2.1 Magnetron sputtering in the Shamrock Deposition Tool.....	45
2.1.1 Magnetron Sputtering .....	45
2.1.2 The Shamrock .....	46
2.2 Magnetoresistance measurements.....	51
2.3 Noise Measurements.....	51
2.4 Superconducting Quantum Interference Device (SQUID).....	52
2.5 Magnetic annealing.....	52
2.6 X-ray Diffraction .....	54
2.7 Polarised Neutron Reflectometry.....	56
2.7.1 Principles of neutron reflectivity .....	56
2.7.2 Neutron-matter interaction.....	57
2.7.3 Reflectivity on Non-Magnetic Systems .....	58
2.7.4 Neutron reflectivity on magnetic systems .....	60
2.7.5 Interaction of the neutron with a magnetic layer .....	61
2.7.6 The PRISM Spectrometer .....	63



2.8	Fabrication of small magnetic structures .....	65
2.8.1	Optical Lithography .....	65
2.8.2	Focused Ion Beam (FIB) tool .....	69
2.9	References.....	72

### Chapter 3

Characterisation of Spin Valves using Polarized Neutron Reflectometry .....		73
3.1	Introduction.....	73
3.2	Structural and magnetic characterisation of spin valves.....	74
3.2.1	Deposition and Magnetotransport.....	74
3.2.2	Structural characterisation using X-Ray Reflectometry .....	75
3.2.3	Structural and magnetic characterisation using PNR .....	77
3.2.4	Measurement of the spin valve thermal stability .....	81
3.3	Conclusion .....	86
3.4	References.....	87

### Chapter 4

Influence of the Annealing Field Strength on Exchange Bias and Magnetoresistance of Spin Valves with IrMn .....		88
4.1	Introduction.....	88
4.2	As-deposited spin valves .....	91
4.3	Influence of the annealing temperature .....	95
4.4	Influence of the annealing field .....	101
4.5	Conclusion .....	108
4.6	References.....	109

### Chapter 5

Effects of Ga <sup>+</sup> ion implantation on the magnetoresistive properties of spin valves with IrMn .....		111
5.1	Introduction.....	111
5.2	Direct implantation of Ga <sup>+</sup> ions .....	113
5.3	Ga <sup>+</sup> ion implantation during FIB milling.....	120

5.4	Conclusion .....	123
5.5	References.....	124

## Chapter 6

Femtotesla Magnetic field Measurement with a Spin Valve Sensor .....		125
6.1	Introduction.....	125
6.2	Design of the spin valve element of the mixed sensor .....	128
6.2.1	Noise in spin valves .....	128
6.2.2	Spin valve design .....	129
6.2.3	Spin valve sensitivity .....	132
6.3	The principle of the mixed sensor device .....	133
6.4	Sample preparation .....	136
6.5	Femtotesla resolution with an YBCO-spin valve mixed sensor .....	138
6.6	Femtotesla resolution with a Nb-spin valve mixed sensor .....	141
6.7	Conclusion .....	143
6.8	References.....	145

## Chapter 7

Conclusions and Future Work.....		147
Publications.....		151



## Table of Figures

### Chapter 1

Figure 1.1	The original GMR observation of GMR in (Fe/Cr) <sub>n</sub> multilayers by Baiblich et al [3] reporting GMR effects of up to 45% requiring saturating fields of up to 2T.....	11
Figure 1.2	Density of states of transition metals Fe, Co, Ni and Cu from [] .....	13
Figure 1.3	Resistor model of GMR.....	14
Figure 1.4	Current in plane (left) and current perpendicular to plane (right) GMR geometries.....	16
Figure 1.5	Schematic of magnetisation (left) and magnetoresistance (right) of a pseudo spin valve .....	18
Figure 1.6	Magnetoresistance (top) and magnetisation (bottom) of an exchange biased spin valve. ....	19
Figure 1.7	Free layer reversal of a spin valve. ....	20
Figure 1.8	Schematic showing ferromagnetic magnetostatic Néel coupling between two ferromagnetic layers separated by a non-magnetic spacer. ....	21
Figure 1.9	Hysteresis of Co/CoO particles measured at 77 K after cooling under a magnetic field of 1 T (1) and zero field (2) [22].....	23
Figure 1.10	Phenomenological description of exchange bias .....	24
Figure 1.11	Magnetotransport curve of SAF spin valve with stack composition shown.... .....	33
Figure 1.12	Spin valve deposited with crossed anisotropy (a) and parallel anisotropy (b) .....	35
Figure 1.13	Schematic cross section of a vertical read -head above a storage recording medium .....	38



## Chapter 2

Figure 2.1	Cross section schematic of the S-Gun magnetron .....	46
Figure 2.2	The shamrock sputtering tool in the CINSE class 1000 cleanroom .....	47
Figure 2.3	Schematic of the shamrock .....	48
Figure 2.4	Schematic of turntable showing planetary motion (left) and substrate planet with integrated magnetic array (right) .....	49
Figure 2.5	Four point magnetoresistance measurement.....	51
Figure 2.6	Cross-section schematic of magnetic furnace inside superconducting 5.5 T Cryogenics magnet .....	53
Figure 2.7	Schematic of XRR set-up .....	55
Figure 2.8	Reflectivity curve with fit for a Au film of thickness 53nm.....	56
Figure 2.9	Schematic of axis notation used for reflection from a surface .....	58
Figure 2.10	Neutron reflectivity from a perfect silicon surface [6]. .....	60
Figure 2.11	Up and down reflectivities on a nickel thin film [6].....	62
Figure 2.12	Schematic of the experimental set-up: (a) top view, (b) side view. The different elements are: multilayer monochromator (M), deviator guide (D), focusing guide (C), collimation slits (S1-S4), flippers (F1 and F2), transmission polarizer (P) and reflection analyzer (A). Fabrication of small magnetic structures .....	64
Figure 2.13	Six steps involved in the standard patterning procedure .....	67
Figure 2.14	5 steps for lift-off procedure .....	68
Figure 2.15	The dual beam FIB tool in the Class 1000 cleanroom.....	70

## Chapter 3

Figure 3.1	Free layer reversal of crossed anisotropy spin valve structure Ta(5nm)/NiFe(3.5nm)/CoFe(1.2nm)/Cu(2.9nm)/CoFe(2.5nm)/IrMn(10nm)/ Ta(10nm) .....	50
Figure 3.2	XRR curve with fit of spin valve structure .....	51
Figure 3.3	Schematic showing spin valve measurement configuration for $R^{++}$ and $R^{-}$ intensities for free and pinned layer parallel (left) and free and pinned layer antiparallel (right). .....	52
Figure 3.4	Reflectivity curves for spin valve with $t_{\text{NiFe}} = 2\text{nm}$ in the parallel (a) and anti-parallel (b) configuration. Red squares $R^{++}$ , blue squares $R^{-}$ , best fit in red and blue lines. Table showing spin valve structure as determined by fits to the reflectivity curves. ....	52
Figure 3.5	Reflectivity curves for spin valve with $t_{\text{NiFe}} = 2\text{nm}$ in the parallel (a) and anti-parallel (b) configuration. Red squares $R^{++}$ , blue squares $R^{-}$ , best fit in red and blue lines. Table showing spin valve structure as determined by fits to the reflectivity curves. ....	53
Figure 3.6	Reflectivity curves for spin valve with $t_{\text{NiFe}} = 5\text{nm}$ in the parallel (a) and anti-parallel (b) configuration. Red squares $R^{++}$ , blue squares $R^{-}$ , best fit in red and blue lines. Table showing spin valve structure as determined by fits to the reflectivity curves. ....	54
Figure 3.7	Schematic showing spin valve configuration for spin flip measurement ....	55
Figure 3.8	Spin valve reflectivity with spin flip for $t_{\text{NiFe}} = 3.5\text{nm}$ at room temperature with a 1.3mT applied field. ....	56
Figure 3.9	Rocking curves of the spin flip maximum as a function of temperature .....	58
Figure 3.11	Reflectivity curves for spin valve heated at 185°C overnight. ....	59



## Chapter 4

Figure 4.1	Spin-valve structures: (a) top spin valve (TSV), (b) bottom spin valve (BSV), (c) synthetic antiferromagnetic top spin valve (SAFTSV), and (d) synthetic antiferromagnetic bottom spin valve (SAFBSV). ....	91
Figure 4.2	Magnetotransport and SQUID magnetisation curves for the as-deposited TSV ((a) and (b)) and BSV ((c) and (d)) structure. ....	92
Figure 4.3	Magnetotransport and SQUID magnetisation curves for the as-deposited SAFTSV [(a) and (b)] and SAFBSV [(c) and (d)] structures. ....	93
Figure 4.4	Annealing temperature dependence of the exchange bias field (a) and MR (b) of the TSV and BSV structure. The annealing field was 5.5 T. The filled symbols indicate the as-deposited values. ....	97
Figure 4.5	Magnetotransport curves for SAFTSV (a) and SAFBSV (b) as-deposited and after annealing at 210 °C in a field of 5.5 T. ....	99
Figure 4.6	Annealing temperature dependence of the exchange bias field (a) and MR (b) of the SAFTSV and SAFBSV structures. The annealing field was 5.5 T. The filled symbols indicate the as-deposited values. ....	100
Figure 4.7	Normalized magnetisation and magnetotransport curves for the TSV structure before and after annealing in different magnetic fields. ....	101
Figure 4.8	Normalized magnetisation and magnetotransport curves for the BSV structure before and after annealing in different magnetic fields. ....	102
Figure 4.9	Annealing field strength dependence of the exchange bias field (a) and MR (b) of the TSV and BSV structure. The annealing temperature was 210 °C. The filled symbols indicate the as-deposited values. ....	103
Figure 4.10	Annealing field strength dependence of the exchange bias field (a) and MR (b) of the SAFTSV and SAFBSV structure. The annealing temperature was 210 °C. The filled symbols indicate the as-deposited values. ....	107



## Chapter 5

Figure 5.1	Magnetoresistance and magnetisation curves for the as-deposited spin valve structure. ....	114
Figure 5.2	Magnetoresistance of implanted spin valves .....	115
Figure 5.3	spin valve resistance (filled symbols) and magnetoresistance (open symbols) as a function of ion dose (lines are guides to the eye). ....	116
Figure 5.4	Normalised exchange bias field as a function of ion dose.....	117
Figure 5.5	TRIM simulation showing 30 keV Ga <sup>+</sup> ion distribution throughout the spin valve structure.....	117
Figure 5.6	Normalised MR and $\Delta R$ as a function of ion dose (line is a guide). ....	119
Figure 5.7	SEM of spin valve lines FIB milled to different widths. ....	120
Figure 5.8	Magnetoresistance of FIB milled spin valves with line widths ranging from 10 $\mu\text{m}$ to 0.5 $\mu\text{m}$ . ....	121
Figure 5.9	(a) Resistance (b) $\Delta R$ and (c) magnetoresistance as a function of 1/linewidth for FIB milled spin valves .....	122

## Chapter 6

Figure 6.1	Spin valves patterned into a yoke device (left) and a short-circuited meander (right). ....	130
Figure 6.2	Resistance and MR ratio of the free layer reversal of a spin valve yoke...	130
Figure 6.3	Magnetic configuration of a yoke after saturation and reversal to zero magnetic field as obtained from micromagnetic simulations. ....	131
Figure 6.4	1/f noise in a spin valve yoke at room temperature with a sensing current of 3 mA at different external applied fields. ....	132

Figure 6.5	Schematic of the superconducting loop when an external perpendicular field is applied. The supercurrent (white arrows) generates a high density of field lines with an in-plane component at the position of the constriction. The spin valve sensor is placed immediately above or below the constriction. 133
Figure 6.6	Schematic views of YBCO mixed sensor device. (A) Schematic showing YBCO superconducting loop with yoke-shaped spin valve sensor and four contacts for measurement. (B) Optical micrograph of the constricted area of the loop under the active part of the spin valve. (C) Cross-section of the spin valve stack showing the in-plane components of the field created by the YBCO flux-to field transformer. (D) Cross-section of the device showing electrical isolation of the spin valve and the contacts from the loop by the Si <sub>3</sub> N <sub>4</sub> layer..... 135
Figure 6.7	Schematic of patterning process for the YBCO-based mixed sensor device. . ..... 137
Figure 6.8	Magnetoresistance of the spin valve yoke of an YBCO-based mixed sensor at 4.2 K..... 138
Figure 6.9	Magnetoresistance ratio as a function of temperature. .... 139
Figure 6.10	Magnetoresistance as a function of perpendicular applied field at 4.2 K on the YBCO device. The inset shows the gain as a function of temperature. ..... 140
Figure 6.11	Noise spectra of the YBCO mixed sensor at 4.2K and 77K with 15 mA and 5 mA of sensing current respectively. .... 141
Figure 6.12	Magnetoresistance as a function of perpendicular applied field at 4.2 K for the Nb based mixed sensor. .... 142
Figure 6.13	Noise spectra of the Nb device at 5 K with 0 mA and 1 mA sensing current. ..... 143



# Chapter 1

## Introduction

### 1.1 Spin Electronics

Over the last ten years, Spin Electronics has become an exciting area of research and development combining the two traditional areas of magnetism and electronics. Conventional electronics is based on manipulating and controlling a current flow by applying an electric field, which acts as a force on the charge of electrons. Another interesting property of the electron is its spin. This is an intrinsic property resulting from the fact that the electron behaves as if it were spinning on its own axis thereby creating a magnetic moment. This spin angular momentum is quantized and can take only two values:  $+\hbar/2$  (spin up) and  $-\hbar/2$  (spin down), where  $\hbar$  is Planck's constant. Non-magnetic materials have equal numbers of spin up and spin down electrons. In contrast, in ferromagnetic materials the density of states is different for each of the two spin configurations resulting in a net spin polarization of the electron current. Spin electronics uses the electron spin as the active element manipulated in transport processes with the aim of developing new devices as well as magnetic versions of conventional electronic devices [1, 2].

## 1.2 Giant Magnetoresistance

In the last thirty years, huge technological advances have been made in the fields of thin films deposition and materials preparation. This has allowed development of a wealth of artificially constructed multilayer systems combining magnetic, non-magnetic, semiconducting and superconducting materials. In 1988 Fert and co-workers [3] and Grünberg and co-workers [4] independently discovered that the resistance of a multilayer structure comprised of alternating nanometer films of Fe and Cr changed in a magnetic field (Figure 1.1). The change in resistance involved was orders of magnitude bigger than conventional anisotropic magnetoresistance observed in single films of magnetic material (typically 3% in permalloy). Hence the phenomenon was termed Giant Magnetoresistance or GMR.

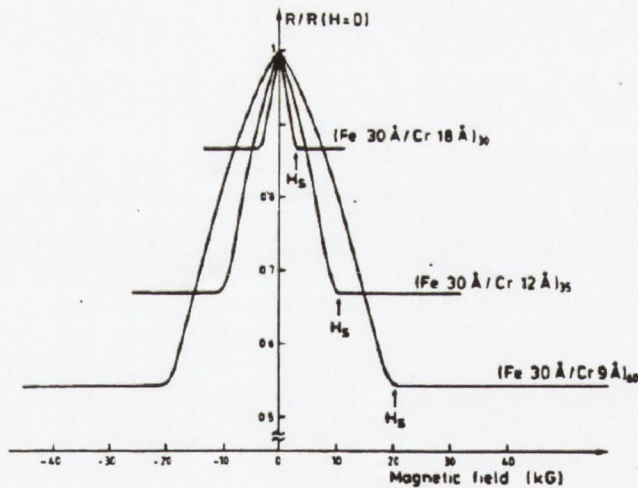


**Figure 1.1** The original GMR observation of GMR in (Fe/Cr)<sub>n</sub> multilayers by Baiblich et al [3] reporting GMR effects of up to 45% requiring saturating fields of up to 2T.



The magnetoresistance (MR) ratio is defined as:

$$\frac{\Delta R}{R} = \frac{R_{AP} - R_P}{R_P} \quad (1.1)$$

where  $R_{AP}$  and  $R_P$  are the resistances in states where the alternate ferromagnetic layers are aligned with their magnetisations antiparallel and parallel, respectively. Later, an MR ratio of 110 % at room temperature was reported for sputter deposited [110]-oriented antiferromagnetically coupled  $\text{Co}_{95}\text{Fe}_5/\text{Cu}$  superlattices [5] and an MR of 220 % at 1.5K was reported for Fe/Cr multilayers [6].

In order to understand the GMR effect we must first consider the band structure of a ferromagnetic transition metal. The electrons participating in conduction can be distinguished as two types depending on the direction of their spin along the local magnetisation axis. Spin up electrons conventionally have their spin aligned parallel to the local magnetisation and vice versa. Spin up and spin down electrons are often described as majority and minority. The two-current model introduced by Mott [7] considers that these two types of electrons carry independent electrical current in parallel, assuming that spin-flip scattering does not occur. Figure 1.2 shows the density of states (DOS) of Fe, Co Ni and Cu. The DOS can be viewed as a superposition of a narrow sp-band and a wide d-band. A normal metal such as Cu has equal density of spin up and spin down electrons at the Fermi level. A ferromagnet however, has a spin split density of states at the Fermi level. For Co and Ni, the majority d-band is fully occupied and is situated below the Fermi level, whereas the minority spin band is only partially occupied. This spin splitting results in very different scattering rates for spin up and down electrons at the Fermi level as there is a difference in the density of available states into which the electrons can be scattered. This leads to different resistivities for spin up and spin down electrons as described by the spin scattering asymmetry:

$$\alpha = \frac{\rho_{\downarrow}}{\rho_{\uparrow}} \quad (1.2)$$

where  $\rho_{\uparrow}$  and  $\rho_{\downarrow}$  are the resistivities of majority and minority electrons. For example, for the ferromagnetic elements Co, Ni and Fe,  $\alpha > 1$ . This means that spin down electrons are scattered more heavily than spin up electrons in these materials, on account of the empty spin down d-states.

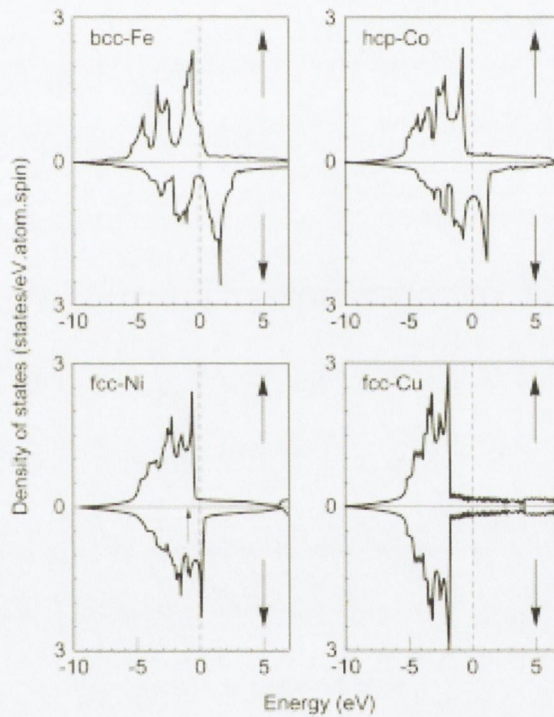


**Figure 1.2** Density of states of transition metals Fe, Co, Ni and Cu from [8]

The GMR effect can be understood by considering these spin dependent scattering effects. Consider two ferromagnetic layers separated by a non-magnetic spacer layer as shown in Figure 1.3. The magnetisation of the two magnetic layers can either be aligned parallel or antiparallel. Both spin up and spin down electrons flow through the stack and can be considered as two independent channels. In the parallel configuration, spin up electrons



are not scattered in either magnetic layer and have low resistivity. Similarly, spin down electrons are scattered heavily in both magnetic layers and have high resistivity. The lower resistivity of the spin up channel effectively gives a short circuit and the overall resistance of the stack is low. In the antiparallel configuration, spin up electrons have low resistivity in one magnetic layer and high resistivity in the second layer. Spin down electrons experience the opposite effect so that both types of electrons are scattered and the overall resistance of the stack is high. If we assume that the mean free paths of the electrons are larger than the layer thicknesses, then the resistor model in Figure 1.3 can be used to describe the situation.

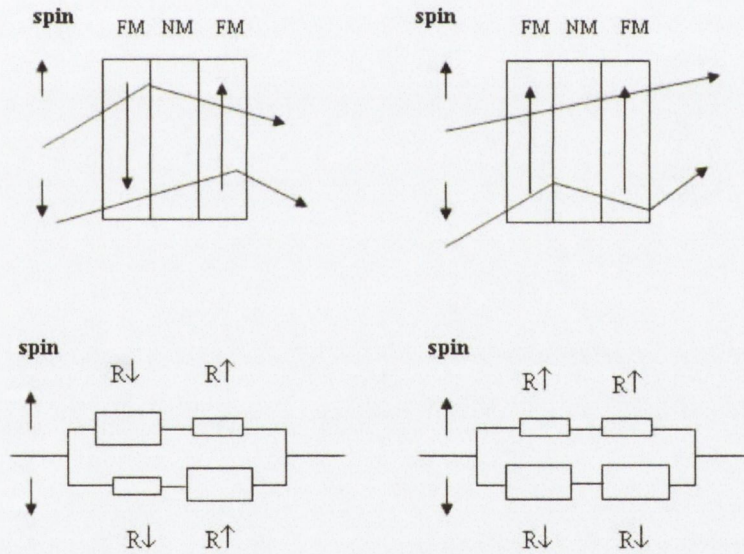


**Figure 1.3 Resistor model of GMR**

In the parallel configuration the resistivity is given by:

$$R_p = \frac{R_\uparrow R_\downarrow}{R_\uparrow + R_\downarrow} \tag{1.3}$$

while in the antiparallel configuration it is described by:

$$R_{AP} = \frac{R_{\uparrow} + R_{\downarrow}}{4} \quad (1.4)$$

The GMR ratio is then given by:

$$\frac{\Delta R}{R} = \frac{R_{AP} - R_p}{R_p} = \frac{(1 - \alpha)^2}{4\alpha} \quad (1.5)$$

This illustrates the importance of the scattering asymmetry in the origin of GMR. Scattering at interfaces in multilayer structures also plays an important role and depends on the degree of matching of the electronic band structures of the ferromagnetic and non-magnetic materials in the bulk of the layers and near the interfaces. In order to obtain a large GMR effect, good electronic structure matching is required for one spin direction and bad matching for the other direction. Good electronic structure matching explains, in part, the large GMR ratios for Fe/Cr multilayers where matching is good for the minority electrons and for Co/Cu where good matching occurs for the majority spin electrons [9]

There are two ways in which the current can flow through a GMR stack; parallel to the plane of the film or perpendicular to the plane. These two configurations are known as current in plane (CIP) and current perpendicular to plane (CPP) (Figure 1.4). The simple model discussed above assumes that the current densities are homogenous for both spin directions throughout the layers. This isn't valid for the CIP geometry and is generally more applicable to CPP which is described in detail by the Valet Fert model [10]. There is a fundamental difference between the important length scales in the two geometries. In the case of CIP GMR, the electric field is uniform along the in-plane direction. It is important then that the mean free path of the spin up and spin down electrons is much larger than the thicknesses of the layers. The electrons will then, on average, traverse many layers



without being scattered as they drift along the in-plane direction and the resistance contributed by each spin channel will be proportional to the scattering rate for each channel. This is the case in Co/Cu multilayers for example where the antiferromagnetic coupling is realized at a Cu layer thickness of about 0.85 nm and the majority mean free path in Co is around 5nm and Cu is about 30nm [11]. In CPP GMR, the electric field created by the current will ensure that electrons are pushed across the non magnetic spacer towards the next magnetic layer. The important length scale here then is the spin diffusion length. This describes the distance an electron can travel without flipping its spin. It is important that the spacer layer is thinner than this distance so that electrons retain their spin configurations between successive magnetic scattering events. In addition, because electrons are forced to traverse the interfaces there is an additional spin-dependent interfacial resistance in CPP GMR resulting from the difference in the positions of the bottoms of the conduction bands with respect to the Fermi energy in successive layers. CPP GMR is usually much higher than CIP GMR. However applications have generally avoided the CPP geometry thus far due to the technical challenges of making CPP pillars of small enough dimensions such that the resistance is appreciable.

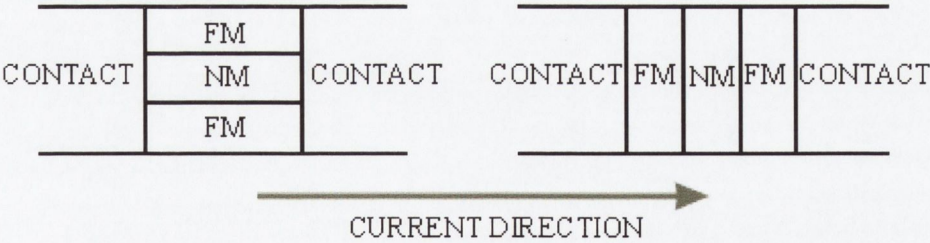


**Figure 1.4** Current in plane (left) and current perpendicular to plane (right) GMR geometries.

Semi-classical theories have been developed to model GMR in magnetic multilayers. The CIP transport properties of magnetic multilayers are calculated using an adaptation of the Boltzmann theory using spin-dependent resistivities of the materials and the spin dependent interfacial resistances as input parameters. These theories have proven successful in explaining most of the general transport trends in multilayers and spin valves such as the dependence of GMR on the thicknesses of the various layers and also the effects of specular reflection. A detailed description of these theories is beyond the scope of this introduction. A comprehensive review can be found in [12].

Multilayer systems can have high GMR ratios but are not well suited for applications. The coupling in these multilayers oscillates from ferromagnetic to antiferromagnetic as a function of the spacer layer thickness. This thickness is engineered such that the layers are coupled antiferromagnetically at zero field. This coupling is so strong however, that it takes a rather large magnetic field (several hundred mT) to overcome it and get a change in resistance. This is unsuitable in applications such as read head sensors for example, which are exposed to fields of the order 10mT. Another disadvantage is the non-linearity of the resistance change, making the multilayer system less useful for sensor applications. These constraints led to the development of the spin valve sensor in 1991 [13] as discussed in the next section.

### 1.3 Spin valve structures

The basic spin valve element consists of two magnetic layers separated by a non-magnetic spacer. The device is engineered such that the ferromagnetic layers can be switched from parallel to antiparallel in a controlled and independent manner. Parallel alignment is achieved by the application of a magnetic field. Antiparallel alignment can be realized by



several different techniques. Perhaps the most obvious method is to use ferromagnetic layers with different coercive fields. This can be done by using a magnetically hard and magnetically soft layer as the ferromagnetic electrodes such as:

NiFe(3nm)/Cu(5nm)/Co(3nm)/Cu(5nm) [14]. These systems are often called pseudo spin valves and an example of a magnetisation and magnetoresistance curve is shown in Figure 1.5. The pseudo spin valve has a symmetric and irreversible response of the resistance with field. Again, this is a disadvantage for applications in sensors and magnetoresistive heads. However pseudo spin valves have been studied for application in GMR MRAM (magnetic random access memory) architecture.

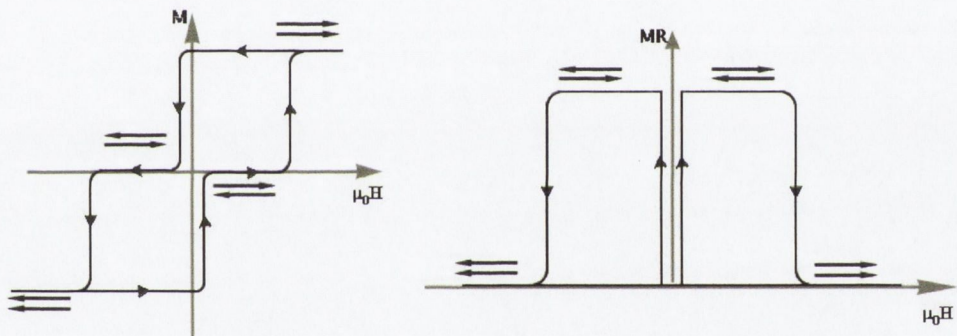


**Figure 1.5 Schematic of magnetisation (left) and magnetoresistance (right) of a pseudo spin valve**

A more useful configuration is the exchange biased spin valve. In its basic form it has the structure FM1/NM/FM2/AFM where FM1 and FM2 are ferromagnetic layers, NM is a non-magnetic spacer and AFM is an antiferromagnetic layer that pins the magnetisation of the adjacent FM layer using the so-called exchange anisotropy phenomenon (section 1.4). In this configuration, FM1 is termed the free or soft layer and FM2 the pinned or hard layer. Figure 1.6 shows the room temperature magnetisation and magnetoresistance of a spin valve of structure:

Ta5nm/NiFe3.5nm/CoFe1.5nm/Cu2.9nm/CoFe2.5nm/IrMn10nm/Ta5nm.

The magnetisation curve of this sample consists of two hysteresis loops. At high negative fields both free and pinned layers are aligned parallel with the field. At close to zero field, the free layer (NiFe3.5/CoFe1.5nm) switches antiparallel to the pinned layer. The pinned layer (CoFe2.5nm) does not switch until the exchange anisotropy is overcome at 35mT, the so-called exchange bias field. In the magnetoresistance curve, at high negative fields both layers are parallel and the resistance is low. At close to zero field the free layer switches sharply to the antiparallel configuration and the resistance reaches a maximum. As the field is further increased, the pinned layer gradually switches and the resistance decreases to the minimum value.

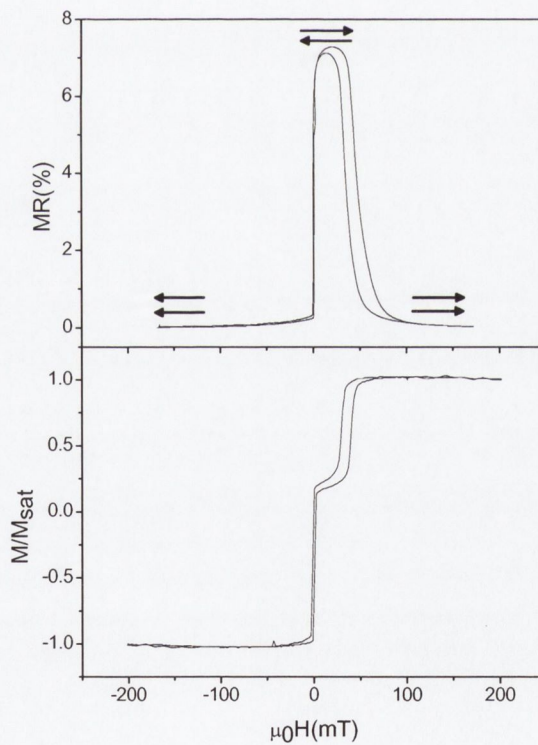


**Figure 1.6 Magnetoresistance (top) and magnetisation (bottom) of an exchange biased spin valve.**



### 1.3.1 Interlayer coupling in spin valves

The change in the relative orientation between the magnetisation in the free and pinned layers in an exchange biased spin valve does not rely on the existence of antiferromagnetic coupling through the spacer. The unidirectional exchange anisotropy of the pinned layer means that the two FM layers switch independently. Figure 1.7 shows the reversal of the free layer. This illustrates the advantage of the exchange-biased spin valve, with high magnetoresistance and sensitivity at low fields it is ideal for sensor applications. The loop shift in the free layer indicates the presence of a slight ferromagnetic coupling through the Cu spacer layer. The three main contributions to this coupling are direct coupling through pinholes, Néel or orange-peel coupling and oscillatory RKKY (Ruderman-Kittle-Kasuya-Yosida) coupling.

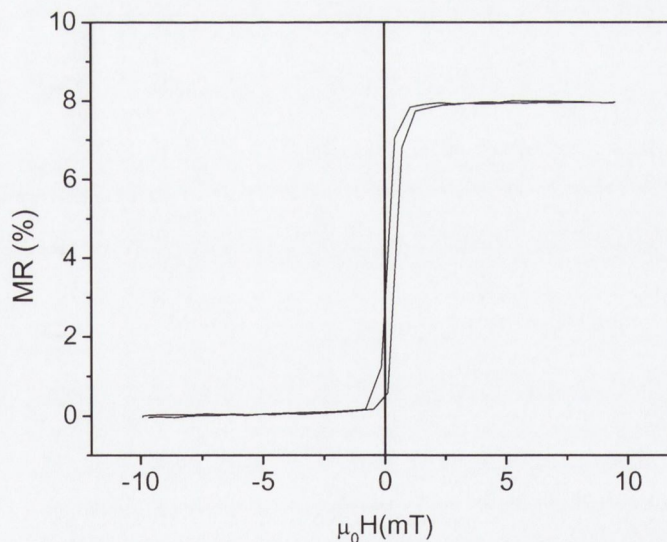


**Figure 1.7** Free layer reversal of a spin valve.

Direct coupling through pinholes in the non-magnetic spacer layer can occur at low spacer layer thickness. This ferromagnetic coupling can result in loss of independent switching of

the free and pinned layers. The critical thickness below which this coupling occurs depends on the roughness of the layers and the degree of interdiffusion between the magnetic and non-magnetic spacer. Buffer layers such as Ta or NiFeCr are used in spin valve stacks to reduce this effect.

Néel or orange peel coupling [15] occurs because the roughness of the interfaces in multilayers is correlated from one interface to another. There is no dipolar coupling between perfectly smooth, uniformly magnetized ferromagnetic layers because they create no stray field. However, rough surfaces do couple via dipolar fields. The resultant ferromagnetic dipolar coupling between the two magnetic layers separated by a non-magnetic spacer where the interfacial roughness,  $J$ , is described a sinusoidal function of amplitude  $h$  and wavelength  $L$  (Figure 1.8) is given by [16,17]:

$$J = \frac{\pi}{\sqrt{8}} \cdot \mu_0 \frac{h^2}{L} M_s^2 \exp\left(\frac{-2\pi \cdot t_{NM} \sqrt{2}}{L}\right) \quad (1.6)$$

where  $M_s$  is the saturation magnetisation of the magnetic layers and  $t_{NM}$  is the non-magnetic spacer layer thickness.

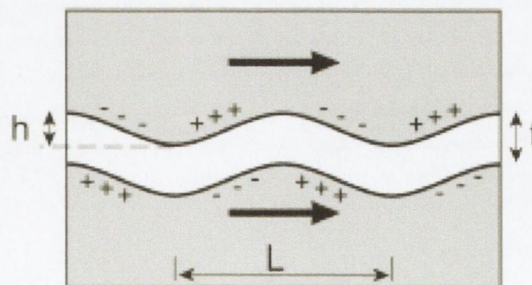


**Figure 1.8** Schematic showing ferromagnetic magnetostatic Néel coupling between two ferromagnetic layers separated by a non-magnetic spacer.



As mentioned in section 1.2, the exchange coupling in multilayer systems such as  $(\text{Co}/\text{Cu})_n$  oscillates from ferromagnetic to antiferromagnetic with the spacer layer thickness. This is the same as the RKKY coupling mechanism which describes the interaction between ferromagnetic impurities in a non-magnetic matrix [18]. This effect is pronounced in high quality multilayers. It has been shown that the GMR ratio also oscillates as a function of spacer thickness in these systems and the thickness of the NM layer can be chosen to coincide with antiferromagnetic coupling at zero field and high GMR [19]. In spin valves with only two magnetic layers separated by a non-magnetic spacer, an oscillation of the coupling as a function of the spacer thickness can be seen in high quality samples with low roughness. As the roughness increases the coupling becomes ferromagnetic as Néel coupling dominates [20]. Optimisation of the spin valve coupling mechanisms through optimisation of roughness and spacer layer thickness can therefore be used to adjust the offset of the free layer switching or the bias point. This is important from an applications point of view.

#### 1.4 Exchange bias

In 1956 Meiklejohn and Bean discovered the phenomenon of exchange anisotropy when studying ferromagnetic Co particles embedded in their native antiferromagnetic oxide CoO [21,22]. When the particles were cooled in a magnetic field from room temperature, where the CoO is paramagnetic, to 77K where it is antiferromagnetic, a unidirectional anisotropy appeared. The same treatment carried out on non-oxidised Co particles resulted in uniaxial anisotropy (Figure 1.9). This unidirectional anisotropy was attributed to exchange interaction between the AFM CoO particles and the FM Co core and was termed exchange anisotropy. The most notable manifestation of this phenomenon was the shift from zero field of the magnetisation loop of the sample.

Since then, exchange anisotropy has been observed in a wide variety of systems containing FM-AFM interfaces. A review of the experimental findings is given in [23]. The common features are the shift from zero field of the magnetisation curve by an amount known as the exchange bias field  $H_{ex}$ , an enhanced coercivity, and the disappearance of these features at temperatures above  $T_B$ , the blocking temperature of the AFM where  $T_B < T_N$ , the Néel temperature of the AFM.

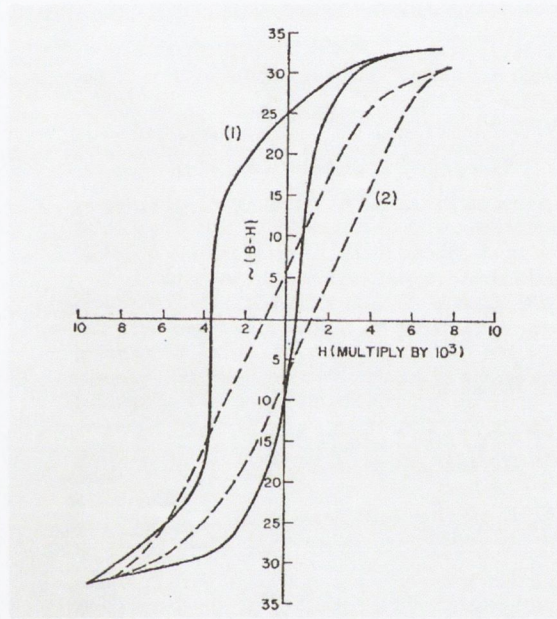


**Figure 1.9 Hysteresis of Co/CoO particles measured at 77 K after cooling under a magnetic field of 1 T (1) and zero field (2) [22].**

Meiklejohn and Bean explained the unidirectional anisotropy and exchange bias by considering a simple picture of the FM/AFM interface (Figure 1.10). In this case there is a ferromagnetic interaction at the interface and the magnetisations are aligned. The interface is non-compensated, i.e. only one type of antiferromagnetic spin is present at the interface and the magnetisation at the interface is non-zero. The interaction between at the FM/AFM interface tries to keep the magnetisations at the interface aligned and can be thought of as an effective field acting on the FM film. It is more energetically favourable



for the FM to be aligned along the direction of this effective field. During the hysteresis cycle, when the applied field is as shown in Figure 1.10, the FM spins remain aligned with the AFM until the applied field is greater than the sum of the effective field and the coercive field of the FM. In the second half of the hysteresis cycle, the applied field is now in the direction of the effective field and the FM will switch at a lower applied field value given by the difference between coercive field of the FM and the effective field. So the FM has only one stable configuration, as shown by unidirectional anisotropy and a shift from zero of the hysteresis cycle by a value corresponding to the exchange bias field,  $H_{ex}$ .

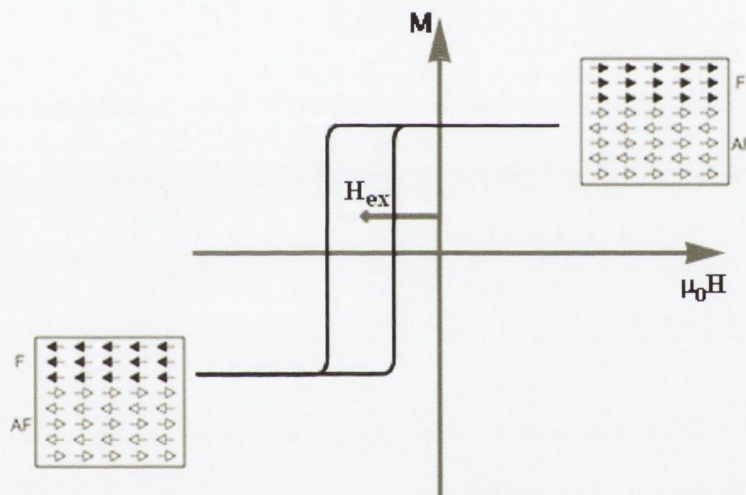


**Figure 1.10** Phenomenological description of exchange bias

The situation can be described analytically by minimizing the energy of the system. Consider a single domain FM film of thickness  $t_{FM}$ , saturation magnetisation,  $M_{FM}$  and uniaxial anisotropy  $K_{FM}$  in contact with a single domain AFM film of thickness  $t_{AFM}$ , and uniaxial anisotropy  $K_{AFM}$ . We assume the anisotropy axes are collinear and in the direction of the applied field and the coupling at the interface is ferromagnetic. The energy of the system is given by:

$$E = -HM_{FM}t_{FM} \cos \theta + K_{FM}t_{FM} \sin^2 \theta + K_{AFM}t_{AFM} \sin^2 \theta - J \cos \theta \quad (1.7)$$

The angle  $\theta$  is made between the magnetisations of the FM and AFM layers and their respective anisotropy axes, which are collinear. The first term is the Zeeman energy, describing the interaction between the applied field and the magnetisation of the FM. The second and third terms represent the anisotropy energies of the FM and AFM films. The final term represents the interaction between the two films where  $J$  is the interface exchange coupling constant. If we assume that the antiferromagnet is rigid the energy simplifies to:

$$E = -HM_{FM}t_{FM} \cos \theta + K_{FM}t_{FM} \sin^2 \theta - J \cos \theta \quad (1.8)$$

Minimising the energy w.r.t  $\theta$  gives two extrema for the direction of the magnetisation of the FM film when  $\theta = 0$  and  $\theta = \pi$ . Stability of the  $\theta = 0$  configuration is possible if  $J/t_{FM} + HM_{FM} + 2K_{FM} > 0$  and stability of the  $\theta = \pi$  configuration is possible if  $J/t_{FM} - HM_{FM} - 2K_{FM} > 0$ .

This corresponds to the coercive fields:

$$H_{c1} = -\frac{2K_{FM}t_{FM} + J}{M_{FM}t_{FM}} \quad (1.9)$$

$$H_{c2} = \frac{2K_{FM}t_{FM} - J}{M_{FM}t_{FM}} \quad (1.10)$$

As the two coercive fields are not equal in magnitude, the hysteresis cycle is shifted by the bias field given by:

$$H_{ex} = \frac{J}{M_{FM}t_{FM}} \quad (1.11)$$



The dependence of the exchange field on  $1/t_{\text{FM}}$  underlines the interfacial nature of the phenomenon and has been verified experimentally on several systems. However, the exchange fields estimated from equation (1.11) are orders of magnitude larger than those reported experimentally, if  $J$  is supposed to be similar to the bulk exchange constant [24]. Several other models summarized in [23] and [25] have been formulated to account for different important parameters in exchange biased systems, which are not taken into account in the basic Meiklejohn and Bean approach. The main limitation of this model is in considering that both the AFM and FM are perfectly uniform and single domain as it is unlikely that this effectively describes the lowest energy magnetic configuration near the interface. It is also assumed that the spin structure in the AFM layer remains fixed as the FM layer switches. An alternative model taking these limitations into account was proposed by Mauri in 1987 in allowing a domain wall to develop parallel to the interface in the AFM film during the FM reversal [26]. He assumed that the coupling at the interface between FM and AFM moments is ferromagnetic and the moments of the FM and AFM films are parallel at the surface in the absence of an applied field, the thickness of the FM film is smaller than the domain wall width and the FM is therefore considered single domain. The AFM is considered infinite and a domain wall is allowed to develop in the AFM during reversal of the FM. In order for the domain wall to form, its energy  $\sqrt{A_{\text{AFM}}K_{\text{AFM}}}$  must be less than the interfacial coupling energy  $J$ . Minimization of the system energy in this case gives an exchange field of:

$$H_{\text{ex}} = \frac{2\sqrt{A_{\text{AFM}}K_{\text{AFM}}}}{M_{\text{FM}}t_{\text{FM}}} \quad (1.12)$$

This means the exchange field is reduced by a factor  $J/2\sqrt{A_{\text{AFM}}K_{\text{AFM}}}$  and gives values for  $H_{\text{ex}}$  of the same order of magnitude as measured experimentally. There are still limitations to this model however. It is only valid for an ideally flat interface with a single domain

ferromagnetic film and an antiferromagnetic film of infinite thickness. It assumes the interface plane is homogenous and that the AFM moments at the interfaces are non-compensated. A compensated interface is one with an equal distribution of the two AFM sublattices at the interface. The ferromagnet is then exchange coupled equally to both sublattices and there is no net moment for the ferromagnetic to interact with. The previous models predict zero exchange field for this scenario but experimental studies show that this is not the case. A model by Koon [27] predicts the formation of domains in the AFM parallel to the interface in a similar manner to Mauri except that the interface can be compensated or non-compensated. The drawback is that the model assumes uniform properties at the interface. The Malozemoff model [28, 29, 30] has addressed this situation by considering that an ideal interface is unrealistic and that roughness leading to magnetic defects gives rise to local random fields. The total energy of the antiferromagnet, including the contribution from the random fields, is then minimized by the formation of domain walls perpendicular to the interface. The contribution of energy difference between the different random domains produces the exchange bias.

More recent experimental findings [31,32] support an extension of the Meiklejohn and Bean model by the discovery using x-ray magnetic circular dichroism (XMCD) that only a small fraction of AFM spins are pinned at the interface. These pinned spins do not rotate in an external magnetic field and the coupling between them and the spins in the FM layer results in the exchange bias and the shift of the hysteresis loop. The majority of the uncompensated interfacial spins, however, are not pinned. These spins are dragged along with the magnetisation reversal process in the FM layer and although they do contribute to an enhanced coercivity, they are not responsible for the exchange bias effect. Taking into account that only a small pinned fraction  $\rho$  of the uncompensated interfacial moments contributes to the bias, the Meiklejohn and Bean model (1.11) can be written as [31]:



$$H_{ex} = \frac{J_{eff}}{M_{FM}t_{FM}} \quad (1.13)$$

where  $J_{eff} = \rho J$

This eliminates the discrepancy between the values of J predicted by the Meiklejohn and Bean model and those measured experimentally.

All of these models and many more have found different degrees of agreement with the vast range of existing experimental results on exchange anisotropy. A fully comprehensive model of exchange bias is still lacking and there remain several unsolved issues. It seems the detailed mechanism of exchange bias may be quite different for each specific FM/AFM system. Nevertheless it is a phenomenon which has been implemented very successfully in several devices. The technological considerations in tailoring exchange bias for applications are well studied and will be discussed briefly in the next section.

#### 1.4.1 Exchange bias materials and properties

The choice and study of antiferromagnets for spin valves has been largely driven by the requirements of read head applications. The main requirements are as follows:

- Large exchange bias field
- High resistivity in order to reduce parasitic shunting of resistance in CIP geometry
- Low processing temperature so that the structural integrity of the rest of the stack is not affected during deposition or post deposition anneal
- Corrosion resistance
- Thermal stability - high blocking temperature  $T_B$ , the temperature below the antiferromagnetic ordering Néel temperature at which the exchange bias goes to zero.

- Low critical thickness - the minimum thickness of antiferromagnetic material for which exchange bias can be established.

The most commonly studied antiferromagnetic layers are manganese-based alloys such as FeMn, IrMn, NiMn, PdMn and PtMn. FeMn was for a long time the most intensively studied alloy. Films of composition  $\text{Fe}_{1-x}\text{Mn}_x$  with  $x \sim 0.5$  were implemented in some of the first spin valves [13]. Further studies indicated a low blocking temperature in the range 140 to 190 °C rendering the material unsuitable for disk-drive applications [33]. Other disadvantages include low stability with respect to Mn diffusion and poor corrosion resistance [34].  $\text{Ir}_{1-x}\text{Mn}_x$  with  $x \sim 0.8$  has been intensively studied since its introduction as an exchange bias material in 1996 [35] and is the material used in spin valves discussed in this work. One of its advantages is ease of processing. For spin valves in which the IrMn is grown on top of the FM layer (top spin valves), room temperature deposition in a small magnetic field is enough to establish reasonable exchange bias. For spin valves in which the IrMn is grown beneath the FM layer (bottom spin valves), a magnetic anneal is normally required although a small exchange bias at room temperature can be obtained. A detailed discussion of the effects of magnetic annealing on top and bottom IrMn spin valves is presented in Chapter 4. The advantages of IrMn over FeMn include higher blocking temperature, larger exchange field, lower critical thickness, higher resistivity and better stability against Mn diffusion [34, 38].

NiMn, PtMn and PdMn are ordered AFM compounds with very high Néel temperatures ranging from 540°C for PdMn to 800°C for NiMn. This makes them good candidates for application as exchange bias materials. Unfortunately in the as-deposited state these materials are random alloys with low exchange bias and a long annealing process is required to induce a phase transformation to the ordered state. In the case of NiMn, for



example, annealing processes from 10-40 hours at temperatures around 280 °C have been reported [36]. Nevertheless, these materials have very high blocking temperatures and excellent thermal stability [37,38], which makes them very suitable for use in spin valves for read head applications.

Oxide antiferromagnets, such as NiO and  $\alpha$ -Fe<sub>2</sub>O<sub>3</sub> have also been implemented in spin valves [39,40]. The obvious advantage of an oxide antiferromagnet is the elimination of current shunting through the layer due to its intrinsically high resistivity. An added advantage of increased GMR ratio due to specular reflection at the oxide interface was discovered when studying NiO spin valves. This has resulted in high GMR ratios of up to 28 % [41]. Unfortunately both NiO and  $\alpha$ -Fe<sub>2</sub>O<sub>3</sub> suffer from low exchange bias fields and large critical thicknesses. An overview of the main properties of the antiferromagnets used in spin valves from [42, 44] is given in Table 1.1.

AFM Films	FeMn	IrMn	NiMn	PtMn	NiO	$\alpha$ -Fe <sub>2</sub> O <sub>3</sub>
Critical thickness, $t_c$ (nm)	7–10	5–8	25	10–15	50	50
Neel Temp, $T_N$ (°C)	230	420	800	702	250	680
Blocking temp, $T_B$ (°C)	140-190	240-290	360-400	350-400	180-230	250
Exchange energy, $J$ (mJ/m <sup>2</sup> )	0.10-0.15	0.12-0.40	0.30-0.40	0.20-0.30	0.02-0.12	0.03-0.12

**Table 1.1 Characteristics of different types of antiferromagnets. Values of  $J$ (mJ/m<sup>2</sup>) are given for systems with CoFe as the ferromagnetic layer.**

## 1.5 Spin valve designs

Improvements in spin valve performance (GMR, exchange field, sensitivity) are continually pursued both through the development of new materials and the design of new spin valve geometries. The basic FM/NM/FM/AF spin valve has evolved into many variants [43, 44].

The standard spin valve is composed of at least six layers: buffer layer, free layer, spacer layer, pinned layer, antiferromagnetic layer and capping layer. The buffer layer is usually 2-5 nm of Ta and is used to increase the quality of the subsequent layers and reduce roughness. The relatively high resistivity ( $\rho = 160 \times 10^{-8} \Omega\text{m}$ ) of tantalum makes it a suitable choice as shunting effects through it are negligible. The capping layer is also usually Ta and protects the structure from oxidation and corrosion. The free layer in exchange biased spin valves generally consists of two ferromagnetically coupled layers with different compositions. The most frequently used combination is  $\text{Ni}_{80}\text{Fe}_{20}/\text{Co}_{90}\text{Fe}_{10}$ . The permalloy layer is used to reduce the coercivity whereas the CoFe gives a higher MR ratio due to the larger scattering potential for minority electrons at the CoFe/Cu interface. Usually the antiferromagnetic layer is at the top of the spin valve structure, hence the name top spin valve. The antiferromagnet can also be grown at the bottom of the stack – a bottom spin valve. The bottom spin valve is more difficult to realize experimentally as the structure generally needs to be annealed in a magnetic field to establish reasonable exchange bias. Typical MR values for top and bottom spin valves with IrMn range from 5 – 10%.

The dual (or symmetric) spin valve takes advantage of the fact that spin dependent scattering of the conduction electrons takes place at the magnetic/non-magnetic interfaces. Therefore it is possible to increase the MR ratio by increasing the number of interfaces.



Dual spin valves consist of essentially three FM layers separated by two non-magnetic spacers. The magnetisation of the outer two FM layers are pinned by an AFM layer, whereas the inner FM layer is free. An example of a dual spin valve structure is NiO/Co/Cu/Co/Cu/CoNiO. GMR ratios as large as 24.8% [45,46] have been reported for these spin valves but the increased thickness of the structure can make it unsuitable for read head applications.

A further advance in spin valve design was the development of the synthetic antiferromagnet (SAF). The SAF is a three-layer stack consisting of two ferromagnetic layers (usually Co or CoFe) separated by a thin layer of non-magnetic spacer (usually Ru). The coupling between the ferromagnetic layers oscillates between ferromagnetic and antiferromagnetic as a function of the Ru thickness and is strongly antiferromagnetic in the range 0.5-1.0 nm [47]. One of the ferromagnetic layers in the SAF is coupled to an antiferromagnet to give a spin valve of the form shown in Figure 1.11. The antiparallel coupling across the Ru layer is much stronger than the interfacial coupling between the FM/AFM layer and the two FM layers in the SAF remain antiparallel up to quite large fields. The magnetoresistance curve in Figure 1.11 shows that the pinning fields in the SAF spin valve can be twice as large as that of the standard spin valve and the GMR value is the same. Another advantage of using the SAF is that, in a patterned device, stray field created by the pinned layer on the sensing layer is reduced because of the antiparallel alignment of the two FM layers in the pinned layer. An analytical calculation of the magnetic response of the SAF spin valve has been carried out [48].

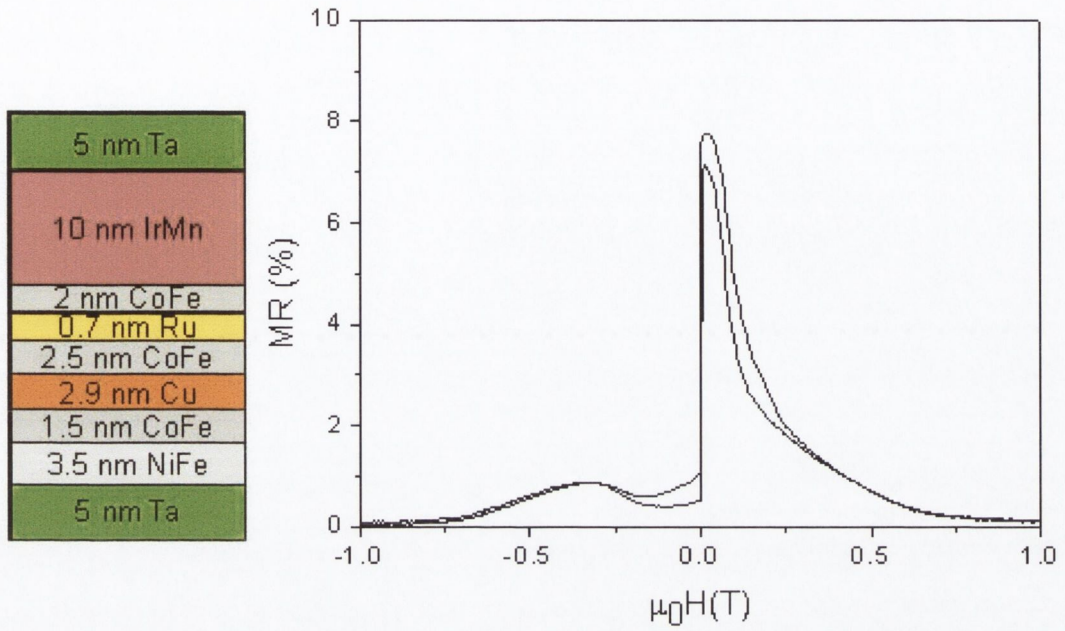


**Figure 1.11 Magnetotransport curve of SAF spin valve with stack composition shown.**

Spin valves with nano-oxide layers (NOL) were introduced in 1999 [49]. Very thin specularly reflecting oxide layers were introduced inside the pinned layer and near the free layer of the spin valve resulting in enhanced MR ratios of up to 18 %. This was attributed to specular reflection at the NOL interface. A specularly reflected electron at an interface in a CIP spin valve conserves its momentum parallel to the interface and its perpendicular component changes sign. The result is that the electrons move repeatedly through the active region in a manner that is equivalent to increasing the number of repeats in the structure. This affords an increase in the GMR of the structure without dramatically increasing the thickness. Nano-oxide layers are formed by the oxidation of an already deposited layer, or by the deposition of a magnetic oxide layer. NOLs inserted in the pinned layer should be thin enough such that a large effective exchange bias field is retained. Deposition is normally followed by an anneal step [50]. Specular reflection has



also been reported in spin valves with oxide antiferromagnets such as NiO [46] and  $\alpha$ -Fe<sub>2</sub>O<sub>3</sub> [51]. NOL insertion into a spin valve with a metallic antiferromagnet such as IrMn can be more useful due to the higher thermal stability and lower critical thickness of the antiferromagnet.

Spin filter spin valves have the structure AFM/FM/NM/FM/B where B is a conductive non-magnetic back layer. The result is an increased mean free path and reduced resistance for majority spin electrons in parallel alignment and hence an increased GMR ratio [52]. Optimisation is a trade off between the increased mean free path and increased current shunting through the back layer. The advantage of the spin filter spin valve is that the thickness of the free layer can be reduced to levels that would be sub-optimal without a back layer. A thinner free layer is advantageous for read head applications as the continued reduction in the bit size of magnetic recording heads means smaller magnetic flux coming from each bit. This means that the moment of the free layer must be decreased in order to maintain the same amplitude of rotation.

## 1.6 Spin valves devices

Spin valves are currently used in a wide variety of commercial sensor products. The main applications at present are in read heads of hard disk drives in the magnetic storage industry and as magnetic field sensors. The precise requirements of a spin valve sensor and its advantages over other types of sensor depend on the specific application. The general requirements for a spin valve sensor are as follows [53]:

- Large magnetoresistance ratio
- Large exchange bias field
- Large sensitivity

- Small hysteresis
- Low noise
- Thermal stability
- Good repeatability and reliability

Considerable advances in the areas of hysteresis and sensitivity were made by the discovery of the role of crossed anisotropy of the free and pinned layers [54]. The coercivity of the free layer of the spin valve is much smaller when the free layer has an in-plane uniaxial anisotropy with the easy axis perpendicular to the unidirectional easy axis of the pinned layer.

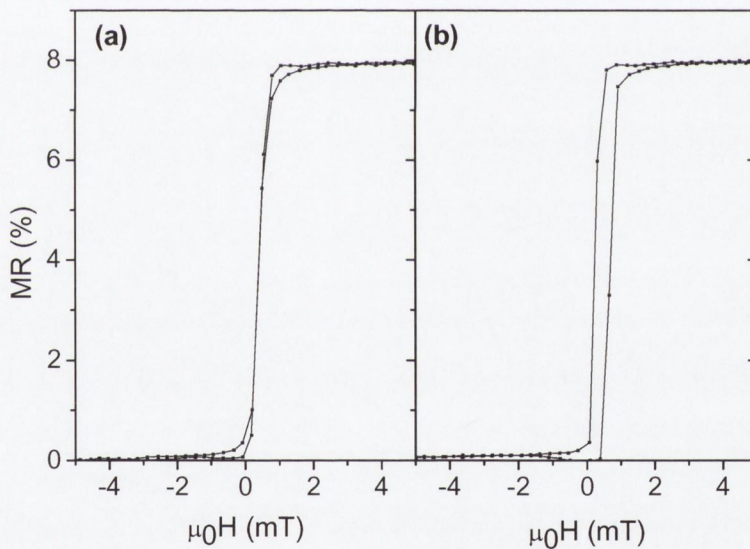


**Figure 1.12 Spin valve deposited with crossed anisotropy (a) and parallel anisotropy (b)**

In such systems with crossed-anisotropies when the external field is applied parallel to the biasing direction, the magnetisation of the free layer switches by coherent rotation



resulting in a near linear variation of the resistance with field. In contrast, in the case of parallel anisotropies, magnetisation reversal is the result of domain wall movement leading to hysteresis in the MR curve. As a result, strong Barkhausen noise is superimposed on the sensor output signal due to pinning and depinning of domain walls. In Figure 1.12, a spin valve with free layer NiFe(3.5nm)/CoFe(1.2nm) and pinned layer CoFe (2.5nm)/IrMn (10nm) is shown with crossed (a) and parallel (b) anisotropy. The crossed configuration was obtained by growth of the spin valve in a magnetic field and rotation of the sample by 90 degrees for growth of the pinned layer.

The crossed anisotropy configuration is used in applications where a linear, reversible, hysteresis-free output is required. These applications include read-heads for magnetic recording and magnetic field sensors. The hysteretic, irreversible switching of the parallel anisotropy configuration is useful when the spin valve is to be applied as a memory element in GMR MRAM for example where two zero field states of the free layer are required to represent a digital “0” and “1”.

### 1.6.1 Spin valves as magnetic-field sensors

Magnetic field sensors are in widespread commercial use in applications such as linear and rotary encoders, proximity detectors, speed and position sensors and Earth’s field magnetometers. Hall Effect devices are commonly used to sense magnetic fields in the range 10 - 1000 mT. Inductive coils or flux gates are also used but although inexpensive, they are relatively bulky and have poor low frequency response. AMR materials are used to sense below approximately 5 mT. Spin valves have surpassed many of these devices due to their higher output signal and sensitivity. Spin valves exhibit a change in resistance that is proportional to the cosine of the angle between the free and pinned layers. This can be exploited to create devices with an inherently linear relationship between the applied

magnetic field and the output voltage. Minimization of the noise and particularly the magnetic noise is essential for spin valve sensors. This can be achieved by appropriate design of the sensor geometry. The optimisation of spin valves for magnetic field sensors is described in detail in chapter 6.

### 1.6.2 Spin valves in read heads

An overwhelming amount of spin valve research has been driven by the interests of the magnetic storage industry. The first magnetic disk drive, introduced by IBM in the early 1950's, was termed RAMAC and had an areal density of 2 kb/in<sup>2</sup> [55]. The areal density of this drive, based on inductive technology, experienced a growth rate of 30 %/year until 1992 when magnetoresistive heads based on the anisotropic magnetoresistance of permalloy films were introduced. From this point on the areal density increased at a rate of 60 %/year boosted by the discovery of GMR and the implementation of spin valves in read heads in 1998. Today, areal densities of up to 100 Gb/in<sup>2</sup> have been demonstrated.

The principle of magnetic recording is illustrated schematically in Figure 1.13. The basic components are the recording media and a read-write head. The recording medium is a disk of magnetic material on which information is stored as abrupt changes in magnetisation, or magnetic bits in tracks along the disk. The areal density is then the product of the density at which transitions can be packed along a track (the linear bit density) and the density at which tracks can be packed together (the track density). The read-write head is positioned on an air bearing slider (ABS) at a fixed position above the disk. The writer is essentially a submicron electromagnet, the stray field from which is used to switch the magnetisation of bits on the recording media. The higher the saturation magnetisation of the pole pieces of the writer, the higher the write field. Materials currently used in write heads are Ni<sub>80</sub>Fe<sub>20</sub>, Ni<sub>45</sub>Fe<sub>55</sub> and FeTaN. The reader currently



consists of a spin valve stack electrically insulated from two thick shields of magnetic material such as NiFe. The free layer of the spin valve senses the stray field from adjacent bits in the magnetic media below it resulting in a voltage output. The purpose of the shields is to increase the resolution of the head along the track by absorbing all the magnetic flux coming out of the media except for just underneath the gap between the shields where the spin valve is located - the read gap.

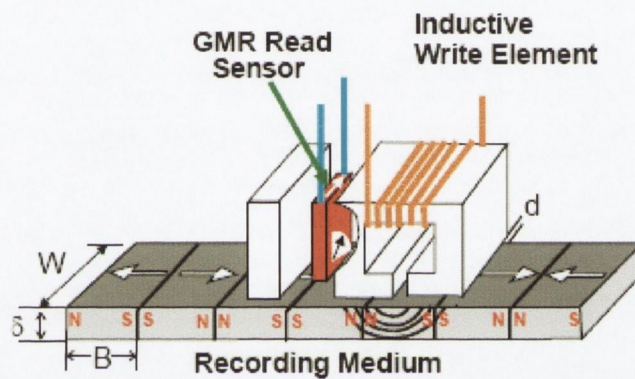


**Figure 1.13 Schematic cross section of a vertical read -head above a storage recording medium**

This is an example of a CIP vertical read head. The magnetisations of the free and pinned layers are set perpendicular to one another in order to have a linear response of the spin valve. Permanent magnets on either side bias the free layer in a direction perpendicular to the pinned layer and keep it in a domain-free state to reduce noise. The stray field from the recording medium is then in a direction perpendicular to the free layer and causes it to rotate coherently resulting in a linear response. This linear response can be compromised and offset from zero in a similar manner to blank spin valves as discussed in section 1.3.1. The interlayer coupling tries to align the free and pinned layers ferromagnetically. Other

forces include antiferromagnetic coupling with the dipolar field created by the pinned layer magnetisation which becomes important at smaller dimensions. The Oersted field created by the sense current in the spin valve also has an affect on the free layer. These fields can be adjusted in order to reduce the offset by optimisation of process and measurement parameters. The coupling between the layers can be reduced by appropriate choice of spacer layer thickness. The effect of the dipolar field of the pinned layer can be almost eliminated by use of a synthetic antiferromagnet as discussed in section 1.5 and the sense current can be changed to adjust the Oersted field. In practice a combination of these techniques is used.

An important parameter in the performance of read heads is the readout resolution parallel and perpendicular to the trackwidth of the recording medium. The resolution parallel to the trackwidth is determined by the effective length of the spin valve and is determined by the spacing between the leads, the position of the permanent magnets and is generally limited by the resolution of lithographic techniques. The resolution perpendicular to the trackwidth is determined by the read-gap which is determined by the combined thickness of the insulating layers and the spin valve stack. Reduction of the insulation thickness risks shortage and increased vulnerability to electrostatic discharge. Methods of reduction of the spin valve thickness through specular reflection and highly conductive layers have been investigated as discussed in section 1.5 but only small improvements can be foreseen. For this reason and several other advantages, more efforts are now focussed on CPP MR heads based on spin valves or tunnel junctions. In the CPP configuration the shields can double as current leads to the MR element and the need for the insulation layers is eliminated resulting in an immediate reduction of the read-gap and increased lateral resolution.



### 1.6.3 Spin valves in MRAM

Existing semiconductor random access memories such as SRAM (static random access memory) and DRAM (dynamic random access memory) are disadvantaged by their volatility [56]. Magnetic random access memory (MRAM) has the potential advantages of non-volatility, speed, unlimited write endurance and low cost. MRAM has been the subject of intense research over the last ten to fifteen years. Initial MRAM architecture was based on the AMR of NiFe elements but soon moved on to GMR multilayers and then spin valve structures. MRAM based on exchange bias spin valves have been demonstrated [57] but most work on GMR MRAM has been based on pseudo spin valve cells [56]. In the GMR-MRAM architecture, the spin valve elements are organised in a square array. Each spin valve element is located at a cross point between two sets of perpendicular lines, word lines and sense lines. Information is stored as the orientation of the magnetisation of the hard layer of the spin valve. In order to write information in a cell, pulses of current are simultaneously sent in the sense and word lines that cross at the selected cell. These currents generate two perpendicular magnetic fields on the hard layer (one along its easy axis and one along its hard axis) and can switch its magnetisation direction. The other spin valve cells experience either no field or one of the fields, i.e. are “half selected”. Only the cell which experiences both fields switches. The read process is performed by passing a current through the sense line to orient the magnetisation of the free layer and then reading the resistance. Since the cells are connected in series, a differential two-step read out process must be performed. This slows down the read time. Other limitations include low output signals and the unsuitability for scaling to high densities. The discovery of magnetic tunnel junctions (MTJs) offered the possibility of much higher signals and read times. Present research on MRAM focuses entirely on architectures based on magnetic tunnel junctions.

## 1.7 References

---

- [1] G.A. Prinz, *Science*, **282**, 1660 (1998).
- [2] J.F. Gregg, I. Petej, E. Jouguelet, C. Dennis, *J. Appl. Phys.* **35**, R121 (2002).
- [3] M.N. Baiblich, J.M. Broto, A.Fert, F. Nguyen Van Dau, F. Petroff, D. Etienne, G. Greuzet, A. Frederick, J. Cjazelas, *Phys. Rev. Lett.* **61**, 2472 (1988).
- [4] G. Binash, P. Grünberg, F. Saurenbach, W. Zinn, *Phys. Rev. B.* **39**, 4828 (1989).
- [5] S.S.P. Parkin, Chapter 5 in *Spin dependent transport in magnetic nanostructures*, ed. S Maekawa and T. Shinjo, Taylor and Francis (London) (2002)
- [6] R. Schad, C.D. Potter, G. Verbank, V.V. Moshchalkov, Y. Bruynseraede, *Appl. Phys. Lett.* **64**, 3500 (1994).
- [7] N.F.Mott, *Adv. Phys.* **13**, 325 (1964).
- [8] R. Coehoorn, Chapter 4 in *Magnetic Multilayers and Giant Magnetoresistance: fundamentals and applications*, Springer Series in Surface Sciences vol. **37**, U. Hartmann (ed) p. 65-127 (Berlin) (2000).
- [9] W.H. Butler, X.G. Zhang, D.M. Nicholson, J.M. MacLauren, *J. Magn. Magn. Mat.* **151**, 354 (1995).
- [10] T. Valet, A. Fert, *Phys. Rev. B.* **48**, (2003).
- [11] B.A. Gurney, V.S. Speriosu, J.P. Nozieres, H. Lefakis, D.R. Wilhoit, O.U. Need, *Phys. Rev. Lett.* **71**, 4023 (1993).
- [12] E. Tsymbal, D.G. Pettifor, “Perspectives of Giant Magnetoresistance”, *Solid State Physics*, **56**, 113 (2001).
- [13] B. Dieny, V.S. Speriosu, S.S.P. Parkin, B.A. Gurney, D.R. Wilhoit, D. Mauri, *Phys. Rev. B.* **43** 1297 (1991).
- [14] T. Shinjo, H. Yamamoto, *J. Phys. Soc. Jap.* **59**, 3061 (1990).



- 
- [15] L. Néel, *Comptes Rendues, Acad. Sci.* **255**, 1676 (1962).
- [16] J.C.S. Kools, Th. G.S.M. Rijks, A.E.M. De Veirman and R. Coehoorn, *IEEE Trans. Mag.* **31**, 3918 (1995).
- [17] T.C Schulthess and W.H. Butler, *J. Appl. Phys.* **87**, 5759 (2000).
- [18] C. Kittel, *Introduction to Solid State Physics*, 7<sup>th</sup> edition, Wiley, New York.
- [19] S.S.P. Parkin, R. Bhadra, and K.P. Roche, *Phys. Rev. Lett.* **66**, 2152 (1991).
- [20] J.L Leal, and M.H. Kryder, *IEEE Trans. Mag.* **32**, 4642 (1996).
- [21] W.H. Meiklejohn , C.P. Bean, *Phys. Rev.* **102**, 1413 (1956).
- [22] W.H. Meiklejohn , C.P. Bean, *Phys. Rev.* **105**, 904 (1957).
- [23] J. Nogués and I.K. Schuller, *J. Mag. Magn. Mater.* **192**, 230 (1999).
- [24] R.Jungblut, R.Coehoorn, M.T. Johnson, J. aan de Stegge, A. Reinders, *J. Appl. Phys.* **75**, 6659 (1994).
- [25] R. L. Stamps, *J. Phys. D: Appl. Phys.* **33**, R247 (2000).
- [26] D. Mauri, H.C. Siegmann, P.S Bagus, E.Kay, *J. Appl. Phys.* **62**, 3047 (1987).
- [27] N.C. Koon, *Phys. Rev. Lett.* **78**, 4865 (1997).
- [28] A. P. Mazolemoff, *Phys. Rev. B* **35**, 3679 (1987).
- [29] A.P. Mazolemoff, *Phys. Rev. B* **37**, 7673 (1988).
- [30] A.P. Mazolemoff, *J. Appl. Phys.* **63**, 3874 (1988).
- [31] H. Oldag, A. Scholl, F. Nolting, E. Arenholz, S. Maat, A.T. Young, M. Carey, J. Stöhr, *Phys. Rev. Lett.* **91**, 017203 (2003).
- [32] T.P.A. Hase, B.D. Fulthorpe, S.B. Wilkins, B.K. Tanner, C.H. Marrows, B.J. Hickey, *Appl. Phys. Lett.* **79**, 985 (2001).
- [33] A. Devasahayam, M.H. Kryder, *IEEE Trans. Magn.* **35**, 649 (1999).
- [34] G.W. Anderson, M. Pakala, Y. Huai, *IEEE Trans. Magn.* **36**, 2605 (2000).
- [35] K. Hoshino, R. Nakatani, R. Hoshiya, Y. Sugita, *Jpn. J. Appl. Phys.* **33** 1327 (1996).

- 
- [36] T.Lin, D.Mauri, N.Staud, C.Hwang, J.K. Howard, G.L. Gorman, *Appl. Phys. Lett.* **65**, 1183 (1994).
- [37] T. Lin, C. Tsang, R.E. Fontana, J.K. Howard, *IEEE Trans. Magn.* **31**, 2585 (1995).
- [38] G.W. Anderson, Y. Huai, M. Pakala, *J. Appl. Phys.* **87**, 5726 (2000).
- [39] C. Cowache, B. Dieny, A. Auffret, M. Cartier, R.H. Taylor, R. O'Barr, S.Y. Yamamoto, *IEEE Trans. Magn.* **34**, 843 (1998).
- [40] Y. Kawawake, Y. Sugiat, M. Satomi, H. Sakakima, *J. Appl. Phys.* **87**, 6983 (2000).
- [41] H. Sakakima, Y. Sugiat, M. Satomi, Y. Kawawake, *J. Mag. Magn. Mater.* **198**, 9 (1999).
- [42] E. Hirota, H. Sakakima, K. Inomata, *Giant Magneto-Resistance Devices*, Springer Series in Surface Sciences, **40**, 177 (2000).
- [43] B. Dieny, Chapter 1: Spin valves "Magnetoelectronics", Ed. Mark Johnson, Elsevier (2004).
- [44] R. Coehoorn, *Handbook of Magnetic Materials*, **15**, 1-197 (2003), Elsevier.
- [45] W.F. Egelhoff, T. Ha, R.D.K. Misra, Y. Kadmon, J. Nir, C.J. Powell, M.D. Stiles, R. McMichael, C.L. Lin, J.M Siversten, J.H. Judy, K. Takano, A.E. Berkowitz, T.C. Anthony, J.A. Brug, *J.Appl. Phys.* **78**, 273 (1995).
- [46] W.F. Egelhoff, P.J. Chen, C.J. Powell, M.D. Stiles, R. McMichael, C.L. Lin, J.M Siversten, J.H. Judy, K. Takano, A.E. Berkowitz, T.C. Anthony, J.A. Brug, *J.Appl. Phys.* **79**, 5277 (1996).
- [47] S.S.P Parkin, N. More, K.P. Roche, *Phys. Rev. Lett*, **64**, 2304 (1990).
- [48] B. Dieny, M. Li, S.H. Liao, C. Horng, K. Lu, *J. Appl. Phys.* **87**, 3415 (2000).
- [49] Y. Kamiguchi, K. Saito, K. Kouji, M. Yoshiwaka, H. Yuase, H. Fukuzawa, S. Hashimoto, H. Iwasaki, H. Yoda, M. Sahashi, US patent 6,303,218 B1, (1999).



- 
- [50] H. Fukuzawa, K. Koi, H. Tomitas, H.N. Fuke, Y. Kamiguchi, H. Iwasaki, M. Sahashi, *J. Magn. Magn. Mater.* **235**, 208 (2001).
- [51] Y. Sugita, Y. Kawawake, M. Satomi, H. Sakakima, *Jpn. J. Appl. Phys.* **37**, 5984 (1998).
- [52] B.A. Gurney, V.S. Speriosu, V.S. Nozieres, J.P. Lefakis, D.R. Wilhoit, O.U. Need, *Phys. Rev. Lett.* **71**, 4023 (1993).
- [53] S. Tumanski, "Thin Film Magnetoresistive Sensors", IOP Series in Sensors (2001).
- [54] TH.G.S.M. Rijks, W.J.M. de Jonge, W. Folkerts, J.C.S. Kools, R. Coehoorn, *Appl. Phys. Lett.* **65**, 916 (1994).
- [55] C. H. Tsang, R. E. Fontana, Jr., T. Lin, D. E. Heim, B. A. Gurney, and M. L. Williams, *IBM Journal of Research and Development*, **42**(1) (1998)
- [56] S. Tehrani, E. Chen, M. Durlam, M. DeHarra, J.M. Slaughter, J. Shi, G. Kerszykowsly, *J. Appl. Phys.* **85**, 5822 (1999).
- [57] D.D. Tang, P.K. Wang, V.S Speriosu, S. Le, K.K. Kung, *IEEE Trans. Magn* **31**, 3203 (1995).

## Chapter 2

# Experimental Techniques

### 2.1 Magnetron sputtering in the Shamrock Deposition Tool

In this section the basics of magnetron sputtering are described followed by a description of the Shamrock Deposition tool, which was used to deposit all of the samples discussed in this thesis.

#### 2.1.1 Magnetron Sputtering

Sputtering is a physical process whereby atoms in a solid target are ejected into the gas phase due to bombardment of the surface of the target material by energetic ions. The ions for the process are supplied by a plasma which is created by applying a voltage across a gas, usually Argon, at low pressure ( $10^{-3}$  mbar). Ar ions then strike the target with sufficient energy to cause the ejection of surface atoms which are deposited on the substrate, and secondary electrons, which cause further ionization of the gas. Magnetron sputtering is a technique where a magnetic field is incorporated into the target gun in order to trap electrons and increase the plasma ionization [1]. Figure 2.1 shows a cross section of the Series III magnetron guns used in the Shamrock. An array of permanent magnets



surrounding the cathode target creates a magnetic field parallel to the cylindrical cathode surface. Combined with an electric field, this causes a drift of the secondary electrons in closed orbits in front of the target surface. This restricts the electron motion to the vicinity of the cathode, thereby increasing the ionization efficiency. At the same time, a substantial fraction of the ions produced in the trap volume are attracted to the target (cathode), leading to sputter erosion of it.

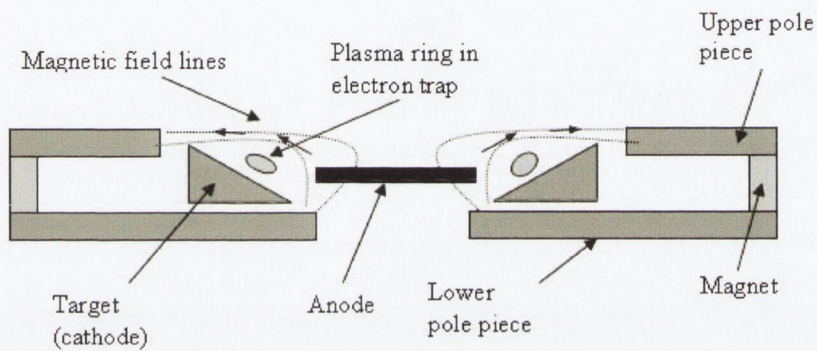


**Figure 2.1** Cross section schematic of the S-Gun magnetron

### 2.1.2 The Shamrock

The Shamrock is a fully automated commercial magnetron sputter system, which is housed in a class 1000 cleanroom (Figure 2.2). The system consists of four high vacuum chambers; two process chambers A and B, a transfer module and a cassette module or load-lock (Figure 2.3). The central transfer module is separated from the other chambers via VAT gate valves. Chamber A is the original process chamber and is used for room-temperature deposition. Chamber B was custom designed for high temperature deposition of oxides and was added to the original system.

Chamber A is a sputter-up deposition system. The base of the chamber contains six water-cooled Series III magnetron S-guns. All six magnetrons work in DC mode. Six 2.5 kW Advanced Energy power supplies control the cathode bias and two HP power supplies control the anode bias on guns 1-3, 4-6 respectively. It is not essential to apply anode bias but it can be used to increase the deposition rate. Guns 5 and 6 can also work in RF mode (2x Dresslar CESAR 300W RF supply & matching network) by connecting the RF directly to the gun or by connecting to an RF plasma ring directly above the guns. A pulsed DC power supply can be connected to gun 2 and there is also an ion mill for substrate cleaning.

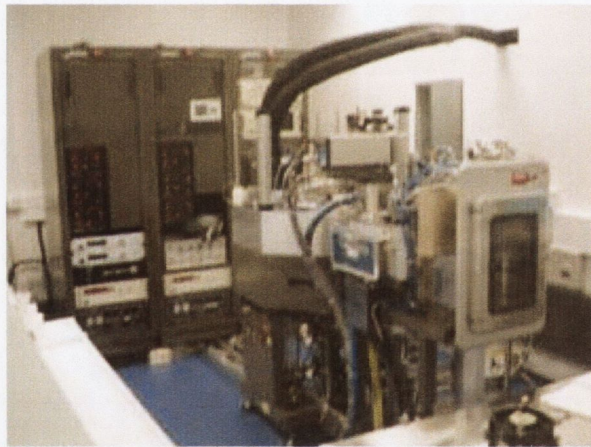


**Figure 2.2 The shamrock sputtering tool in the CINSE class 1000 cleanroom**

3 inch cup shaped targets are used in the system. Target change is a simple process and the system can be turned around in approximately fifteen minutes. One disadvantage of the magnetron configuration evidenced by the Shamrock is inefficient target usage. Targets burn through around a central ring and then need to be replaced.



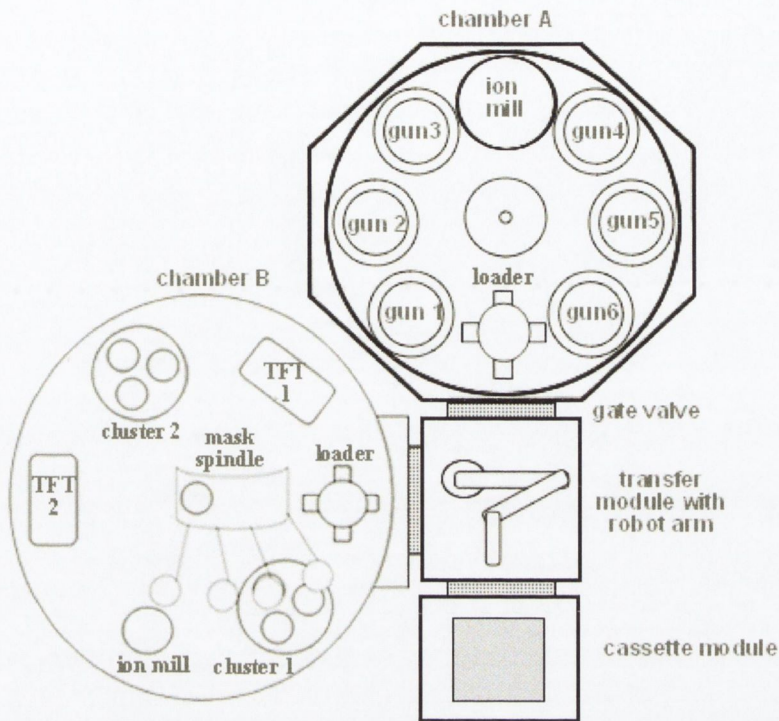


**Figure 2.3 Schematic of the shamrock**

Chamber A is currently configured for 4-inch wafers but can handle up to 6 inch. 4 inch wafers are fitted into 4.5 inch square metal adapters and placed in a cassette that holds up to 16 wafers in the cassette module. Metal shadow masks can be placed in contact with the wafers in the adapter. A robot arm housed in the transfer module picks the wafers and transfers them to chamber A where they are placed, facing down, in one of four substrate positions, or planets, on the turntable. During process the turntable rotates around its central axis while at the same time each planet rotates about its own axis resulting in the so-called planetary motion of the substrates (Figure 2.4 left). This allows uniform deposition on 4-inch or 6-inch wafers from only 3-inch targets. Each substrate planet contains an integrated array of permanent magnets with in-plane field strength of 5 mT for growth-induced easy-axis (Figure 2.4 right). The chamber is equipped with a loader,

which loads wafers from the robot arm to the planet and an aligner, which aligns planets correctly to receive the wafers. The loader and aligner can be used for in-situ 90-degree reorientation of the samples in order to deposit magnetic multilayers with different magnetisation directions.

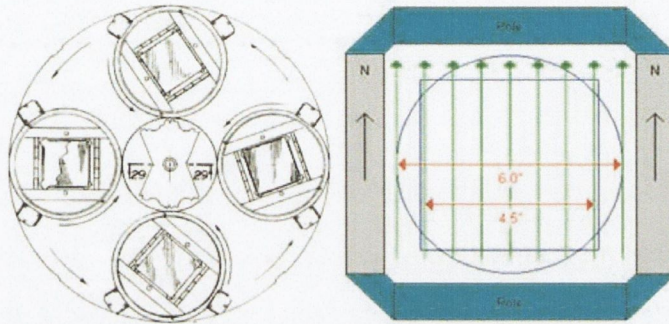


**Figure 2.4 Schematic of turntable showing planetary motion (left) and substrate planet with integrated magnetic array (right)**

Typical base pressure in chamber A is  $1 \times 10^{-7}$  mbar. Process pressure (through introduction of high purity Ar) is  $3 \times 10^{-3}$  mbar. The chamber is reactive sputtering capable. Oxygen can be introduced through a special reactive gas ring above gun 5. This is typically used for the deposition of tunnel barriers.

Film thickness is controlled by deposition time, and deposition rate is calibrated by measuring the thickness of calibration samples using X-Ray reflectometry (section 2.6). Typical deposition parameters are shown in Table 2.1.



Target	Deposition pressure (mbar)	Ar flow (sccm)	Gun number	Power (watts)	Deposition rate (Å/s)
Ta	$3 \times 10^{-3}$	25	4	150	0.18
Ni <sub>81</sub> Fe <sub>19</sub>	$3 \times 10^{-3}$	25	6	150	0.24
Co <sub>90</sub> Fe <sub>10</sub>	$3 \times 10^{-3}$	25	3	150	0.19
Cu	$3 \times 10^{-3}$	25	2	100	0.30
Ir <sub>20</sub> Mn <sub>80</sub>	$3 \times 10^{-3}$	25	1	150	0.28
Ru	$3 \times 10^{-3}$	25	5	100	0.07

**Table 2.1 Typical deposition parameters for the Shamrock**

There are no shutters in chamber A. A burn-in with four dummy wafers is done immediately before deposition and then usually one of the four dummies is replaced with a clean substrate for process. Up to four wafers can be processed at a time. The Shamrock tool was previously owned by Agere Systems Ltd. It was rebuilt and installed in TCD in 2002.

Chamber B was added to the Shamrock in 2005. It was designed specifically for the high temperature deposition of oxide materials. It is also a sputter-up chamber. It has two DC cluster guns which each contain three 3-inch targets with shutters, two target-facing-target (TFT) guns for RF sputtering of insulating materials and a Copra ion source for substrate cleaning and implantation. The chamber is capable of reactive sputtering and substrates can be heated up to 800 °C during deposition. The base pressure of the chamber is  $10^{-8}$  mbar. Wafers are loaded via the robot arm in the same way as chamber A. Separate computers control the processes in the two chambers. The spin valves discussed in this thesis were deposited in chamber A.

## 2.2 Magnetoresistance measurements

For blank samples, resistance is measured using the standard four-point probe, in-line geometry (Figure 2.5). Contacts are pressure contacts with a fixed position on the sample surface. Contacts to samples deposited through shadow masks were made with silver paint. Resistance is measured in 4-point configuration using a computer-controlled set-up with a Keithley 2400 source meter. The field is generated by an electromagnet driven by a Kepco 10 amp bi-polar power supply. The maximum field attainable using this power supply is 170 mT. The field is applied parallel to the current direction and is measured by reading out the voltage from a Hall sensor attached to one of the pole pieces of the magnet. Samples requiring higher fields were measured in the superconducting magnet described in section 2.5.

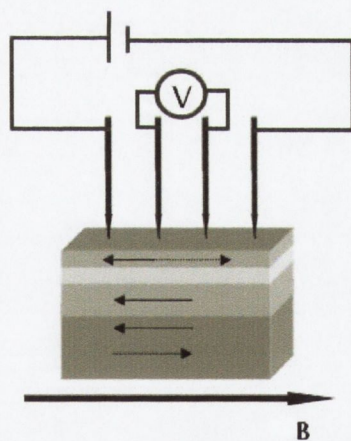


**Figure 2.5** Four point magnetoresistance measurement

## 2.3 Noise Measurements

Noise measurements on patterned spin valve sensors and on the mixed sensor discussed in Chapter 6 were carried out at the CEA, Saclay by M. Pannetier and C. Fermon. The measurements were obtained in a simple four point DC configuration using a low noise



battery to supply current to the sample and then reading the voltage fluctuations through a preamplifier as a function of time. The specific details of the noise measurements for the mixed sensor can be found in [2].

## 2.4 Superconducting Quantum Interference Device (SQUID)

A Quantum Design Magnetic Property Measurement System (MPMS) sample magnetometer was used to characterise the magnetic properties of thin films. A superconducting quantum interference device (SQUID) detection system is integrated with a temperature control unit, a high field superconducting magnet and the computer operating system. Liquid helium is necessary for refrigeration of the superconducting components as well as for low temperature measurements. The exceptional sensitivity of the magnetometer makes it ideal for thin film measurements where the signals are too weak for detection in a VSM. Measurements can be made between 1.7 and 800 K in a field of up to 5 T, with a sensitivity of  $10^{-11}$  Am<sup>2</sup>

## 2.5 Magnetic annealing

Magnetic annealing is a post-deposition technique used to establish or improve exchange bias of spin valves and FM/AFM bilayers. Spin valves are often annealed in relatively small magnetic fields of several hundred millitesla. For this work, an annealing furnace was specifically designed and constructed to fit into a superconducting magnet in order to anneal spin valves at fields up to 5.5 T. A schematic of a cross-section of the furnace inside the superconducting magnet is shown in Figure 2.6. The superconducting magnet is a cryogen free Cryogenic Ltd. Magnet with a 100 mm room temperature bore. The magnet is cooled to an operating temperature of 7.5 K using a closed circuit Leybold helium compressor. The magnet can be ramped remotely via a PC at various ramp rates up to a maximum field of 5.5 T. The field is parallel to the bore axis and the maximum field inside the bore is positioned 280 mm from the top of the magnet casing. The furnace was

designed in collaboration with Magnetic Solutions Ltd. The furnace is essentially a quartz tube with a resistive heater wrapped around the outside. The tube is pumped by a Pfeiffer turbomolecular pumping station to a pressure of  $10^{-6}$  mbar. A sample rod was designed to fit into the quartz tube such that samples are placed at the central field point of the magnet. Samples are inserted with their easy axis aligned with the field, parallel to the bore axis. Temperature is monitored and controlled using a Eurotherm 2416 temperature controller and a thermocouple fixed on the sample rod. Power to the heater from a 1 kW power supply is controlled by the temperature controller. The quartz tube is fixed inside a large metallic cylindrical water jacket designed to fit into the 100 mm bore of the magnet. Water is circulated continuously during process to avoid heating and quenching of the magnet. The set-up was built from non-magnetic material and screwed rigidly to the magnet. This was done to avoid potentially damaging movement of the furnace within the magnet at high field.

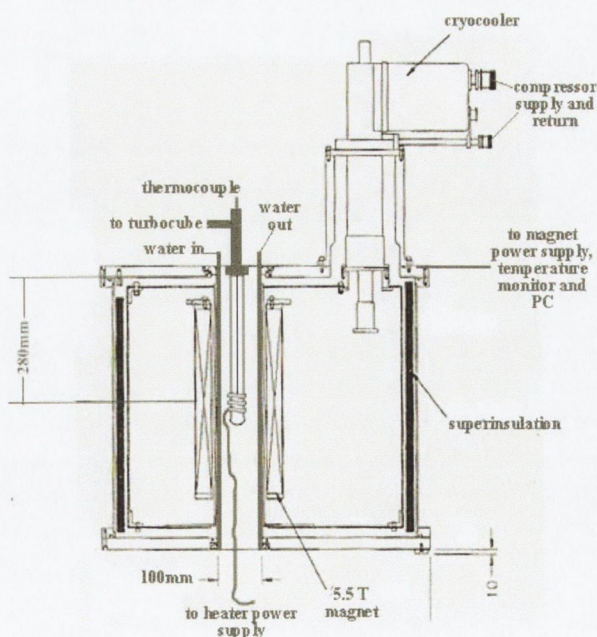


**Figure 2.6** Cross-section schematic of magnetic furnace inside superconducting 5.5 T Cryogenics magnet



## 2.6 X-ray Diffraction

X-ray diffraction (XRD) is a widely used technique for materials characterisation due to the variety of structural information, which can be obtained from it in a non-destructive manner. The wavelength of X-ray radiation is of the order of interatomic distances in typical crystal lattices. Thus a variety of X-ray scattering techniques exist for the characterisation of lattices by interference phenomena.

At large incident angles, X-rays are diffracted from different lattice planes in a crystalline film and constructively interfere to give peaks in the reflected intensity when Bragg's law is satisfied:

$$m\lambda = 2d \sin \theta \quad (2.1)$$

where  $m$  is an integer designating the order of reflection,  $\lambda$  the wavelength of x-ray radiation,  $\theta$  the angle of incidence and  $d$  the distance between lattice planes. X-ray diffraction of thin films yields information on lattice constants, textures and strains.

At low incident angles ( $1^\circ < \theta < 10^\circ$ ) the X-rays are sensitive to larger distances such as film thicknesses in the nanometer range and the technique is called X-ray Reflectometry (XRR). In this configuration total external reflection will occur below a critical angle,  $\theta_c$ . The critical angle depends on the electronic density and refractive index of the material. Above  $\theta_c$ , an interference pattern is formed between reflections from the film surface and from the film/substrate interface. This results in a series of maxima in the reflected intensity. The maxima positions can be determined in analogy to the Bragg positions in lattice diffraction. The Bragg equation at low angles can be approximated as:

$$\sin^2 \theta_m = \left( \frac{m\lambda}{2D} \right)^2 \quad (2.2)$$

where  $\theta_m$  is the position of the  $m^{\text{th}}$  fringe,  $D$  is the film thickness,  $\lambda$  is the wavelength of X-ray radiation. Hence a plot of  $\sin^2\theta_m$  versus the order  $m$  of the peaks should give a straight line, the slope of which gives the film thickness [3].

X-Ray diffraction and reflectivity measurements were performed in a Phillips X-Pert Pro system using  $\text{Cu-K}\alpha$  radiation of wavelength  $\lambda = 1.5406\text{\AA}$ . The schematic of the system showing its major components is shown in Figure 2.7. The film was aligned in the beam by adjusting the height and position of the sample stage. Fits to the measured data were generated using either the Phillips software WINGIXA or the freely available software called IMD [4]. An example of a measured curve with fit is given in Figure 2.8.

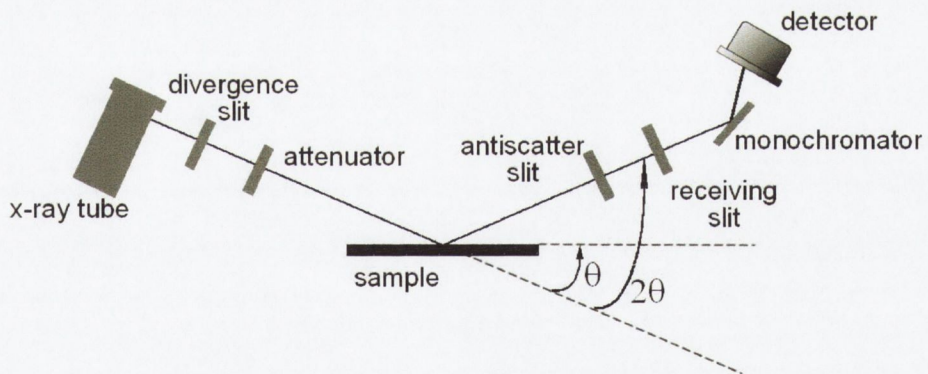


**Figure 2.7 Schematic of XRR set-up**



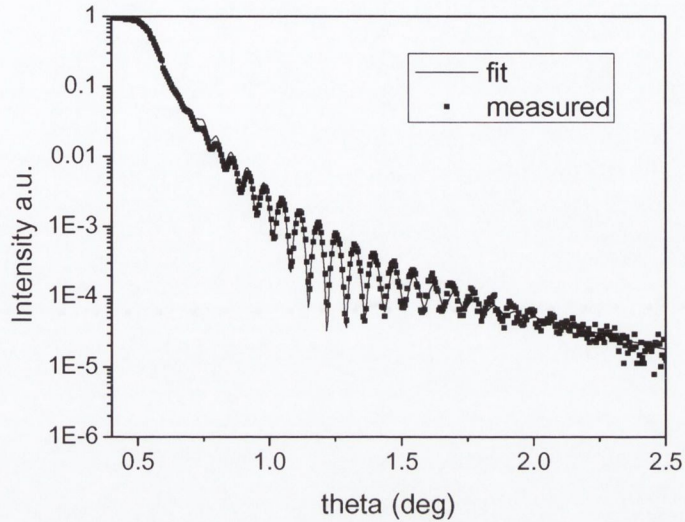


**Figure 2.8** Reflectivity curve with fit for a Au film of thickness 53nm

## 2.7 Polarised Neutron Reflectometry

Polarised neutron reflectometry is a technique which can be applied to magnetic multilayers in order to obtain structural information such as individual layer thicknesses and magnetic information such as layer resolved magnetisation vectors. Spin valves were characterised using PNR at the Laboratoire Léon Brillouin (LLB) [5] at Saclay, France, and the results are presented in Chapter 3. As the technique is not very well known, the basic principles of PNR are described in the following section (and in detail in [6]) and section 2.7.6 describes the PRISM reflectometer at LLB.

### 2.7.1 Principles of neutron reflectivity

The neutron is a neutral particle and can be described by a plane wave of wavelength  $\lambda$ , and a wave vector  $k_0$  according to:

$$k_0 = \frac{2\pi}{\lambda} \quad (2.3)$$

and of energy  $E_0$ :

$$E_0 = \frac{\hbar^2 k^2}{2m} \quad (2.4)$$

Its wavefunction satisfies the Schrödinger equation:

$$\frac{\hbar^2}{2m} \frac{d^2 \psi}{dr^2} + [E - V(r)] \cdot \psi = 0 \quad (2.5)$$

where  $m$  is the neutron mass,  $E$  its energy and  $V$  the interaction potential. The neutron is a spin  $1/2$  particle and can be in two spin states  $+1/2$  or  $-1/2$ . When there is an external or internal magnetic field, an “up” neutron describes a  $+1/2$  neutron aligned parallel to the field and a “down” neutron is  $-1/2$  neutron antiparallel to the field.

### 2.7.2 Neutron-matter interaction

The two main interactions of the neutron are the strong interaction with the nuclei and the magnetic interaction with the magnetic moments. The neutron-nucleus interaction can be modelled by a potential of the form:

$$V_F = b \left( \frac{2\pi\hbar^2}{m} \right) \delta(r) \quad (2.6)$$

where  $b$  is the neutron scattering length and depends on the nucleus and the nuclear spin of the nucleus. The magnetic interaction is the dipolar interaction of the neutron spin with the magnetic field created by the unpaired electrons of the magnetic atoms and is given by:

$$V_M(r) = -\mu \cdot B(r) = g_n \mu_n \sigma \cdot B(r) \quad (2.7)$$

where  $g_n$  is the gyromagnetic ratio of the neutron,  $\mu_n$  is the neutron magnetic moment and  $\sigma$  is the Pauli operator associated with the neutron spin.



### 2.7.3 Reflectivity on Non-Magnetic Systems

Neutron reflectivity on non-magnetic systems can be described using optical indices in a similar approach to the X-ray formalism. Consider a neutron beam, reflected by a perfect surface with an incident angle  $\theta_i$  as shown in Figure 2.9. The surface is defined by the interface between air ( $n=1$ ) and a material with optical index  $n$ . The scattering wave vector,  $\mathbf{q}$ , is given by  $\mathbf{q} = \mathbf{k}_r - \mathbf{k}_i$  and the projection of the scattering vector on the  $z$  axis is given by:

$$q_z = \frac{4\pi}{\lambda} \sin \theta_i \quad (2.8)$$

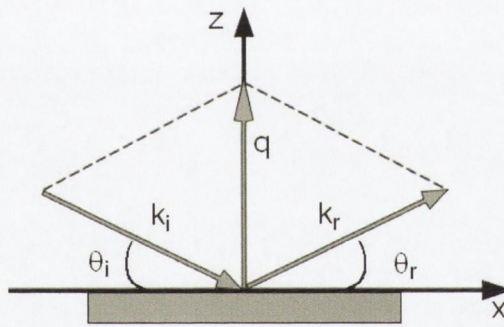


**Figure 2.9** Schematic of axis notation used for reflection from a surface

Since the potential  $V$  is only  $z$  dependent, the Schrödinger equation reduces to the 1 dimensional equation:

$$\frac{\hbar^2}{2m} \frac{d^2\psi}{dz^2} + [E_z - V_z]\psi_z = 0 \quad (2.9)$$

which can be written in the form of a Helmholtz propagation equation as:

$$\frac{d^2\psi}{dr^2} + k^2\psi = 0 \quad (2.10)$$

with

$$k^2 = \frac{2m}{\hbar^2} [E - V] \quad (2.11)$$

and

$$V = \frac{2\pi\hbar^2}{m} b\rho \quad (2.12)$$

where  $\rho$  is the number of atoms per unit volume. In the non-magnetic medium the general solution is given by:

$$\psi_z = Ae^{ik_r z} + Be^{-ik_r z} \quad (2.13)$$

The transmitted wave vector can be related to the incident vector using equation (2.11):

$$k^2 = \frac{2m}{\hbar^2} [E - V] = k_{in}^2 - 4\pi\rho b \quad (2.14)$$

The classical Fresnel formulae can be used to describe the reflected and transmitted amplitudes:

$$r = \frac{\sin \theta_i - n \sin \theta_r}{\sin \theta_i + n \sin \theta_r}$$

$$t = \frac{2 \sin \theta_i}{\sin \theta_i + n \sin \theta_r} \quad (2.15)$$

From the optical index,  $n^2 = k_r^2 / k_0^2$  it is possible to define a critical angle for total reflection,  $\theta_c$  as:

$$\theta_c = \sqrt{\frac{\rho b}{\pi}} \lambda \quad (2.16)$$

In terms of the scattering wave vector, the reflected intensity is given by:

$$R = \left| \frac{k_i - k_r}{k_i + k_r} \right|^2 \quad (2.17)$$



Figure 2.10 shows a reflectivity curve for a perfect silicon surface.

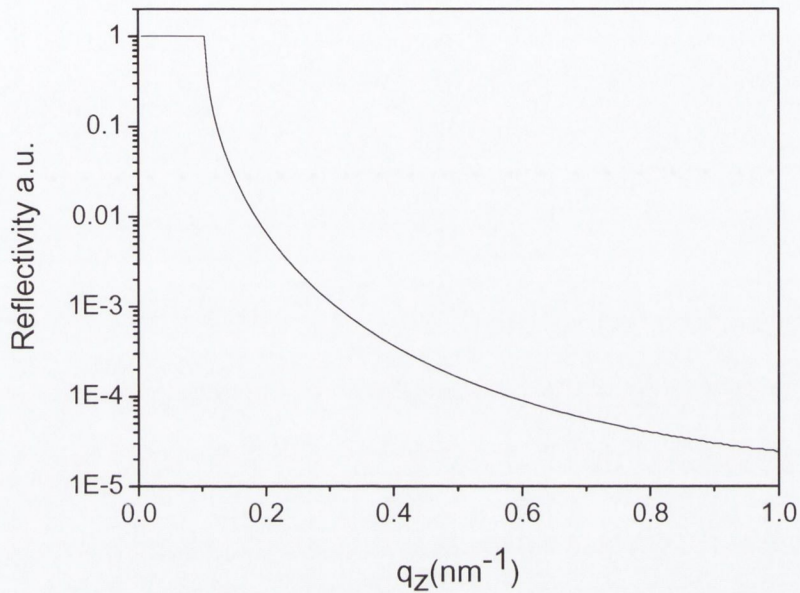


**Figure 2.10 Neutron reflectivity from a perfect silicon surface [6].**

#### 2.7.4 Neutron reflectivity on magnetic systems

If the system is magnetic, or if there is an external magnetic field on the sample, we need to take into account the spin of the neutron. If the magnetisation of the system is aligned with the applied magnetic field and the quantization axis of the neutrons then it is possible to describe the situation using optical indices in a similar manner to the description above except that now the optical index depends on the magnetisation. This is presented in section 2.7.5 below. In the case where the magnetisation is not aligned with the quantisation axis of the neutrons, it is not possible to use optical indices and the Schrödinger equation must be completely solved. This will not be described here.

### 2.7.5 Interaction of the neutron with a magnetic layer

The neutron magnetic interaction with a magnetic thin film is given by:

$$V = -g_n \mu_n \sigma \cdot [\mu_0 M_{//} + B_0] \quad (2.18)$$

Where  $M_{//}$  is the in-plane component of the magnetisation of the film and  $B_0$  is the external field. This highlights the main limitation of PNR for the study of magnetic films; it is only sensitive to the in-plane magnetisation.

Consider a magnetic thin film of thickness  $d$ . If the magnetisation of the film is parallel to the applied field and the neutron quantization axis then all the magnetisation components are parallel and no spin flip scattering can occur. The interaction of a neutron with a magnetic film depends on whether the neutron spin is aligned parallel or antiparallel to the film magnetisation. We define the magnetic interaction potential  $V^+$  when the neutron spin is parallel to the magnetisation and  $V^-$  when it is antiparallel:

$$\begin{aligned} V^+ &= -g_n \mu_n \sigma \cdot [\mu_0 M + B_0] \\ V^- &= +g_n \mu_n \sigma \cdot [\mu_0 M + B_0] \end{aligned} \quad (2.19)$$

It is possible to define a magnetic scattering length  $b_M$ :

$$b_M = \frac{m}{2\pi\hbar^2} \frac{g_n \mu_n [\mu_0 M_{//} + B_0]}{\rho} \quad (2.20)$$

The total interaction potentials are then given by:

$$V^{+/-} = \frac{2\pi\hbar^2}{m} \rho (b_n + /- b_m) \quad (2.21)$$

The two potentials  $V^+$  and  $V^-$  correspond to the interaction potentials seen by neutrons polarised respectively parallel and antiparallel to the applied field.



The optical index for neutrons parallel to the magnetisation is given by:

$$n^+ \approx 1 - \frac{\lambda^2}{2\pi} \rho(b_n + b_m) \quad (2.22)$$

and for neutrons antiparallel to the magnetisation by:

$$n^- \approx 1 - \frac{\lambda^2}{2\pi} \rho(b_n - b_m) \quad (2.23)$$

For the case of magnetic systems it is therefore possible to measure two reflectivity curves, one for neutron spins aligned parallel to the applied field (an “up” curve,  $R^{++}$ ) and one for neutron spins aligned antiparallel to the applied field (a “down” curve,  $R^-$ ). Figure 2.11 illustrates the reflectivity of a magnetic thin film. The optical index is higher for “up” neutrons compared to “down” neutrons and two distinct critical angles can be measured. The thickness of the film is determined by the spacing of the interference fringes in the same way as X-ray reflectivity.

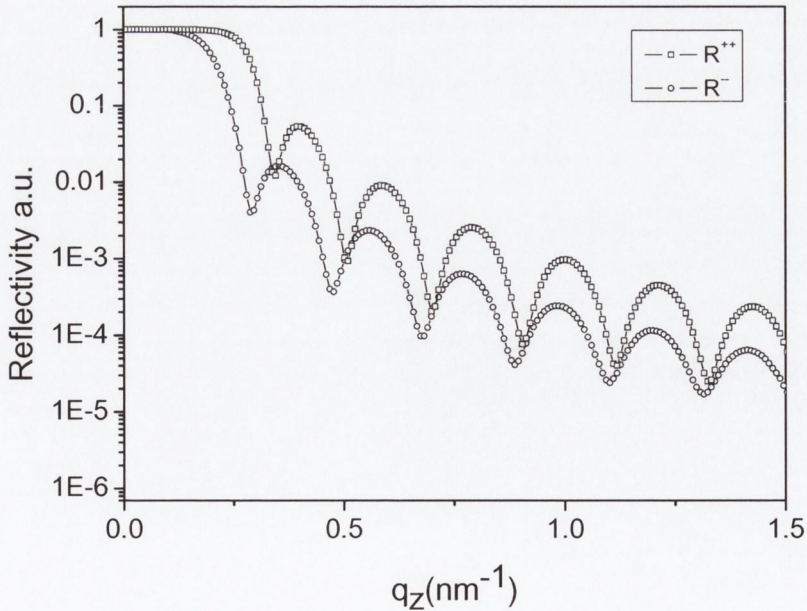


Figure 2.11 Up and down reflectivities on a nickel thin film [6].

If the magnetisation of the film is not aligned with the neutron quantisation axis a spin flip signal appears. In this case an “up” neutron will be transformed to a “down” neutron upon reflection. This situation can only be described by solving the Schrödinger equation in each layer as described in [6].

### 2.7.6 The PRISM Spectrometer

PNR on spin valves was carried out on the PRISM (polarised reflectometer for the investigation of surface magnetism) spectrometer at the LLB in Saclay, France. This spectrometer is mounted on the cold guide G2 of the Orphée neutron source at the LLB. The Orphée neutron source is a 14 MW steady state reactor generating a nominal flux of  $3 \times 10^{14}$  n/cm<sup>2</sup>. The spectrometer is especially adapted to the study of magnetic thin films and multilayers to determine their in-plane magnetic structure. The following description of the system refers to the schematic in Figure 2.12. A detailed technical description of the spectrometer can be found elsewhere [7].

The spectrometer operates at a fixed wavelength of 0.43 nm. The neutron beam from the reactor is monochromated at point M and deviated away from the main guide at D. The focussing guide at C reduces the height of the beam to 15mm at the sample position. The beam is polarised by transmission polarisers at P to  $-1/2$  neutrons. The beam can then be changed to  $+1/2$  by turning on the flipper F1, or left as  $-1/2$  depending on which measurement is being made. After reflection on the sample, the beam passes through another flipper F2, before passing to the reflection analyser and detector. A series of slits (S1-S4) collimate the beam throughout. The sample is aligned in the neutron beam and then the intensity reflected measured as a function of the incident angle,  $\theta$ . Four different measurements called  $R^{++}$  (up-up),  $R^{--}$  (down-down),  $R^{+-}$  (up-down),  $R^{-+}$  (down-up) can be made depending on the polarisation of the incident and reflected beams. These



measurements are arranged by appropriate switching of the flippers. The  $R^+$  and  $R^-$  measurements measure the spin flip intensity and are used when the sample magnetisation is not aligned with the neutron axis. An electromagnet around the sample position can be used to apply fields in the sample plane. A vacuum furnace ( $P < 10^{-6}$  mbar) with a heater with range of up to  $800^\circ\text{C}$  can be attached to the sample stage. Low temperature measurements can also be made with a cryostat. The typical reflectivity range is of the order of  $10^5$  to  $10^6$  for a  $1\text{cm}^2$  sample and a typical reflectivity curve takes 12 hours for a full scan. Fits to the experimental data were generated using the program Simulreflec [8].

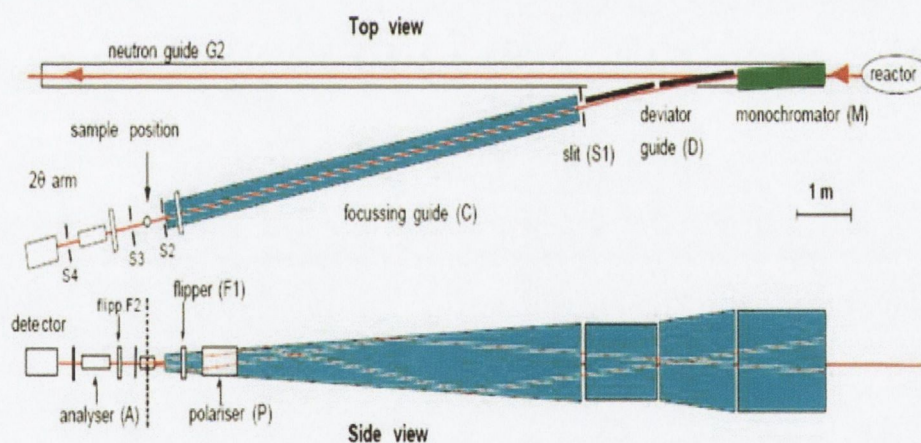


**Figure 2.12** Schematic of the experimental set-up: (a) top view, (b) side view. The different elements are: multilayer monochromator (M), deviator guide (D), focussing guide (C), collimation slits (S1-S4), flippers (F1 and F2), transmission polarizer (P) and reflection analyzer (A).

## 2.8 Fabrication of small magnetic structures

Reliable and reproducible fabrication of small magnetic structures is essential for the field of spin electronics, both for investigation of physical principles and for manufacture of marketable devices. The semiconductor industry has long established processes for the production of integrated circuits at sub-micron dimensions. These techniques such as optical and e-beam lithography are now being used to make magnetic prototype devices at the laboratory level. The integration of magnetic structures with semiconductor technology on a nanometer scale is a goal currently pursued with great vigour, particularly for applications in data storage and sensing device technology. In the case of MRAM, magnetic devices and CMOS logic have merged and are currently an area of intense research at industry level.

### 2.8.1 Optical Lithography

Optical lithography is a frequently used method for creating micron-sized magnetic structures. The basis of optical lithography is the transfer of a pattern designed on a mask onto a photosensitive resist covering the sample. For patterning magnetic structures there are two scenarios. In standard patterning the magnetic layer or multilayer is first deposited on the substrate and the pattern defined afterwards through a combination of photolithography and etching techniques. The alternative is the lift-off technique, whereby the pattern is defined in photoresist on a substrate and the magnetic layers are deposited on top and then partly removed by lift-off, leaving the required pattern. Optical lithography refers to the modification of the photoresist properties upon irradiation and is termed ultra violet (UV), x-ray or electron beam depending on the radiation used. Photoresist is a polymer material sensitive to radiation and can be positive or negative. Positive resist becomes soluble after exposure to radiation. Hence the areas exposed are removed.



Negative resist becomes less soluble after exposure so the unexposed areas are removed. Both positive and negative resists are available commercially.

In this work, UV lithography was used to make micron-sized spin valve lines with contacts on top for transport measurements. Defining the spin valve lines required a standard lithography process whereby the sample to be patterned (i.e. the spin valve stack) was deposited first. Six steps were involved as detailed in Figure 2.13. First the spin valve was deposited on a clean 4" Si/SiO<sub>2</sub> wafer by sputtering in the Shamrock sputtering tool. The spin valve was then taken to the class 100 lithography cleanroom. Here the wafer was cleaned with acetone, IPA and DI water and baked at 115°C to remove water vapour on an EMS 1000 hotplate. Positive photoresist Shipley S1813 was then spun on the wafer using an EMS 4000 spin coater which can spin from 1 to 9000 rpm and has 9 programmable steps. We used a 3 step process for spinning on 4" wafers which resulted in a resist thickness of ~1 µm. After spinning, the wafer was baked at 115°C for 2 minutes to remove the solvent in the photoresist. The pattern was exposed through a photomask using a Karl Suss MJB 3 mask aligner which uses UV light of wavelength  $\lambda = 250$  nm. Photomasks for UV lithography were designed using KIC software. The masks are quartz/chrome and were made commercially in Japan. The resolution of the mask aligner is 1 - 2 µm and while these sizes can be achieved, the difficulty is in achieving uniformity across a wafer. Resolution is also limited by vibrational noise and non-uniformity in the resist. Exposure time in the mask aligner was typically 3.5 seconds. The exposed resist was removed using developer MF319 for 40–60 seconds. The spin valve was then etched using ion beam etching (IBE) in a Millatron tool.

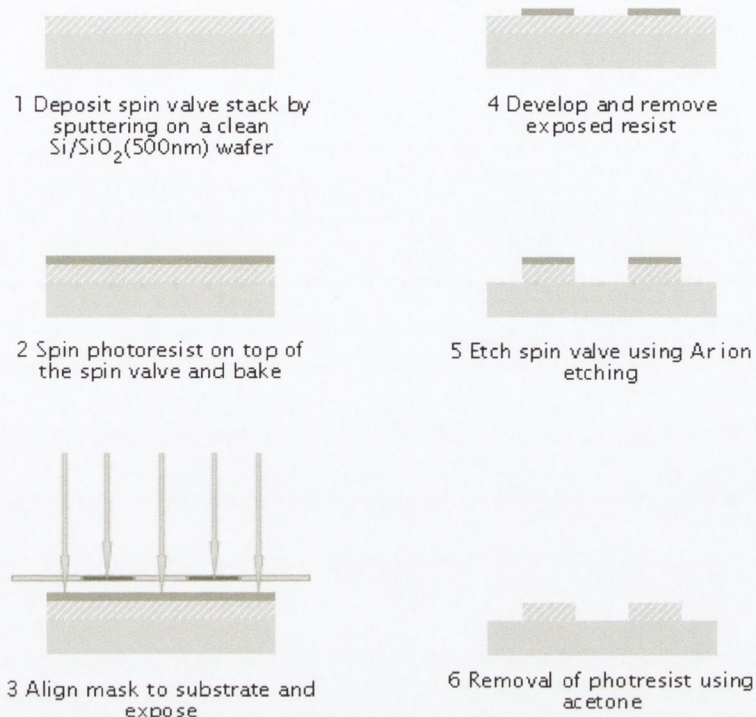


**Figure 2.13 Six steps involved in the standard patterning procedure**

Ion beam etching is a physical plasma process whereby ions are produced in a cavity and then accelerated to produce a relatively intense and homogeneous beam using an RF source. The ions effectively sputter away material not protected by photoresist on the sample. The advantage of the technique is anisotropic etching with high aspect ratios for effective pattern transfer. The Millatron system consists of a vacuum chamber with a rotational sample stage, an ion gun with an RF power supply, a DC supply which controls a magnet in the ion gun and a MFC with lets high purity Ar into the system. The base pressure of the system is typically  $2 \times 10^{-7}$  mbar and the working pressure is  $2 \times 10^{-5}$  mbar using 20 sccm of argon. RF power of 400 W is used with a magnet current of 3.5 A. The sample is rotated in a planetary fashion at  $45^\circ$  to the ion beam and the etch rate is material specific. The disadvantage of the system is the lack of an end-point detection device.



Etch-rates must be calibrated using AFM or profilometry on test samples, but can change over time. After etching in the Millatron, the final step is removal of the resist using acetone.

In order to define the contacts on top of the spin valve, a lift-off patterning process was necessary. In this case, the metallic layer is deposited after the photolithographic process as detailed in Figure 2.14. S1813 photoresist was respun on the patterned spin valve wafer and baked as before. The spin valve pattern contains several alignment crosses which are used to manually align the wafer with the mask for the next step in the mask aligner. The pattern is exposed after alignment for 3.5 seconds.

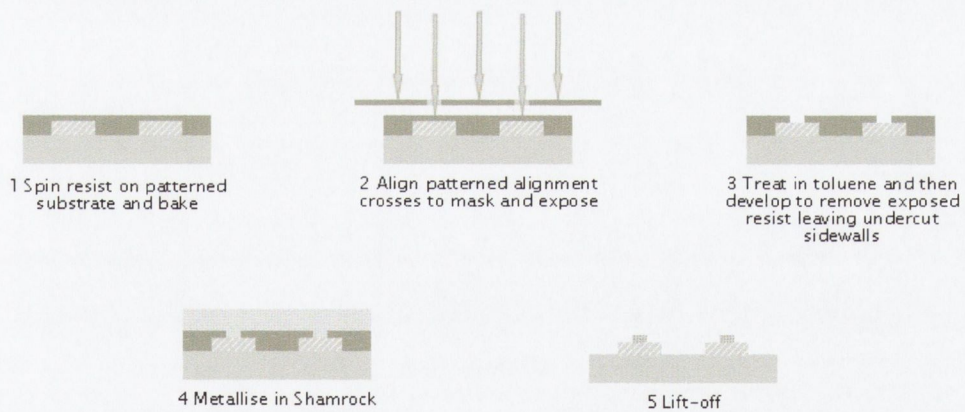


**Figure 2.14 5 steps for lift-off procedure**

In order to assist lift-off of the metal later-on, an extra development step is added. Treating the S1813 resist in toluene before development alters the side-wall profile so that when the resist is developed the side walls are undercut. This allows the resist and metal layer to be more easily removed with acetone. Samples were dipped in toluene for 2 minutes and then

developed for 40-60 seconds in MF319 developer. Wafers were then returned to the Shamrock for deposition of Ta5nm/Cu50nm for the contacts. The Ta is used to promote adhesion on the SiO<sub>2</sub>. The metal was then lifted off in acetone with ultrasonic.

### 2.8.2 Focused Ion Beam (FIB) tool

The FEI strata 235 dual beam FIB system consists of both a scanning electron microscope (SEM) and a focused ion beam and is shown in Figure 2.15. The electron column is used as a standard SEM for imaging purposes and is also equipped with the Raith Elphy Quantum conversion for electron beam lithography and an EDAX detector for elemental analysis. The ion column is situated at 52 degrees to the electron column. The operating principle is similar to that of the SEM except that a beam of ions rather than electrons is rastered over the sample. The ions are field extracted from a liquid gallium source and are then accelerated, collimated and focused by a series of apertures and electrostatic lenses. The accelerating potential typically varies from 5 - 30kV. Depending on the size of the aperture used and the strength of the lenses, beam currents from 1 pA - 50,000 pA with corresponding spot sizes of approximately 10nm - 50nm can be produced. The beam is raster-scanned over the sample, which is mounted in a vacuum chamber at a pressure of around 10<sup>-7</sup> mbar. When the beam strikes the sample, secondary electrons and ions are emitted from the surface. These electrons and ions are collected and used to generate an image of the surface. Image contrast results from topographic contrast and differences in secondary electron yield for different materials. The resolution of the system depends on the material being imaged and the spot size used. Optimum resolution is around 7 - 10 nm.



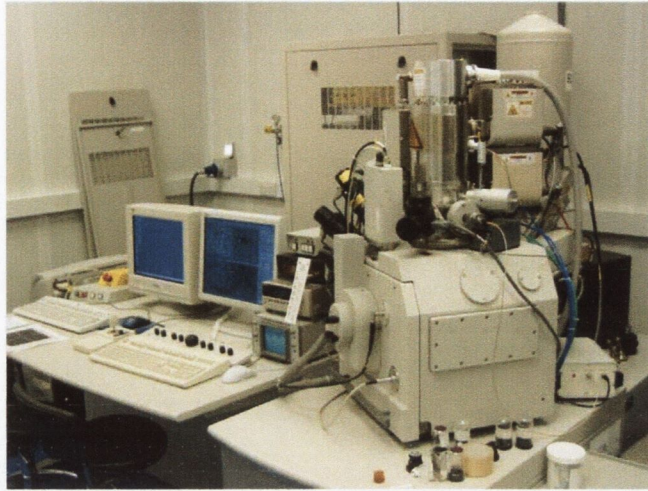


**Figure 2.15** The dual beam FIB tool in the Class 1000 cleanroom

The ion beam can be used to remove material from the sample. This ion beam milling process is used to create cross-sections for constructional and failure analysis of semiconductor devices and can be used to make samples for TEM analysis. Milling can be performed with the assistance of small quantities of gas. Gas is bled into the system via a needle and is adsorbed onto the sample surface where it reacts with the ion beam and surface material, producing volatile compounds that are pumped away. The system can also be used to deposit metals and insulators onto selected areas of a sample. This ion beam assisted deposition involves bleeding a suitable precursor into the chamber which is broken down by the scanning ion beam resulting in the metal (such as platinum) or insulator being deposited and the volatile products being pumped away. Ion beam lithography in resists such as PMMA is also possible in a similar manner to electron beam lithography. This has advantages in that the ion scattering in the resist and back scattering from the substrate are lower than in the case of an electron beam [9].

The capability to mill and deposit metals and insulators makes the FIB system highly versatile. One of the main disadvantages of the FIB as a milling tool is the effect of Ga<sup>+</sup> ion implantation. With a dual beam system this effect is reduced because the electron column can be used for imaging and alignment but the implantation during milling still plays a role. The effect of Ga<sup>+</sup> ion implantation from direct FIB milling of spin valves is discussed in Chapter 5.



## 2.9 References

---

- [1] ULSI Technology, S.M. Sze and C.Y. Chang (Eds) McGraw-Hill
- [2] See supporting online material in : M. Pannetier, C. Fermon , G. Le Goff, J. Simola, E. Kerr, *Science* **304**, 1648 (2004).
- [3] M. Hecker, X-ray scattering techniques, in: *Metal Based Thin Films for Electronics*, K. Wetzig, C.M Schneider (eds.), 158-174 (2003).
- [4] D.L. Windt, *Computers in Physics*, Vol. 12, No. 4, 360-370 (1998)
- [5] [www-llb.cea.fr](http://www-llb.cea.fr)
- [6] C.Fermon, Chapter in “X-ray and Neutron Reflectivity; Principles and Applications”, J. Daillant and A. Gibaud (eds.), Springer, Berlin (1999).
- [7] C. Fermon, F. Ott, G. Le Goff, H. Glättli, V. Wintenberger, *Rev. Sci. Inst.* **71**, 3797 (2000).
- [8] <http://www-llb.cea.fr/prism/programs/simulreflec/simulreflec.html>
- [9] R.M. Langford, A.K Petford-Long, M. Rommeswinkle, S. Egelkamp, *Materials Science and Technology*, **18**, 743, (2002).

## Chapter 3

# Characterisation of Spin Valves using Polarized Neutron Reflectometry

### 3.1 Introduction

Polarised neutron reflectometry (PNR) is a powerful tool for the investigation of magnetic thin films and multilayers. The large magnetic coupling between the neutron and the magnetic moment means that precise measurements of layer-resolved magnetic moment configurations can be obtained. The technique also yields precise information on the structural configuration such as individual layer thicknesses [1]. A variety of magnetic thin film systems such as superlattices and exchange bias systems have been studied using PNR [2] [3]. The reversal of the free layer in a spin valve has been investigated by PNR [4]. The purpose of this work was to characterise top IrMn spin valves. This spin valve structure has been implemented in a mixed sensor used for femtotesla magnetic field measurement described in Chapter 6. A detailed characterisation of the sample was therefore necessary. The aim was to determine the individual layer thicknesses of the structure and the magnetic moment in  $\mu_B/\text{atom}$  of the free and pinned layers of the spin



valve. The thermal stability of the spin valve was also investigated. Measurement of the spin flip signal allowed the magnetic stability of the pinned layer to be determined. The evolution of the crossed anisotropy configuration was followed as a function of temperature and applied magnetic field and reflectivity measurements at elevated temperatures were used to assess the long term stability of the structure.

## 3.2 Structural and magnetic characterisation of spin valves

### 3.2.1 Deposition and Magnetotransport

Spin valves of structure:

Ta(5nm)/NiFe(3.5nm)/CoFe(1.2nm)/Cu(2.9nm)/CoFe(2.5nm)/IrMn(10nm)/Ta(10nm) were deposited on 4 inch Si/SiO<sub>2</sub>(500nm) wafers in the Shamrock deposition tool. The spin valves were deposited with the anisotropy axes of the free and pinned layers perpendicular to one another. This was achieved by depositing in a field of 5 mT and rotating the sample by 90 degrees after the deposition of the Cu spacer layer. Deposition was at room temperature. The free layer reversal of the spin valve is shown in Figure 3.1 where the field is applied parallel to the pinned layer.

The crossed anisotropy configuration of the spin valve results in coherent rotation of the free layer during reversal and a near-linear response with very low coercivity. These properties will be further enhanced when the spin valve is patterned to smaller dimensions. The magnetoresistance ratio of the structure is 8 %. The coupling between the free and pinned layers results in an offset from zero field of 0.4 mT.

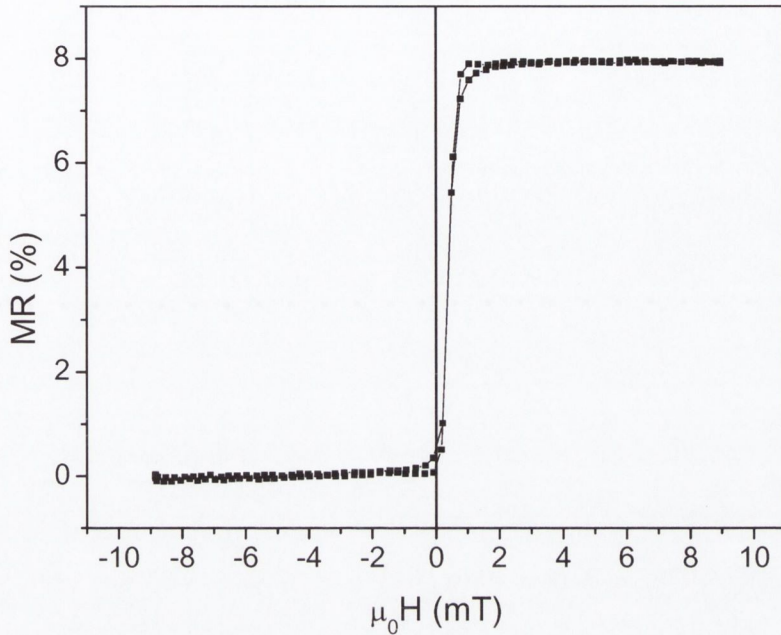


**Figure 3.1** Free layer reversal of crossed anisotropy spin valve structure

**Ta(5nm)/NiFe(3.5nm)/CoFe(1.2nm)/Cu(2.9nm)/CoFe(2.5nm)/IrMn(10nm)/Ta(10nm)**

### 3.2.2 Structural characterisation using X-Ray Reflectometry

Structural knowledge of the sample gained from another technique such as X-ray reflectivity is helpful when analyzing neutron reflectivity data. The X-ray reflectivity curve of the spin valve structure was measured as described in Chapter 2. The resulting curve with best fit is shown in Figure 3.2. From the XRR results we see that the thicknesses of the layers are close to the nominal values within the error. The curve is fit assuming that top 1 nm of the spin valve is oxidized. The 10nm Ta cap layer is more than enough to protect the spin valve. The XRR results also show that the roughness of the spin valves is low and the samples are of high structural quality.



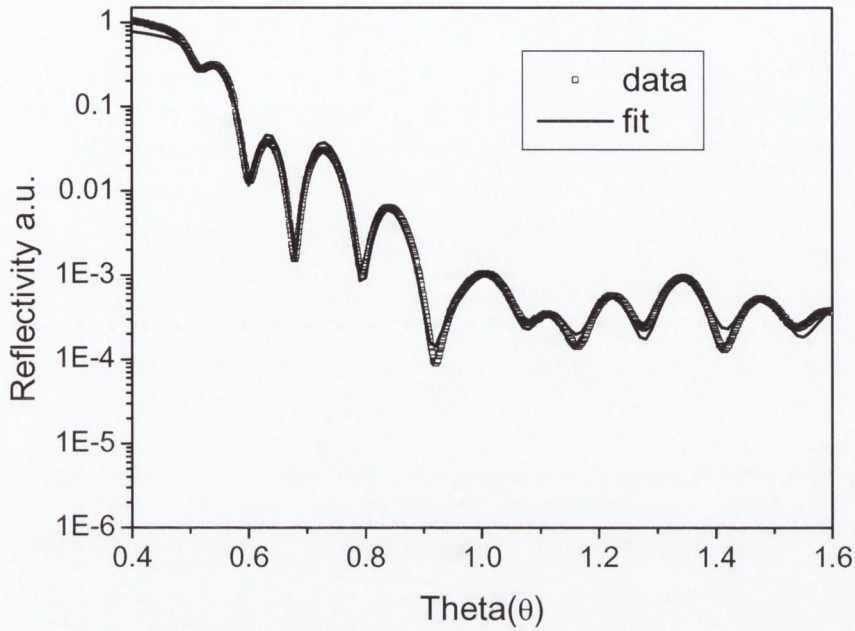


**Figure 3.2** XRR curve with fit of spin valve structure of Figure 3.1.

From the fit to the data, the layer thicknesses shown in Table 3.1 were determined.

	Ta	NiFe	CoFe	Cu	CoFe	IrMn	Ta	oxide
Thickness (nominal) in nm	5	3.5	1.2	2.9	2.5	10	10	0
Thickness (fit) in nm	5 (±0.5)	3.0 (±0.5)	1.5 (±0.2)	2.9 (±0.2)	2.7 (±0.2)	10.2 (±0.2)	10.0 (±0.5)	0.5 (±0.5)

**Table 3.1** Spin valve layer thicknesses as determined by fit to the x-ray reflectivity curve in Figure 3.2

### 3.2.3 Structural and magnetic characterisation using PNR

Polarised neutron reflectivity of the spin valve was carried out at the PRISM reflectometer at the LLB as described in Chapter 2. Spin valves with NiFe free layer thicknesses of 2 nm and 5 nm were also studied. Figure 3.3 shows the measurement configurations. A field of 5 mT was applied to saturate the magnetisation of the free layer parallel or antiparallel to the pinned layer and the reflectivity curves were measured in both configurations. As all of the magnetisation of the sample is aligned with the magnetic field and neutron axis, no spin flip signal is present in this configuration. The  $R^{++}$  and  $R^{-}$  cross sections were measured and fit using the program Simulreflec [5] in order to determine the thickness and composition of each layer and the magnetisation in  $\mu_B/\text{atom}$  of the magnetic layers. Figures 3.4 -3.6 show the resulting reflectivity curves with fits for three spin valves with different NiFe free layer thicknesses.

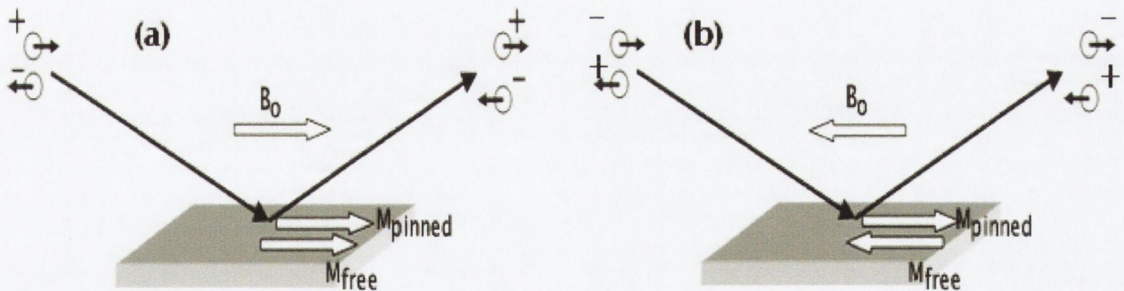
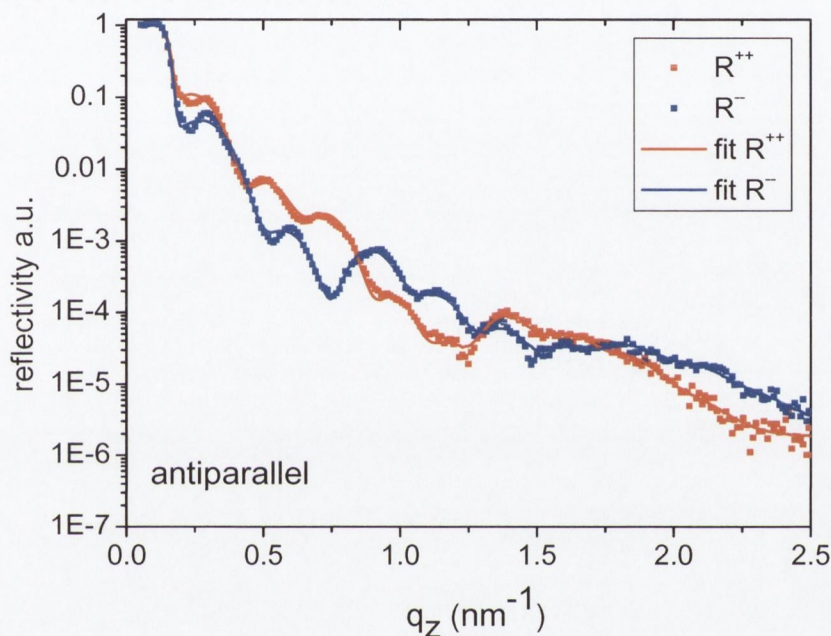


**Figure 3.3** Schematic showing spin valve measurement configuration for  $R^{++}$  and  $R^{-}$  intensities for free and pinned layer parallel (left) and free and pinned layer antiparallel (right).

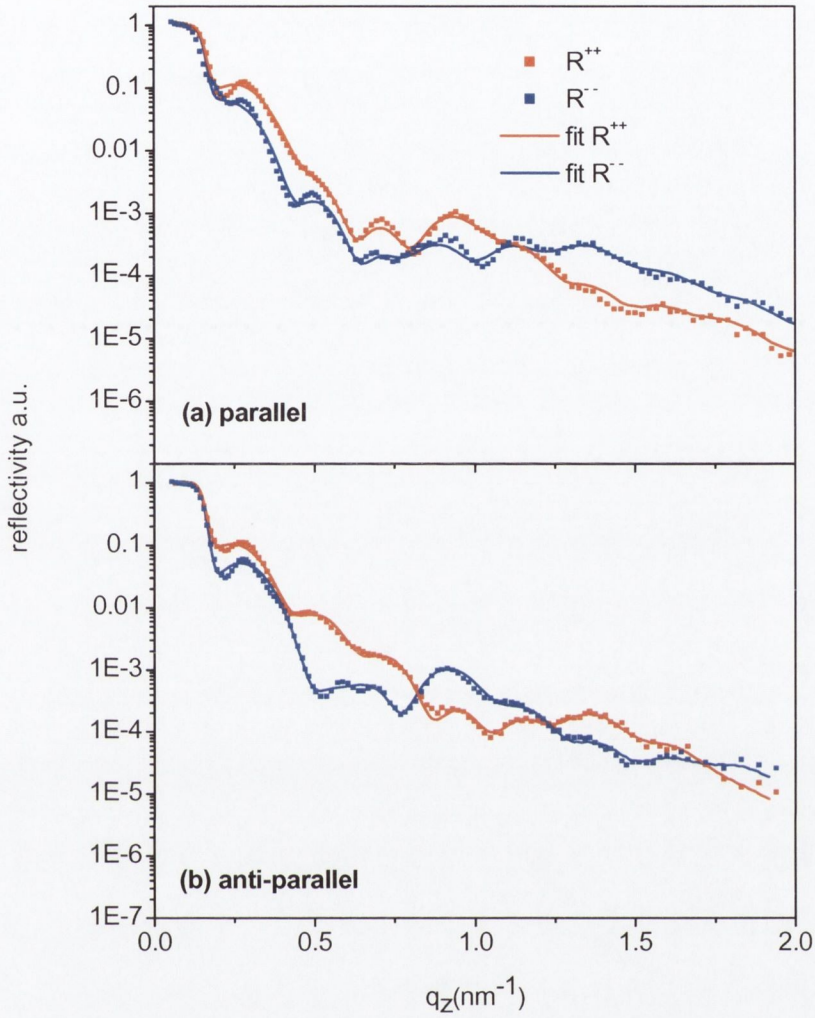


From the fit to the data we can see that the thicknesses of the individual layers are within 10 % of their nominal values. The high structural quality of the samples is indicated by the presence of oscillations at high angles. The magnetic moment of CoFe layers is around 1.5  $\mu_B$ /atom and NiFe is 1  $\mu_B$ /atom. The magnetic moment of the NiFe layer does not change as the thickness of the layer is changed.



	Ta	NiFe	CoFe	Cu	CoFe	IrMn	Ta	oxide
Thickness (nominal) in nm	5	2	1.2	2.9	2.5	10	10	0
Thickness (fit) in nm	5 ( $\pm 0.5$ )	2.3 ( $\pm 0.2$ )	1.2 ( $\pm 0.2$ )	2.4 ( $\pm 0.2$ )	2.7 ( $\pm 0.2$ )	10.4 ( $\pm 0.2$ )	10.9 ( $\pm 0.5$ )	1.0 ( $\pm 0.5$ )
Magnetisation (fit) in $\mu_B$ /atom	0	1.0 ( $\pm 0.2$ )	1.6 ( $\pm 0.2$ )	0	1.6 ( $\pm 0.2$ )	0	0	0

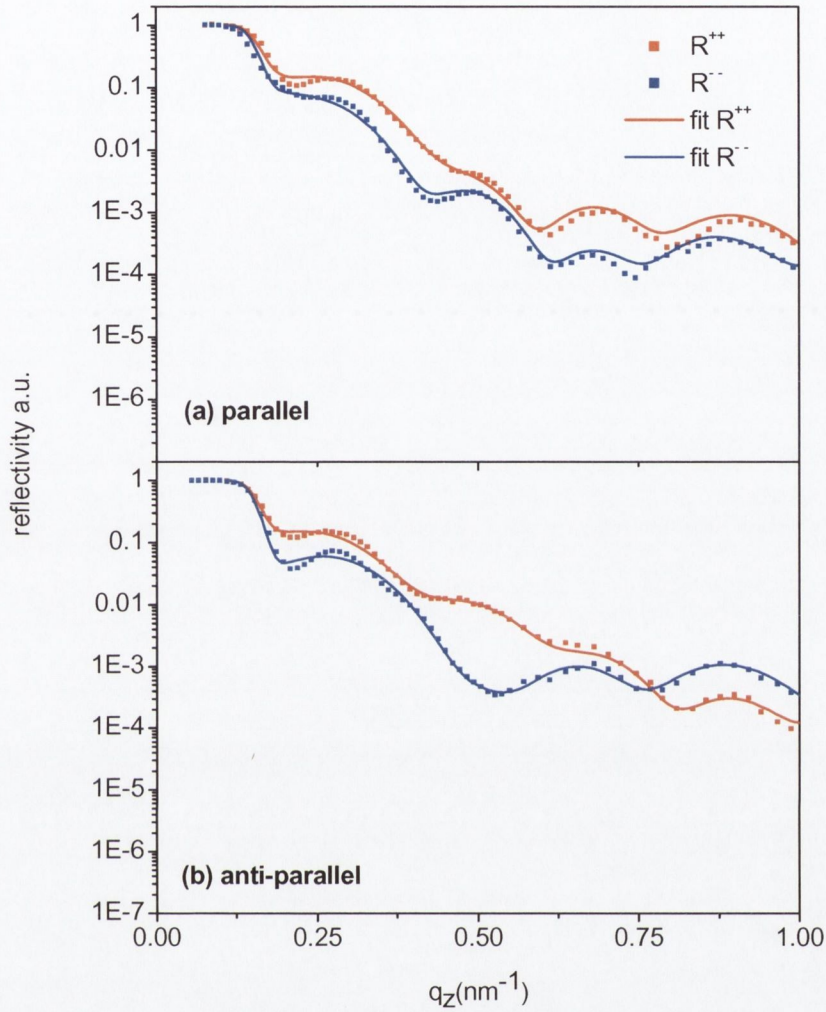
**Figure 3.4** Reflectivity curves for spin valve with  $t_{\text{NiFe}} = 2$  nm in the parallel (a) and antiparallel (b) configuration. Red squares  $R^{++}$ , blue squares  $R^{-}$ , best fit in red and blue lines. Table showing spin valve structure as determined by fits to the reflectivity curves.



	Ta	NiFe	CoFe	Cu	CoFe	IrMn	Ta	oxide
Thickness (nominal) in nm	5	3.5	1.2	2.9	2.5	10	10	0
Thickness (fit) in nm	5 (±0.5)	3.2 (±0.5)	1.2 (±0.2)	2.7 (±0.2)	2.9 (±0.2)	10.4 (±0.2)	10.9 (±0.5)	1.0 (±0.5)
Magnetisation (fit) in $\mu_B$ /atom	0	1.0 (±0.2)	1.6 (±0.2)	0	1.6 (±0.2)	0	0	0

**Figure 3.5** Reflectivity curves for spin valve with  $t_{\text{NiFe}} = 3.5$  nm in the parallel (a) and antiparallel (b) configuration. Red squares  $R^{++}$ , blue squares  $R^{--}$ , best fit in red and blue lines. Table showing spin valve structure as determined by fits to the reflectivity curves.





	Ta	NiFe	CoFe	Cu	CoFe	IrMn	Ta	oxide
Thickness (nominal) in nm	5	5	1.2	2.9	2.5	10	10	0
Thickness (fit) in nm	5 (±0.5)	4.6 (±0.2)	1.2 (±0.2)	2.9 (±0.2)	2.7 (±0.2)	10.2 (±0.2)	10.0 (±0.5)	1.8 (±0.5)
Magnetisation (fit) in $\mu_B$ /atom	0	0.9 (±0.2)	1.5 (±0.2)	0	1.5 (±0.2)	0	0	0

**Figure 3.6** Reflectivity curves for spin valve with  $t_{\text{NiFe}} = 5\text{ nm}$  in the parallel (a) and antiparallel (b) configuration. Red squares  $R^+$ , blue squares  $R^-$ , best fit in red and blue lines. Table showing spin valve structure as determined by fits to the reflectivity curves.

### 3.2.4 Measurement of the spin valve thermal stability

The neutron spin flip signal is sensitive to components of the magnetisation perpendicular to the applied field. This can be used to study magnetisation directions as a function of field or temperature. The  $t_{\text{NiFe}}=3.5$  nm spin valve was placed in the spectrometer in a vacuum furnace with a resistive heater and pumped down to  $10^{-6}$  mbar. The easy axis of the pinned layer was arranged perpendicular to the neutron quantization axis and a field of 1.3 mT was applied to saturate the free layer perpendicular to the pinned layer. The measurement configuration is shown schematically in Figure 3.7. In this configuration, a spin flip signal from the pinned layer should be measurable. In theory four cross-sections are measurable;  $R^{++}$ ,  $R^{-}$ ,  $R^{-}$ , and  $R^{+-}$ . In practice, the  $R^{+-}$  cross section is not measured as it should be identical to  $R^{+}$  for moderate external magnetic fields. Furthermore, it involves using both neutron flippers and a larger error is associated with the measurement.

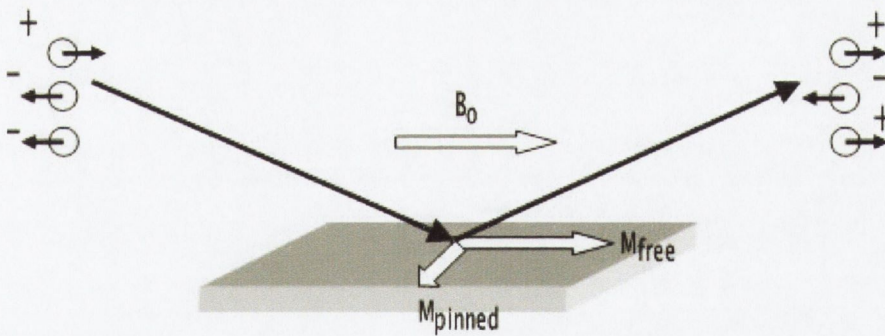


**Figure 3.7** Schematic showing spin valve configuration for spin flip measurement

The  $R^{++}$ ,  $R^{-}$ , and  $R^{+-}$  signals were first measured at room temperature. The resulting reflectivities in an applied field of 1.3 mT are shown in Figure 3.8. The presence of the spin-flip  $R^{+-}$  curve indicates that the free and pinned layers are not collinear. The spin-flip signal shows a maximum at around 0.25 degrees theta. The amplitude of this maximum is indicative of the angle between the magnetisation of the pinned and free layers.



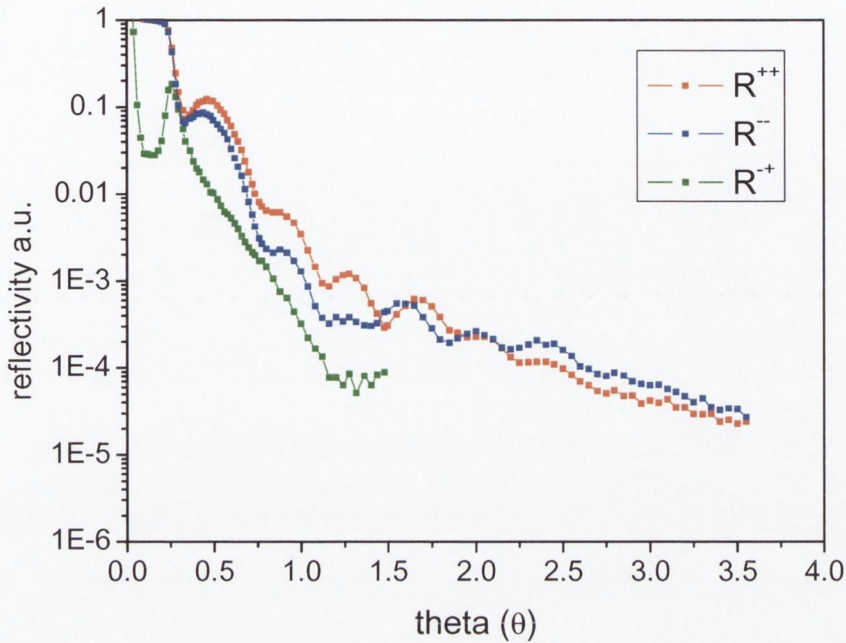


**Figure 3.8** Spin valve reflectivity with spin flip for  $t_{\text{NiFe}} = 3.5\text{nm}$  at room temperature with a 1.3mT applied field along the easy axis of the free layer, perpendicular to the pinned layer.

The amplitude of the spin flip maximum at  $\theta = 0.25$  was then measured as a function as the applied field along the easy axis of the free layer at room temperature. The resulting curve is shown in Figure 3.9. From this, it is clear the pinned CoFe layer begins to rotate at very small perpendicular applied fields and at an applied field of 6 mT, the spin flip signal has already decreased by half. This suggests that the CoFe layer is not very strongly pinned. One possibility is that not all of the thickness of the CoFe is pinned and part of it rotates with the field, creating a rotation within the film. The gain in energy from adopting this configuration is the Zeeman energy,  $-M\mu_0 H \cos(\theta)$ , where  $\theta$  is the angle between the magnetisation,  $M$ , and the applied field  $\mu_0 H$ . This gain will be much less than the cost of

exchange energy  $+J \cos^2 \vartheta$  used to create a rotation of the CoFe moments within the thickness of the film. It is more likely that the pinning across the area of the film is inhomogeneous and weakly pinned areas rotate with the field creating domains within the film. The stability of the magnetisation of the pinned layer against magnetic fields along directions other than its easy axis is important for sensor applications.

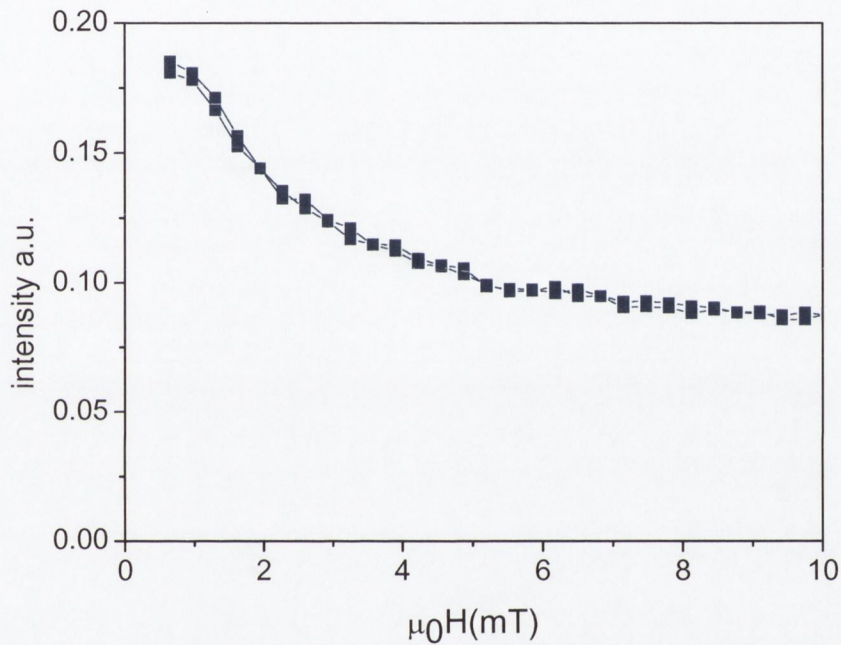


**Figure 3.9 Intensity of the spin flip signal at 0.25 theta as a function of the magnetic field applied along the easy axis of the free layer**

The amplitude of the spin flip signal as a function of the field applied along the easy axis was then followed as the temperature of the furnace was increased. The temperature of the furnace heater was programmed to increase in approximately 10 °C steps from room temperature to 215 °C. When the read out of the thermocouple had stabilized the spectrometer measured the spin flip signal as function of applied field. The resulting



curves for different temperatures are shown in Figure 3.10. From these curves, it is clear that the intensity of the spin flip maximum decreases as the temperature is increased. This shows that the CoFe pinned layer rotates more easily towards the free layer as the temperature is increased. Between 190 °C and 200 °C, the spin flip maximum disappears. At this point the exchange coupling between the IrMn and the CoFe has broken down and the pinned layer has rotated and is nearly parallel to the free layer. At 200 °C, the shape of the spin flip curve has changed due to the fact that the blocking temperature of the IrMn has been reached. The pinned layer has undergone a complete and irreversible rotation at this point. The spin flip signal is not restored after cooling the sample back to room temperature. This experiment reveals that the blocking temperature of the IrMn layer in these spin valves is around 200 °C. This is lower than values of up to 250 °C for IrMn reported in the literature and limits the high temperature applications of these structures.

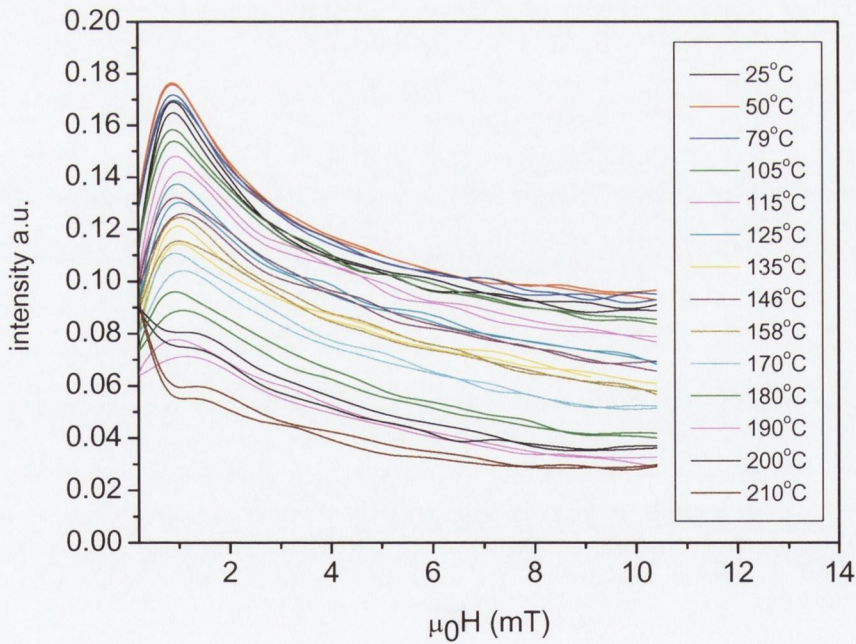


**Figure 3.10** Intensity of the spin flip signal at  $\theta = 0.25$  as a function of the magnetic field applied along the easy axis of the free layer for furnace temperatures from 25 °C to 210 °C.

With the magnetisation of the free and pinned layers aligned parallel to one another, as shown in Figure 3.3(left), the temperature of the furnace was left at 185°C overnight and the reflectivity curve measured at 3 hour intervals. The purpose of this was to assess any structural changes in the spin valve over time at elevated temperatures. The magnetoresistance and exchange bias of spin valves can deteriorate after prolonged temperature treatments due to interdiffusion between layers and an increase in roughness. In spin valves with Mn-based antiferromagnets, Mn diffusion to the active CoFe/Cu/CoFe region is a particular problem [6]. Diffusion of atoms and an increase in roughness would manifest as a change in the neutron reflectivity curve of the sample over time. Figure 3.11 shows the room temperature reflectivity curve for the spin valve and the curves at 185°C measured at 3 hour intervals throughout the night. No significant change in the reflectivity curve is evident. From this we can conclude that at this temperature, the spin valve has not undergone significant structural changes.

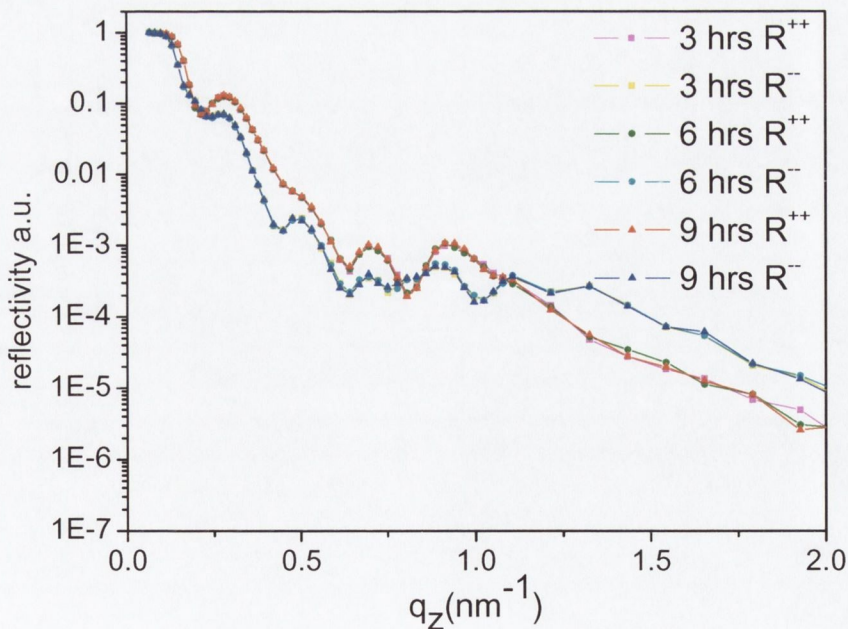


Figure 3.11 Reflectivity curves for spin valve heated at 185°C overnight.



### 3.3 Conclusion

Spin valves have been characterised using polarized neutron reflectometry. The individual layer thicknesses and magnetic moments of the free and pinned layers have been determined with sub-nanometer resolution. The layer thicknesses are in good agreement with the nominal values and the structural quality of the samples is high. The stability of the pinned layer in the presence of magnetic fields perpendicular to the exchange bias direction was assessed by measuring the spin flip signal as a function of field applied along the easy axis of the free layer. This has shown that at room temperature, part of the CoFe layer can rotate away from the exchange bias direction at very small fields. This suggests that the pinning is not very stable and is inhomogeneous. This has implications for application of the structure where fields perpendicular to the exchange bias direction are present, in measurements of the Earth's magnetic field for example.

The thermal properties of the spin valve were determined by analysis of the neutron spin flip signal as a function of temperature and magnetic field. At elevated temperatures, the pinned layer gradually rotates towards the free layer and the crossed anisotropy configuration of the spin valve is compromised. At 200 °C a complete and irreversible rotation of the pinned layer has occurred as the blocking temperature of the IrMn layer has been reached. The exchange bias is not restored after cooling to room temperature. The blocking temperature of 200 °C is lower than previously reported values for IrMn and therefore the high temperature applications of the structure are limited. The structural integrity of the spin valve stack was maintained after prolonged heating below the blocking temperature at 185 °C. At this temperature, significant interdiffusion of the layers does not occur. This characterisation provides essential information for the implementation of these structures as sensors.

### 3.4 References

---

- [1] C.Fermon, Chapter in “X-ray and Neutron Reflectivity; Principles and Applications”, J. Daillant and A. Gibaud (eds.), Springer, Berlin (1999).
- [2] F. Ott, F. Cousin, A. Menelle, *J. All. Comp.* **382**, 29 (2004).
- [3] H. Zabel, K. Theis-Brohl, *J. Phys. Condens. Matter* **15**, S505 (2003).
- [4] M. Pannetier, T.D. Doan, F. Ott, S. Berger, N. Persat, C. Fermon, *Europhys. Lett* **64**, 524 (2003).
- [5] <http://www-llb.cea.fr/prism/programs/simulreflec/simulreflec.html>
- [6] M. Takiguchi, S. Ishii, E. Makimo, A. Okabe, *J. Appl. Phys.* **87**, 2469 (2000).



## Chapter 4

# Influence of the Annealing Field Strength on Exchange Bias and Magnetoresistance of Spin Valves with IrMn

### 4.1 Introduction

For read head and other magnetic sensor applications, magnetic spin valve stacks with large exchange bias field ( $H_{ex}$ ) and high magnetoresistance (MR) values are required. Spin valves with a CoFe/IrMn top layer usually exhibit good magnetotransport characteristics in the as-deposited state, whereas spin valves with an IrMn/CoFe bottom layer normally require magnetic field annealing to establish large exchange bias. After magnetic annealing, however, the exchange bias field of bottom-pinned films often exceeds that of top-pinned films [1,2,3]. The reasons for this discrepancy and, more generally, the origin of the exchange bias effect have been studied in detail. Many groups have found a strong correlation between  $H_{ex}$  and the degree of crystalline texture [1,2,3,4,5]. Particularly in the case of bottom spin valves with IrMn, it has been observed that the exchange bias and the degree of (111) texture improves after annealing. In other work however, a correlation

between these parameters was not found and the exchange bias was attributed to structural parameters such as grain size [2,6,7,8] and interface roughness [2,9]. Ro *et al* concluded that  $H_{ex}$  is not related to (111) texture but depends on the grain size and morphology at the interface. Pakala *et al* investigated the effects of roughness, grain size and texture on IrMn/CoFe bilayers. By using different underlayers and varying the roughness they discovered that the exchange bias of the top configuration decreases with increasing roughness and no correlation with (111) texture was observed. In contrast the exchange bias of the bottom structures was correlated to (111) texture but not with roughness. Some authors argue that the difference between the top and bottom configurations is a magnetic effect resulting from the deposition configuration. Usually, top and bottom-pinned configurations are deposited in a small magnetic field ( $\sim 5$  mT). The higher exchange bias of the as-deposited top-pinned structure can be attributed to the growth of the antiferromagnet on a saturated magnetic layer resulting in a more oriented FM/AFM interface. In the case of the bottom-pinned structures however, the ferromagnet to be pinned grows on top of a randomly oriented antiferromagnet and the interface is less oriented. Malinowski *et al* [10] argue that the magnetic nature of the FM/AFM interface is imprinted during deposition and determines the subsequent field annealing effect. The interface of the poorly oriented bottom-configuration is more easily altered with subsequent annealing treatments whereas the magnetic configuration of the top-pinned interface is locked and not easily altered with further annealing. This suggests that deposition in a magnetic field may not be the route to high exchange bias and also that the strength of the annealing field may have an influence post-deposition. The magnetic field annealing experiments in most studies is focused primarily on the optimisation of the annealing time and temperature. On the other hand, the influence of the annealing field strength on exchange bias and MR is less well studied. In fact, it is common practice to anneal laboratory spin valve stacks in relatively small magnetic fields of several hundred



mT. Much larger fields, in the range 1 - 5 T, are used for industrially produced read-heads. It is generally believed that the exchange bias is predominantly determined by the magnetisation state of the ferromagnetic layer and that the strength of the annealing field is irrelevant as long as it saturates the ferromagnetic layer [11,12]. Reports to the contrary include a study on NiFe/CoO bilayers where the exchange bias was studied as a function of the applied cooling field when cooling below room temperature and  $H_{ex}$  was found to increase with increasing cooling field [13]. In a study on IrMn/CoFe bilayers by van Driel et al [3] it was found that the exchange bias was considerably enhanced after cooling from 580 K in a 2.5 T field as compared to cooling from 460 K or 620 K in a 19 mT field. The authors expect that the positive effect of the larger applied field on the exchange bias interaction is possibly due to a direct influence on the magnetic moments in the antiferromagnetic layer itself.

In this chapter, the influence of the annealing field strength on the exchange bias and MR of four different types of spin valves is examined. The annealing field in our experiment ranges from 0.05 T to 5.5 T. In particular, we find that annealing fields of several T can improve the magnetotransport properties of spin valves with an IrMn-pinned ferromagnetic layer at the bottom.

## 4.2 As-deposited spin valves

The four different spin valve structures under investigation are shown in Figure 4.1. The spin valves were grown by dc magnetron sputtering at room temperature on SiO<sub>2</sub> substrates in the Shamrock deposition system. To establish exchange bias, an in-plane magnetic field of 5 mT was applied during deposition. The structures were deposited in the parallel anisotropy configuration, i.e. the exchange bias direction and the growth induced easy axis of the free layer were parallel.

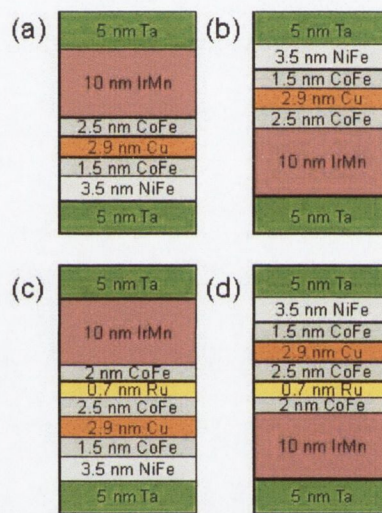


**Figure 4.1 Spin-valve structures: (a) top spin valve (TSV), (b) bottom spin valve (BSV), (c) synthetic antiferromagnetic top spin valve (SAFTSV), and (d) synthetic antiferromagnetic bottom spin valve (SAFBSV).**

The magnetotransport and SQUID data for the as-deposited TSV and BSV structures are shown in Figure 4.2. For the top spin valve (Figure 4.1a,b) at high negative fields the magnetisation of the free and pinned layers are saturated with the field and the resistance is low. At close to zero field, the magnetisation of the free NiFe/CoFe bilayer switches and the resistance increases. The coercivity of the free layer ( $H_c$ ) is 0.25 mT and the magnetoresistance ratio at this point is 7.4 %. At a higher positive field, the magnetisation



of the pinned layer gradually rotates with an exchange field ( $H_{ex}$ ) of 34 mT. The exchange bias of the structure can be described according to equation (1.11).

$$H_{ex} = \frac{J_{ex}}{M_{FM}t_{FM}}$$

This gives a value 0.125 mJ/m<sup>2</sup> for the exchange coupling energy  $J_{ex}$  for these structures. Values ranging from 0.12 mJ/m<sup>2</sup> to 0.4 mJ/m<sup>2</sup> have been reported for the CoFe/IrMn interface in the literature [14].

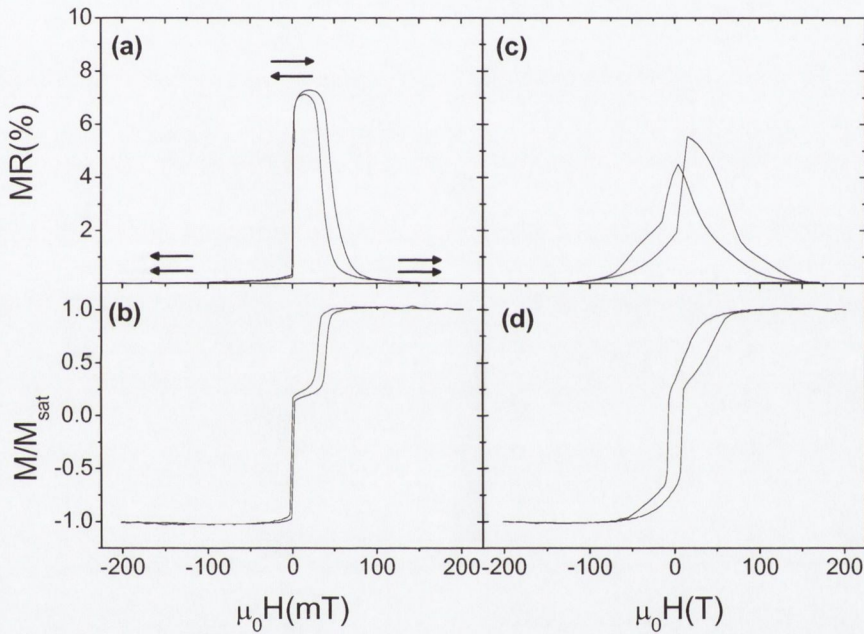


**Figure 4.2 Magnetotransport and SQUID magnetisation curves for the as-deposited TSV ((a) and (b)) and BSV ((c) and (d)) structure.**

The switching of the BSV structure is less well defined in the as-deposited state (Figure 4.1c,d). The exchange bias field is only 23 mT and the coercivity of the free layer is 7 mT. The drastically smaller difference between  $H_{ex}$  and  $H_c$  for the bottom-pinned spin valve leads to simultaneous magnetisation reversal of the free and pinned ferromagnetic layers.

This means that a full antiparallel configuration of the layers is not realized and the MR is reduced to only 5.0 %.

The magnetotransport and SQUID curves for the SAFTSV and SAFBSV structures are shown in Figure 4.3. The basic structure of the top SAF spin valve is F/Cu/AP1/Ru/AP2/AFM where F is the free layer and AP1 and AP2 are two CoFe layers antiferromagnetically coupled through a thin Ru layer. The coupling across the CoFe layers oscillates from ferromagnetic to antiferromagnetic with the thickness of the Ru layer. One of the CoFe layers, AP2, is exchange biased by an adjacent antiferromagnetic layer, AFM. In Figure 4.3a, the arrows indicate the magnetisation directions of F (bottom arrow), AP1 and AP2 (top arrow) during reversal for the top SAF structure.

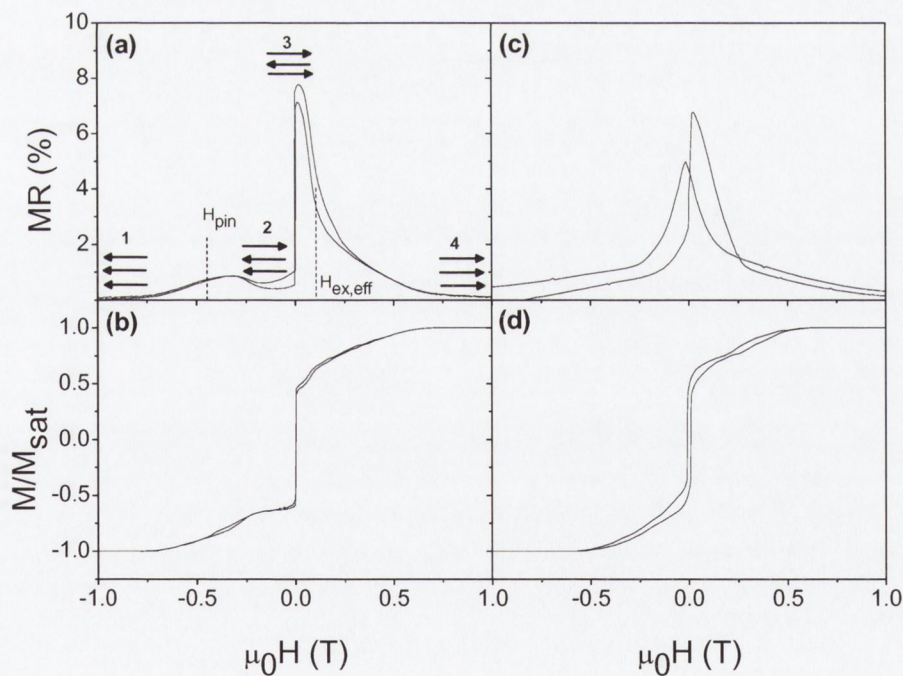


**Figure 4.3** Magnetotransport and SQUID magnetisation curves for the as-deposited SAFTSV [(a) and (b)] and SAFBSV [(c) and (d)] structures.



In region 2 at close to zero fields, AP1 and AP2 are coupled antiferromagnetically. The application of a small positive field switches the magnetisation of the free layer. At this point (region 3), maximum antiparallel alignment is obtained and the MR of the structure reaches its peak value of 8 %. At higher positive fields the antiferromagnetic coupling between AP1 and AP2 is gradually overcome as AP1 switches and the magnetisations of all the layers are aligned with the field at region 4. Between regions 2 and 3, the pinned layer AP2 reverses against the coupling to the antiferromagnet and the coupling through the Ru layer and a spin flop transition occurs with a small increase in resistance.

The effective exchange bias field of this structure,  $H_{eff,ex}$ , measured at the positive field where the MR has decreased by half its maximum value, is 112 mT. At this field, AP1 gradually overcomes the antiferromagnetic coupling energy,  $J_{Ru}$ , with AP2 across the Ru layer. The effective exchange field can be approximated by [15]:

$$H_{eff,ex} = \frac{J_{Ru}}{M_{AP1}t_{AP1}} \quad (4.1)$$

which gives a value of 0.33 mJ/m<sup>2</sup> for the exchange coupling across the Ru layer. This is considerably larger than the exchange coupling at the CoFe/IrMn interface of the standard spin valve and explains why the pinning field of the SAF spin valve is higher. When AP2 reverses at negative fields (between regions 1 and 2 in Figure 4.3a), it does so against the exchange coupling energy with the antiferromagnet,  $J_{ex}$  and the exchange energy across the Ru layer  $J_{Ru}$ . The field is often called the pinning field  $H_{pin}$  and can be estimated from:

$$H_{pin} = -\left( \frac{J_{Ru} + J_{ex}}{M_{AP2}t_{AP2}} \right) \quad (4.2)$$

Inserting our values for  $J$  and  $J_{ex}$  gives a calculated value of 160 mT for  $H_{pin}$ . This is consistent with the experimentally observed switching fields in the SQUID and transport curves of Figure 4.3a,b. This simple model can be used to understand the switching of the different layers of the SAF structure. A full analytical calculation of the magnetoresistive response of spin valves with a SAF can be found in [16].

The switching of the bottom spin valve with a SAF is not well defined in the as-deposited state (Figure 4.3c,d). The exchange bias direction is not well established and the free layer coercivity is large. The free and pinned layers switch simultaneously in a similar manner to the standard bottom spin valve leading to reduced MR of 6.8 %. The as-deposited MR of both structures with the SAF is higher than that of the standard structures.

### 4.3 Influence of the annealing temperature

The effect of annealing temperature on the exchange bias and magnetoresistance of the spin valves was investigated. Post-deposition magnetic annealing was performed in a vacuum furnace which was specifically designed to fit into a superconducting magnet as described in Chapter 2. The annealing field and temperature were varied from 0.05 T to 5.5 T and 180 °C to 300 °C respectively. The typical temperature and field ramp-up time was 30 minutes, after which the samples remained at the annealing temperature for 1 hour. Thereafter, the samples were field cooled to room temperature. The annealing field was aligned parallel to the growth-induced exchange bias direction. The spin valves were first annealing at a constant field of 5.5 T and varying temperatures in order to determine the optimum temperature for the subsequent effect of annealing field experiment.



Field annealing for one hour in a magnetic field of 5.5 T changes the MR and the exchange bias field of both the TSV and BSV structures. Figure 4.4 shows the dependence of  $H_{ex}$  and MR on the annealing temperature. Both the exchange bias field and the MR of the top-pinned spin valve decrease upon magnetic field annealing. While the exchange bias field is approximately independent of the annealing temperature ( $\mu_0 H_{ex} \approx 25$  mT), the MR decreases monotonically with increasing annealing temperature from 7.3 % at 180 °C to 3.5 % at 300 °C. Contrary to the TSV structure, the exchange bias field and MR of the bottom-pinned spin valve increase upon magnetic field annealing. For the BSV structure  $\mu_0 H_{ex} = 40$  mT after annealing at 180 °C, which is larger than the exchange bias field of the TSV structure before annealing. However, above 180 °C the exchange bias field decreases monotonically with increasing temperature and finally it becomes smaller than its pre-annealing value when the annealing temperature is larger than 270 °C. The MR of the BSV structure is about 8.5 % independent of the annealing temperature and the coercivity of the free CoFe/NiFe bilayer is 7 mT.

The experiments reveal that the exchange bias field and the MR of the BSV structure are larger than that of the TSV structure after magnetic field annealing. Although the difference in exchange bias between IrMn bottom-pinned and IrMn top-pinned bilayers has often been attributed to the degree of (111) film texture [1,2,3,4,5], we found no evidence for this in our experiments. XRD measurements on the as-deposited and annealed samples reveal that the IrMn layer in the top structures is (111) textured, but no (111) peaks were measured on the bottom spin valve films. This clearly indicates that a (111) crystalline film texture is not an essential prerequisite for large exchange bias fields. The magnitude of the exchange bias in the TSV and BSV structures is more likely determined by grain size, interface roughness, and defects at the CoFe/IrMn interface and in the IrMn bulk. The lack of (111) texture in the bottom structures can explain the large coercivity of the

free layer as growth of a free layer with (111) texture leads to good soft magnetic properties [17].

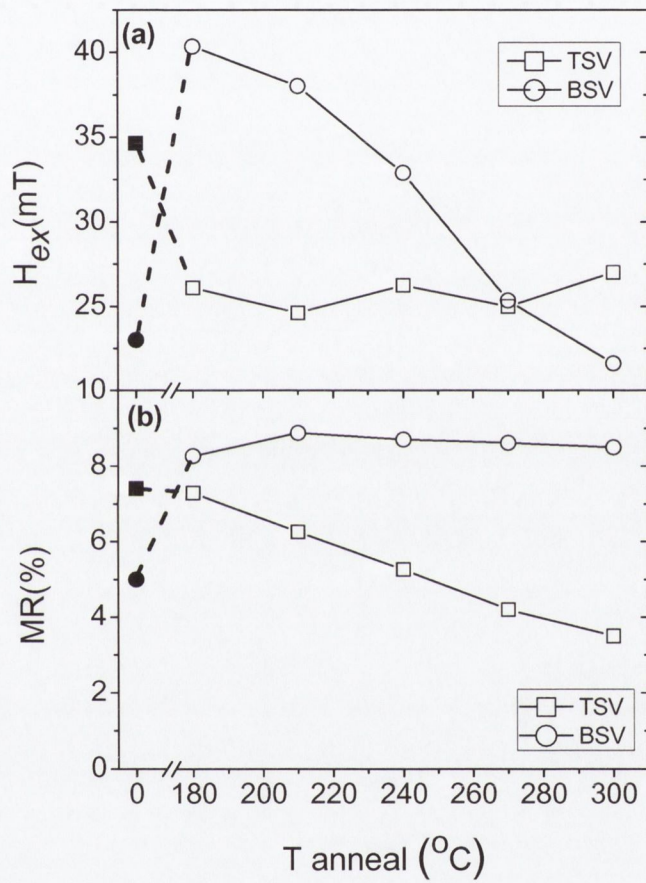


**Figure 4.4** Annealing temperature dependence of the exchange bias field (a) and MR (b) of the TSV and BSV structure. The annealing field was 5.5 T. The filled symbols indicate the as-deposited values.

Another remarkable difference between the TSV and BSV structures is the dependence of the MR on the annealing temperature. While the MR of the bottom-pinned spin valve is



approximately constant for annealing temperatures between 180 °C and 300 °C, the MR of the top-pinned spin valve decreases rapidly with temperature. Since the MR originates predominantly from spin-dependent electron scattering at the CoFe/Cu interfaces, any change in MR indicates a thermal modification of these interfaces. The diffusion of Mn atoms from the IrMn layer to the CoFe/Cu interfaces is a thermally activated process that is different for TSV and BSV structures. Top-pinned CoFe/IrMn interfaces have been found to be less stable against Mn outdiffusion than bottom-pinned IrMn/CoFe interfaces [18]. The decrease of MR for the TSV structure can therefore be due to Mn diffusion towards the CoFe/Cu interfaces. The onset of this effect appears to be at temperatures close to 210 °C. This is consistent with the results from the polarized neutron reflectometry experiment reported in Chapter 3 where structural deterioration of the top spin valve was not evident at a temperature of 185 °C. A similar Mn diffusion related deterioration of the MR has been measured on magnetic tunnel junctions with a CoFe/IrMn top electrode [19,20].

Annealing at 210 °C in a 5.5 T field does not have a large effect on the SAFTSV (Figure 4.9a). The exchange field is slightly reduced and the MR remains almost the same. The effect on the SAFBSV is more pronounced with a large increase in MR from 6.8 % to 9.1 % and an increase in exchange field (Figure 4.5b). However, simultaneous switching of the free and pinned layers still occurs after annealing and the exchange bias is not fully established. Figure 4.6 shows the temperature dependence of the MR and the exchange bias field for the SAF structures.  $H_{ex}$  and MR of the top structures decrease as the temperature is increased. The MR decreases with increasing temperature from 8.1 % to 5.2 %. The decrease in MR with temperature is not as pronounced as the decrease for the standard spin valve. The reduction of MR of the structure is likely to be due to Mn diffusion into the active region, as in the case of the TSV. The effect of diffusion is expected to be somewhat diminished in these structures as the Ru layer can act as a barrier

to the Mn [21]. Hence the SAF structure is more thermally stable with MR of 5.2 % after annealing at 300 °C compared to only 3.5 % for the TSV. The MR of the BSVSAF structure increases after annealing to over 9% and remains higher than its as-deposited value and higher than the MR of the top pinned SAF structure at all temperatures. Overall,  $H_{ex}$  is lower than the as-deposited value after annealing. The values of  $H_{ex}$  are calculated at half the value of the MR. In the case of the SAFBSV, this value is a combination of the switching of the free and pinned layers and is not fully representative of the exchange bias.

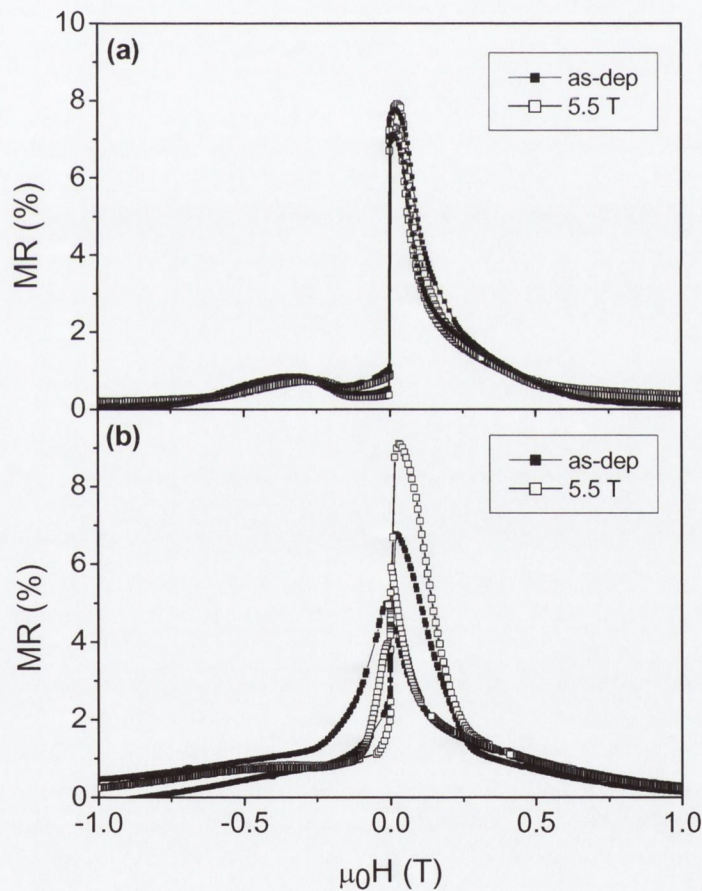


**Figure 4.5** Magnetotransport curves for SAFTSV (a) and SAFBSV (b) as-deposited and after annealing at 210 °C in a field of 5.5 T.



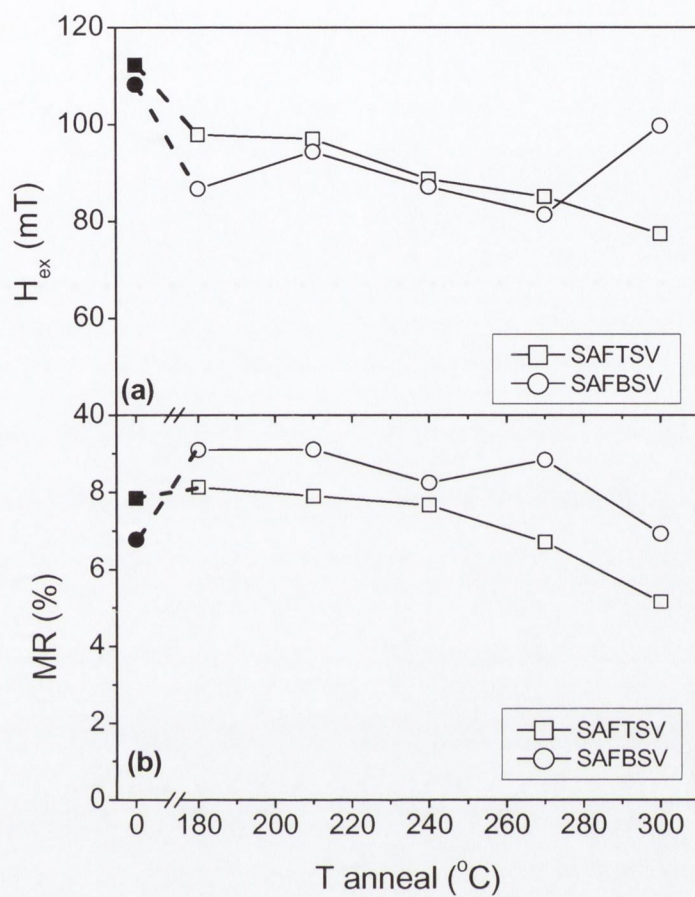


**Figure 4.6** Annealing temperature dependence of the exchange bias field (a) and MR (b) of the SAFTSV and SAFBSV structures. The annealing field was 5.5 T. The filled symbols indicate the as-deposited values.

#### 4.4 Influence of the annealing field

Based on the effects of annealing temperature on the spin valves, the temperature was fixed at 210 °C in order to study the influence of the strength of the annealing field. The annealing field was varied from 0.05 T to 5.5 T. Figure 4.7 shows the SQUID magnetisation curves and magnetotransport loops for the TSV structure before and after magnetic field annealing. The exchange bias field and MR of the top-pinned spin valve decrease upon annealing and the deterioration of the spin valve properties is similar for annealing in different fields.

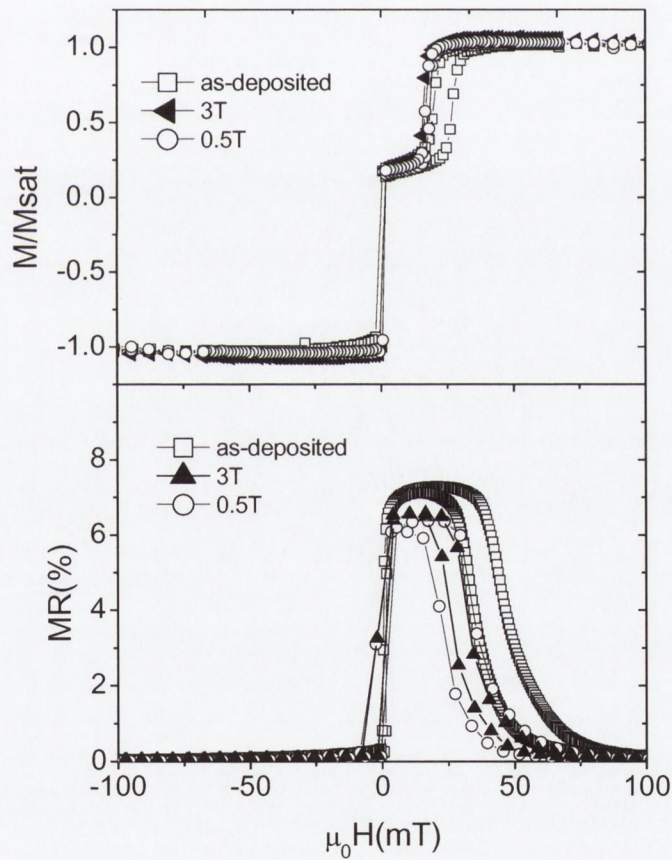


**Figure 4.7** Normalized magnetisation and magnetotransport curves for the TSV structure before and after annealing in different magnetic fields.



The magnetotransport properties of the annealed bottom-pinned spin valve, however, depend strongly on the magnetic field strength as shown in Figure 4.8. Although annealing in a field of 0.05 T already improves the MR from 5.0 % to 7.8 %, it only slightly increases the exchange bias field. The exchange bias field of the BSV structure improves rapidly with increasing magnetic field strength up to a field of about 0.5 T. Above 0.5 T the exchange bias field increases more gradually with annealing field and so does the MR.

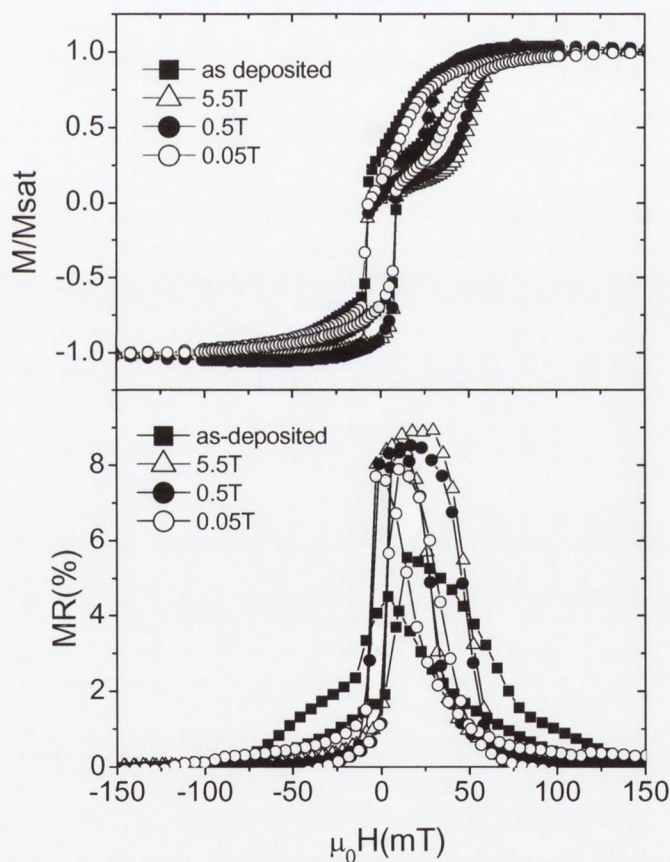


**Figure 4.8** Normalized magnetisation and magnetotransport curves for the BSV structure before and after annealing in different magnetic fields.

The influence of the annealing field strength on the exchange bias field and MR of TSV and BSV structures is summarised in Figure 4.9. The exchange field of the top spin valve decreases from the as-deposited value of 34 mT to a value of approximately 25 mT at all annealing fields. Similarly, the MR deteriorates from the as-deposited value of 7.4 % to 6.5 % independent of the annealing field. Thermal deterioration of the TSV structure occurs as discussed in the previous section and this dominates any possible magnetic field effects.

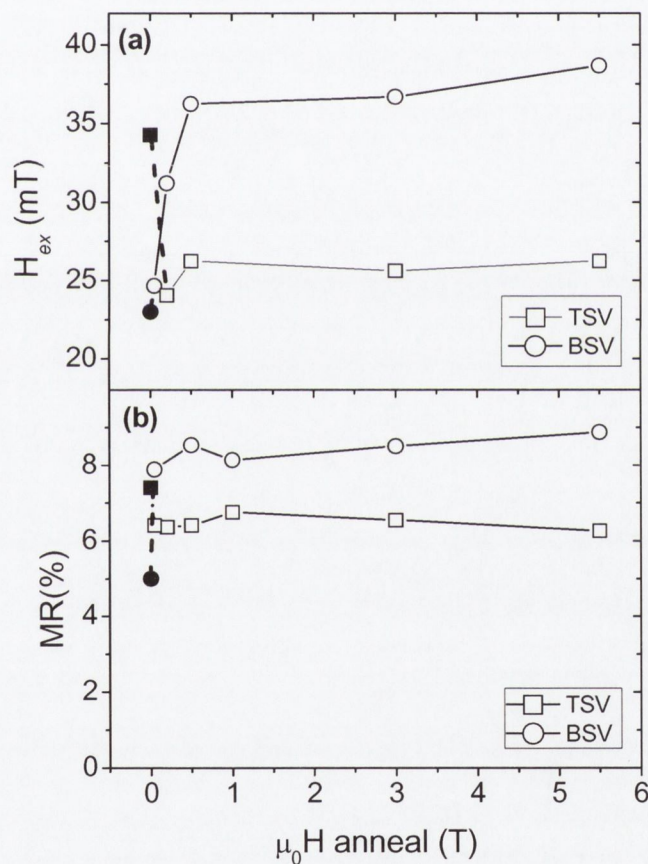


**Figure 4.9** Annealing field strength dependence of the exchange bias field (a) and MR (b) of the TSV and BSV structure. The annealing temperature was 210 °C. The filled symbols indicate the as-deposited values.



The exchange bias of the BSV structure clearly depends on the annealing field strength (Figure 4.9). The exchange bias field initially increases rapidly from 23 mT in the as-deposited state to 36 mT after annealing in a field of 0.5 T and this is followed by a more gradual increase to 39 mT for annealing in a field of 5.5 T. The influence of the annealing field strength can be understood by considering the microscopic origin of exchange bias in IrMn/ferromagnetic bilayers. The exchange bias effect in these systems depends on the uncompensated interfacial spin structure in the IrMn layer [22,23]. Spin reversal in the antiferromagnetic layer is thermally activated and therefore it depends critically on the experimental conditions (temperature and field sweep rate) and the energy barrier distribution. At room temperature and at low field sweep rates only some of the uncompensated spins are pinned, i.e., they do not rotate in an external magnetic field. The coupling between these spins and the spins in the ferromagnetic layer results in a shift in the hysteresis loop. The majority of the uncompensated interfacial spins, however, are not pinned. These spins are dragged along with the magnetisation reversal process in the ferromagnetic layer and although they do contribute to an enhanced coercivity they are not responsible for the exchange bias effect.

The pinned spins are most likely located at interface defects or grain boundaries, which act as pinning sites for domain walls in the IrMn layer. Consequently, the number of pinned interfacial spins depends critically on interface roughness and grain size [2,6-9]. In addition, dilution and irradiation experiments have shown that the number of defects in the antiferromagnetic layer also influences the domain structure and the exchange bias effect [24,25,26,27]. Since the magnitude of the exchange bias field is directly proportional to the pinned uncompensated moment along the bias direction, magnetic field annealing can change the bias field by modifying the number of pinned spins or realigning the orientation of the spin moment. Thermally-activated diffusion changes the number of defects in the



IrMn bulk and at CoFe/IrMn interface during annealing at elevated temperatures. This alters the number of pinned uncompensated interfacial spins and therefore the exchange bias field. The annealing field, on the other hand, does not change the number of pinned spins but it can influence the alignment of the spin moment.

It has generally been found that the magnetic state of the ferromagnetic layer during cooling determines the exchange bias [11,12]. However, this cannot explain the dependence of the exchange bias field on annealing field strength. If the ferromagnetic moment determines  $H_{ex}$ , saturation of this moment during field cooling would result in maximum exchange bias. Since the saturation field of the CoFe layer is considerably smaller than 0.05 T, annealing in this field would already maximize the exchange bias field. As can be seen in Figure 4.9, this is clearly not the case for the BSV structure. Obviously, the application of a larger magnetic field during cooling directly influences the alignment of the uncompensated interfacial spins in the IrMn layer. The component of the interfacial spin moment along the annealing field direction increases with increasing field strength and after freezing some of these interfacial spins during the field cooling procedure it results in an enhanced exchange bias field.

The strength of the annealing field does not have a large effect on the spin valves with the synthetic antiferromagnet (Figure 4.10). Thermal degradation of the SAFTSV dominates any effect and the MR and exchange bias are lower than their as-deposited values at all annealing temperatures and fields. For the SAFBSV, the MR increases from its as-deposited value of 6.4 % and reaches its highest value of 9 % after annealing in a 5.5 T field. The MR of the structures is higher than that of the SAFTSV structure at all annealing fields and temperatures. No clear field annealing effects are evident from the exchange bias of the SAFBSV. The strength of the exchange bias in these structures



depends mainly on the coupling between the two CoFe layers across the Ru spacer and not on the exchange coupling at the CoFe/IrMn interface as discussed in section 4.2. Changes in the spin structure of the IrMn layer do therefore not have a large affect on the exchange bias and hence no dependence of  $H_{ex}$  on the annealing field strength is measured (Figure 4.10).

The effect of the annealing field strength on tunnel junctions with a SAF structure has been reported by Liu et al [28]. When annealing the tunnel junctions at a field of 200 mT, the magnetisations of the SAF layer rotated perpendicular to the annealing field and a large spin flop occurred resulting in drastically reduced TMR signal. A similar result was observed by Jun et al [29] where a spin flop occurred at a field of 100 mT. This effect has not been observed here. The most likely explanation is that the number of field anneals performed up to 500 mT was not large enough to observe this effect.

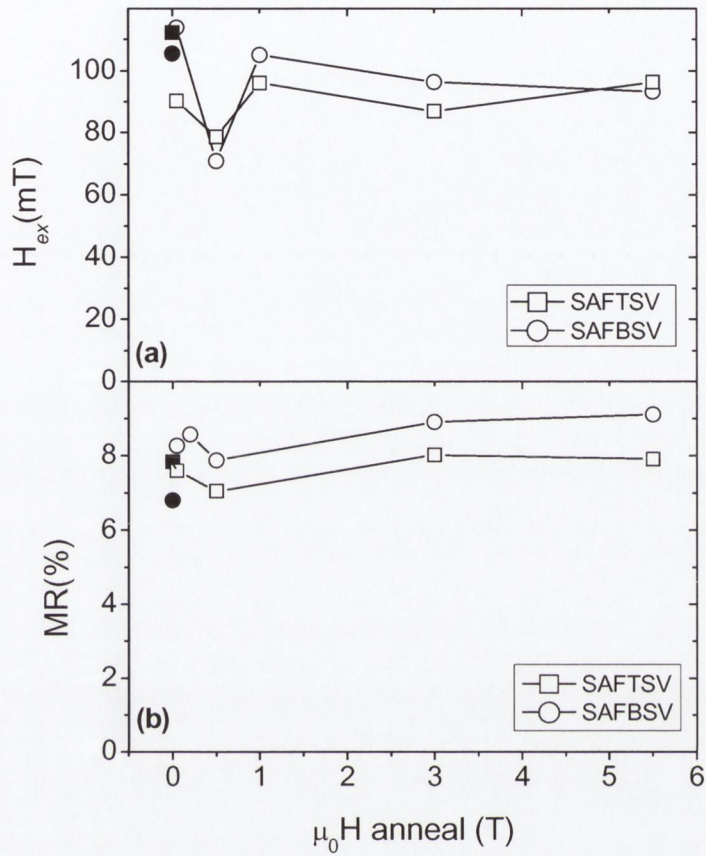


**Figure 4.10** Annealing field strength dependence of the exchange bias field (a) and MR (b) of the SAFTSV and SAFBSV structure. The annealing temperature was 210 °C. The filled symbols indicate the as-deposited values



## 4.5 Conclusion

We have shown that magnetic annealing in large fields enhances the exchange bias and MR of IrMn bottom-pinned spin valves. The dependence of the exchange bias field on annealing field strength can be split into two regimes: For annealing fields up to 0.5 T the exchange bias field increases rapidly from 23 mT to 36 mT. Above 0.5 T the enhancement is more gradual and the exchange bias field reaches 39 mT after annealing in a field of 5.5 T. The annealing field effects for the IrMn bottom-pinned spin valves are attributed to a realignment of the pinned interfacial spins in the IrMn layer. The application of a large magnetic field during cooling increases the component of the pinned interfacial moment along the field direction and this results in a larger exchange bias. For IrMn top-pinned spin valves and spin valves with a synthetic antiferromagnet no clear magnetic field effects were measured. For top-pinned spin valves the study on annealing field effects is complicated by a thermal deterioration of the magnetotransport properties during annealing and for spin valves with a synthetic antiferromagnet the pinning strength does not depend largely on the spin structure in the IrMn layer and is determined by the coupling across the thin Ru layer.

## 4.6 References

---

- [1] G. Anderson, Y. Huai, and L. Miloslawsky, *J. Appl. Phys.* **87** 6989 (2000).
- [2] M. Pakala, Y. Huai, G. Anderson, and L. Miloslawsky, *J. Appl. Phys.* **87**, 6653 (2000).
- [3] J. van Driel, F.R. de Boer, K.-M.H. Lenssen, and R. Coehoorn, *J. Appl. Phys.* **88**, 975 (2000).
- [4] H. Li, P.P. Freitas, Z. Wang, J.B. Sousa, P. Gogol and J. Chapman, *J. Appl. Phys.* **89**, 6904 (2001).
- [5] S-S. Lee, B-K. Kim, J-Y. Lee, D-G. Hwang, S-W. Kim, M-Y. Kim, J-Y. Hwang, and J-R. Rhee, *J. Appl. Phys.* **95**, 7525 (2004).
- [6] R. Nakatani, H. Hoshiya, K. Hoshino, and Y. Sugita, *J. Magn. Magn. Mater.* **173** 321 (1997).
- [7] J-C. Ro, Y-S. Choi, S-J. Suh, and H-J. Lee, *IEEE Trans. Mag.* **35**, 3925 (1999).
- [8] H.N. Fuke, K. Saito, M. Yoshikawa, H. Iwasaki, and M. Sahashi, *Appl. Phys. Lett.* **75**, 3680 (1999).
- [9] K. Yagami, M. Tsunoda, and M. Takahashi, *J. Appl. Phys.* **89**, 6609 (2001).
- [10] G. Malinowski, M. Hehn, S. Robert, O. Lenoble, A. Schuhl, and P. Panissod, *Phys. Rev. B* **68**, 184404 (2003).
- [11] P. Miltényi, M. Gierlings, M. Bamming, U. May, G. Güntherodt, J. Nogués, M. Gruyters, C. Leighton, and I.K. Schuller, *Appl. Phys. Lett.* **75**, 2304 (1999).
- [12] N.J. Gökemijer, J.W. Cai, and C.L. Chien, *Phys. Rev. B* **60**, 3033 (1999).
- [13] T. Ambrose and C.L. Chien, *J. Appl. Phys.* **83**, 7222 (1998).
- [14] R. Coehoorn, *Handbook of Magnetic Materials*, **15**, 1-197 (2003), Elsevier.
- [15] J. Sort, B. Rodmacq, S. Auffret, B. Dieny, *Appl. Phys. Lett.* **83**, 1800 (2003).
- [16] B. Dieny, M. Li, S.H. Liao, C. Horng, K. Lu, *J. Appl. Phys.* **87**, 3415 (2000).



- 
- [17] J.C.S. Kools, *IEEE Trans Magn* **32**, 3165 (1996).
- [18] Y.K. Kim, G-H. Park, S-R. Lee, S-H. Min, J.Y. Won, and S.A. Song, *J. Appl. Phys.* **93**, 7924 (2003).
- [19] S. Cardoso, P.P. Freitas, C. de Jesus, P. Wei, and J.C. Soares, *Appl. Phys. Lett.* **76**, 610 (2000).
- [20] J.H. Lee, S.J. Kim, C.S. Yoon, C.K. Kim, B.G. Park, and T.D. Lee, *J. Appl. Phys.* **92**, 6241 (2002)
- [21] G. Anderson, M. Pakala, Y. Huai, *IEEE Trans. Mag.* **36**, 2605 (2000).
- [22] T.P.A. Hase, B.D. Fulthorpe, S.B. Wilkins, B.K. Tanner, C.H. Marrows, and B.J. Hickey, *Appl. Phys. Lett.* **79**, 985 (2001).
- [23] H. Ohldag, A. Scholl, F. Nolting, E. Arenholz, S. Maat, A.T. Young, M. Carey, and J. Stöhr, *Phys. Rev. Lett.* **91**, 017203 (2003).
- [24] P. Miltényi, M. Gierlings, J. Keller, B. Beschoten, G. Güntherodt, U. Nowak, and K.D. Usadel, *Phys. Rev. Lett.* **84**, 4224 (2000).
- [25] A. Mougin, T. Mewes, M. Jung, D. Engel, A. Ehresmann, H. Schmoranzer, J. Fassbender, and B. Hillebrands, *Phys. Rev. B* **63**, 060409 (2001).
- [26] A. Misra, U. Nowak, and K.D. Usadel, *J. Appl. Phys.* **93**, 6593 (2003).
- [27] E. Kerr, S. van Dijken, R.M. Langford and J.M.D. Coey, *J. Magn. Magn. Mater.* **290-291**, 124 (2005).
- [28] Y.W. Liu, Z. Zhang, Z. Zhang, P.P. Freitas, J.L. Martins, *J. Appl. Phys.* **91**, 8296 (2002).
- [29] K.I. Jung, J.H. Lee, K.H. Shin, K. Rhee, B.C. Lee, *IEEE Trans Magn.* **40**, 2299 (2004).

## Chapter 5

# Effects of Ga<sup>+</sup> ion implantation on the magnetoresistive properties of spin valves with IrMn

### 5.1 Introduction

The drive to study nanoscale magnetic elements has resulted in increased use of focused ion beam milling of magnetic thin films and multilayers. The implantation of Ga<sup>+</sup> ions during milling can have adverse effects on the magnetic and electrical properties of these systems. A wide variety of phenomena have been reported when magnetic thin films and multilayers are subjected to ion irradiation. In NiFe films the coercivity and local anisotropy direction have been altered upon Ga<sup>+</sup> ion irradiation [1]. The magnetisation direction in Co/Pt multilayers has been altered in a controlled manner, switching from out-of-plane to in-plane upon irradiation [2]. Exchange bias systems have also been studied in detail. The exchange coupling in bilayers of Ni<sub>81</sub>Fe<sub>19</sub>/Fe<sub>50</sub>Mn<sub>50</sub> was altered through irradiation with 5 keV He<sup>+</sup> ions [3,4]. It was demonstrated that the exchange bias field can be changed both in magnitude and direction. In particular, within a dose range of  $1 \times 10^{15}$  -



$8 \times 10^{15}$  ions/cm<sup>2</sup>, an enhancement of the local exchange bias field was observed. At higher ion doses it was found that the exchange bias was reduced below its initial value. A model for the effect was established whereby the enhancement of the exchange bias field was attributed to the creation of defects within the volume of the AFM layer and the degradation at higher doses attributed to intermixing at the FM/AFM interface. In order to determine if this exchange bias enhancement was a material-specific or ion-specific effect, implantation of the Ni<sub>81</sub>Fe<sub>19</sub>/Fe<sub>50</sub>Mn<sub>50</sub> system with 30 keV Ga<sup>+</sup> ions was subsequently investigated [5]. In this case, no enhancement of the exchange bias field was observed. The authors highlighted the heavier mass and hence different implantation profile of Ga<sup>+</sup> as opposed to He<sup>+</sup> ions as the reason for the higher degree of interfacial mixing in their experiment. The effect of 30 keV Ga<sup>+</sup> ion implantation on Co<sub>90</sub>Fe<sub>10</sub>/Ir<sub>20</sub>Mn<sub>80</sub> bilayers has also been investigated [6]. The authors report no detectable change in structure as investigated by TEM up to a dose of  $1 \times 10^{14}$  ions/cm<sup>2</sup> although the exchange bias field is already reduced by 30 % at this dose. The structural quality of the bilayer decreased with increasing dose becoming totally amorphous at a dose of  $5 \times 10^{15}$  ions/cm<sup>2</sup>. The exchange bias field and coercivity decreased with increasing dose, no exchange bias enhancement was observed. The magnetic moment of the CoFe layer was found to decrease approximately linearly with increasing dose, already reduced by 50 % at a dose of  $1 \times 10^{15}$  ions/cm<sup>2</sup>. The authors cite increased mixing of atoms from the various layers as the cause of the magnetic degradation of the sample.

The effects of ion implantation on a number of spin valve systems have been investigated. NiMn spin valves implanted with 8 MeV Ni<sup>+</sup> ions showed a degradation of MR with increasing dose [7]. FeMn spin valves implanted with 10 keV He<sup>+</sup> ions showed an exponential decrease in MR with increasing ion dose caused by a higher sheet resistance due to increased defect density and increased coupling between the free and pinned layers

[8]. IrMn spin valves implanted with Ga<sup>+</sup> ions showed an improvement in surface roughness after ion irradiation. The MR and exchange bias were found to decrease with increasing ion dose whereas the zero field resistance increased with increasing ion dose [9]. All these experiments deal with the implantation of ions from the top, i.e. perpendicular to the film plane. The influence of Ga<sup>+</sup> ion implantation during FIB milling, on the other hand, has been studied in less detail. It is this configuration that is of particular interest for applications where FIB milling is used to make sub-micron size magnetic elements. In this chapter, the effect of 30 keV Ga<sup>+</sup> ion implantation in IrMn exchange biased spin valves is investigated. Ga<sup>+</sup> ions were implanted directly, perpendicular to the film plane at doses ranging from 10<sup>12</sup> to 10<sup>16</sup> ions/cm<sup>2</sup>. In addition, Ga<sup>+</sup> ion implantation effects were studied by FIB milling 10 μm spin valve lines fabricated by UV lithography to line widths ranging from 7 μm to 0.5 μm. In these two experiments, the properties of the spin valves were found to degrade with increasing ion dose and decreasing line width, respectively.

## 5.2 Direct implantation of Ga<sup>+</sup> ions

Spin valves with structure Ta(5nm) /NiFe(3.5nm) /CoFe(1.5nm) /Cu(2.9nm) /CoFe(2.5nm)/IrMn(10nm)/Ta(5nm) were grown by DC magnetron sputtering onto thermally oxidized silicon substrates in a Shamrock deposition tool. A metal shadow mask was used to define structures with a line width of 300 μm for four point magnetoresistive measurements. The films were deposited at room temperature in a magnetic field of 5 mT. As-deposited spin valves exhibit a GMR effect of 7.4% and an exchange bias field ( $H_{ex}$ ) of 34 mT as shown in the magnetotransport and SQUID magnetisation curves of Figure 5.1. The resistance of the as-deposited film is 98 Ω.



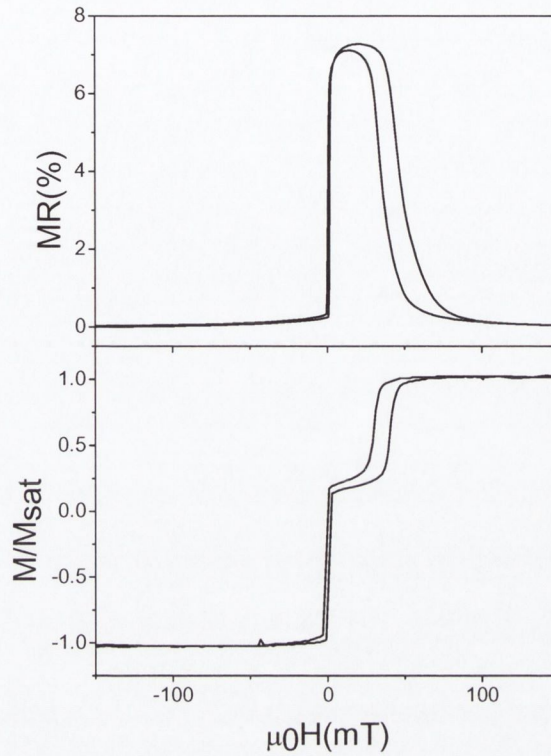


**Figure 5.1 Magnetoresistance and magnetisation curves for the as-deposited spin valve structure.**

These spin valves were subsequently implanted with 30 keV Ga<sup>+</sup> ions in an FEI strata DB 235 tool at doses ranging from 10<sup>12</sup> to 10<sup>16</sup> ions/cm<sup>2</sup>. The dose,  $D$ , was calculated from:

$$D = \frac{it}{eA} \quad (5.1)$$

where  $i$  is the ion current,  $t$  the exposure time,  $A$  the area of implantation and  $e = 1.602 \times 10^{-19}$  Coulombs. The ion beam was perpendicular to the film plane during implantation. The dual beam FIB allowed the use of the electron beam for alignment and imaging of the sample, hence avoiding additional ion implantation by use of the ion beam.

Magnetoresistance curves for a selection of doses are shown in Figure 5.2. A dramatic decrease in the magnetoresistive properties is observed with increasing ion dose, similar to that measured by Guo et al [9].

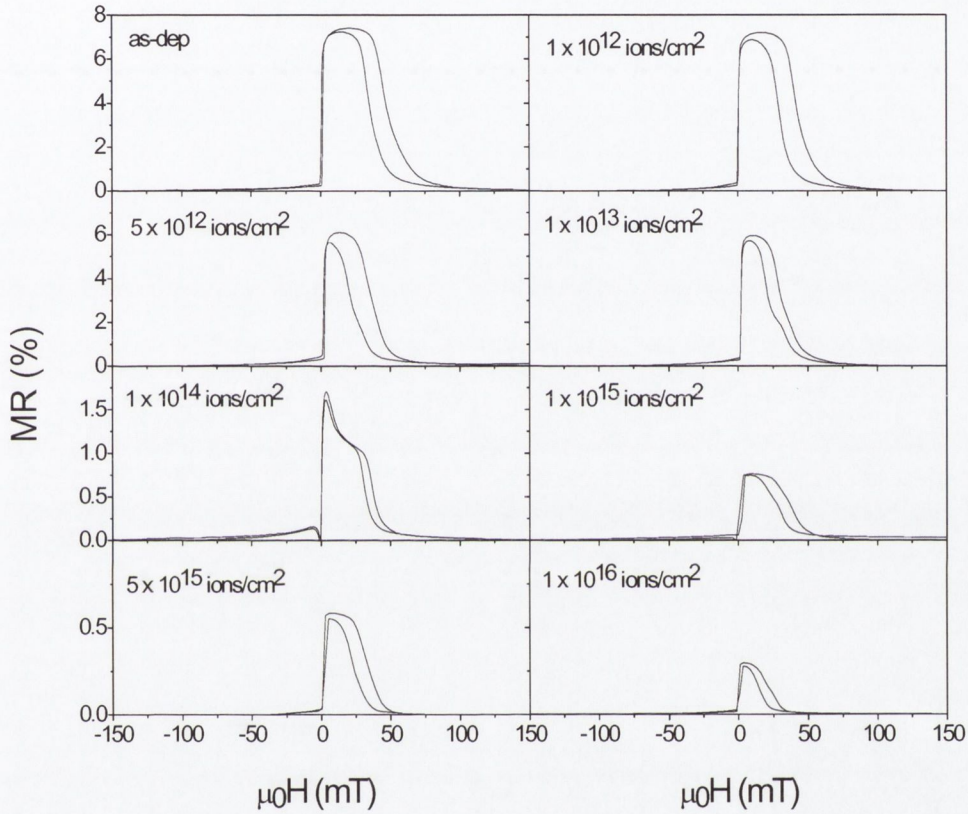


**Figure 5.2** Magnetoresistance of implanted spin valves

The variation of the GMR and film resistance at saturation as a function of ion dose is summarized in Figure 5.3 and the dependence of the exchange bias field on ion dose is shown in Figure 5.4. A dose of  $10^{14}$  ions/cm<sup>2</sup> reduces  $H_{ex}$  to about 75% of its initial value. At low doses the resistance does not increase much and the small reduction of GMR is partly due to the degradation of exchange bias: a full antiparallel alignment of the magnetic moments in the spin valve is not obtained for reduced  $H_{ex}$ .



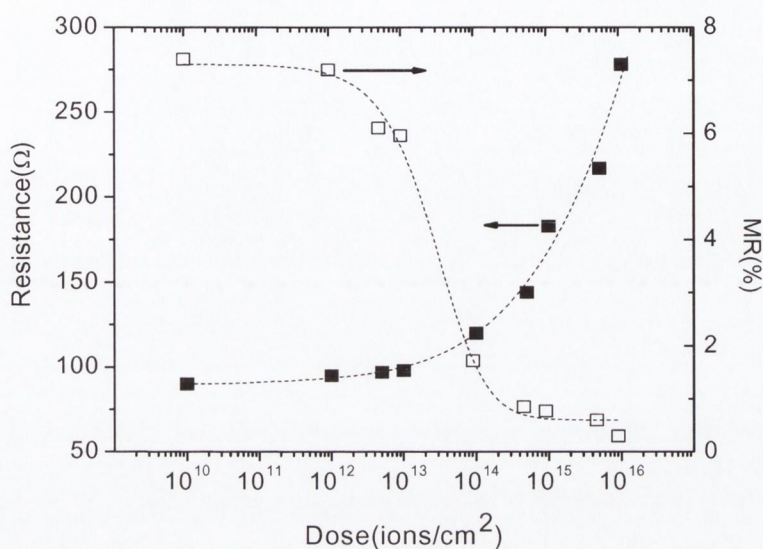


**Figure 5.3** spin valve resistance (filled symbols) and magnetoresistance (open symbols) as a function of ion dose (lines are guides to the eye).

At higher doses the resistance increases rapidly suggesting the generation of bulk defects within the spin valve. TRIM simulations of the  $\text{Ga}^+$  ion implantation process confirm this. The simulation in Figure 5.5 indicates that 30keV  $\text{Ga}^+$  ions are implanted in the entire spin valve stack with the implantation and vacancy distributions having a broad maximum within the IrMn layer. The implantation of  $\text{Ga}^+$  ions creates defects that reduce the exchange bias field by either a destruction of the antiferromagnetic order in the IrMn layer or a reduction of the exchange coupling at the CoFe/IrMn interface.

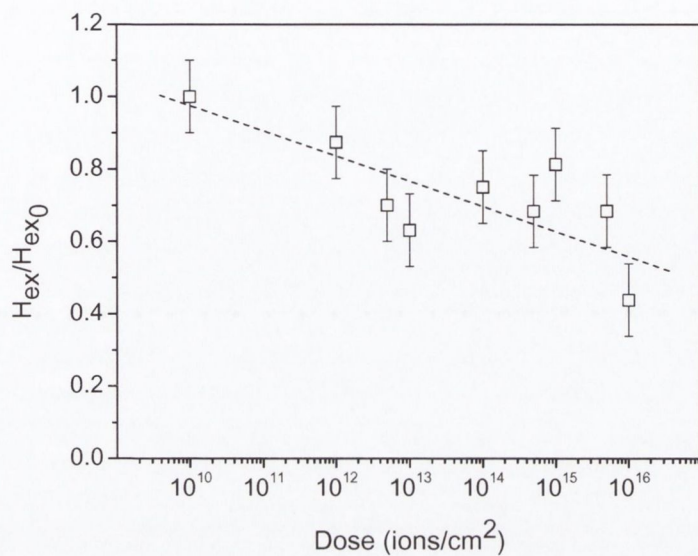


Figure 5.4 Normalised exchange bias field as a function of ion dose

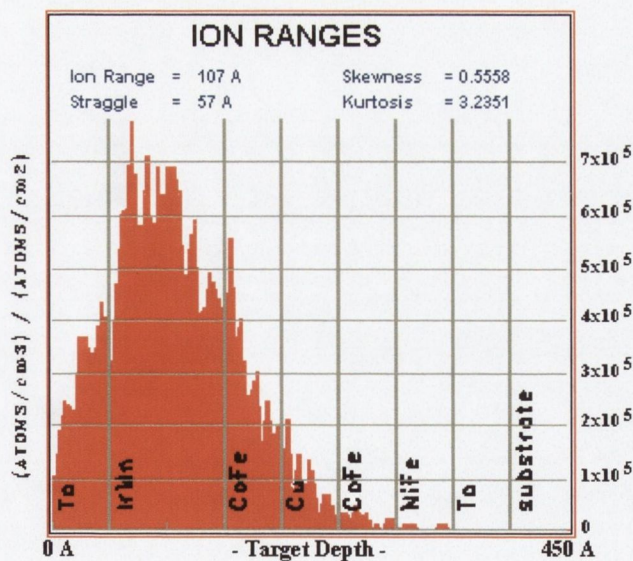


Figure 5.5 TRIM simulation showing 30 keV Ga<sup>+</sup> ion distribution throughout the spin valve structure.



In the study of  $\text{He}^+$  ion implantation in FeMn layers discussed in the introduction, it was found that an initial increase of the exchange bias at low doses is followed by a decrease of  $H_{ex}$  at high doses [3,4]. While the initial enhancement of  $H_{ex}$  was attributed to modifications to the bulk antiferromagnetic order, the degradation of the exchange bias was explained by intermixing at the F/AFM interface. Since we do not see any enhancement of the exchange bias field in our experiments this would suggest that the reduction of  $H_{ex}$  is mainly due to  $\text{Ga}^+$  ion implantation at the CoFe/IrMn interface. However, we note that  $\text{Ga}^+$  ion implantation is a much more energetic process than the implantation of  $\text{He}^+$  ions and therefore we expect that both the antiferromagnetic order in the IrMn layer as well as the structure of the CoFe/IrMn interface is seriously damaged at high doses. This is in agreement with the work on CoFe/IrMn bilayers [6] where a continuous reduction of exchange bias with dose was observed and the exchange bias had already been lowered to 70 % at doses as low as  $10^{14}$  ions/cm<sup>2</sup>.

The degraded exchange bias can explain in part the reduction in GMR of the spin valves. We note from Figure 5.3 that the value of the stack resistance,  $R$ , increases with increasing dose probably due to the creation of defects as a result of the implantation. As the GMR ratio is given by  $GMR(\%) = \Delta R / R$  an increase in stack resistance will automatically give a decrease in MR ratio for the same value of  $\Delta R$ . The size of  $\Delta R$  is a closer indication of the GMR effect within the spin valve. From Figure 5.6 we can see that  $\Delta R$  also decreases with increasing ion dose, in a similar manner to the MR change. This indicates that the change in MR is not just due to an increase of the resistance due to the structural degradation of the spin valve. This is supported by Figure 5.5 where we can see that the implantation and vacancy profile extends throughout the entire spin valve stack and indicates a deterioration of the CoFe/Cu interfaces. Spin-dependent scattering at the CoFe/Cu interfaces is the main source of GMR in these spin valves and the reduction of

$\Delta R$  with dose indicates a decrease in spin dependent scattering, contributing to the drastic reduction of GMR at high doses.

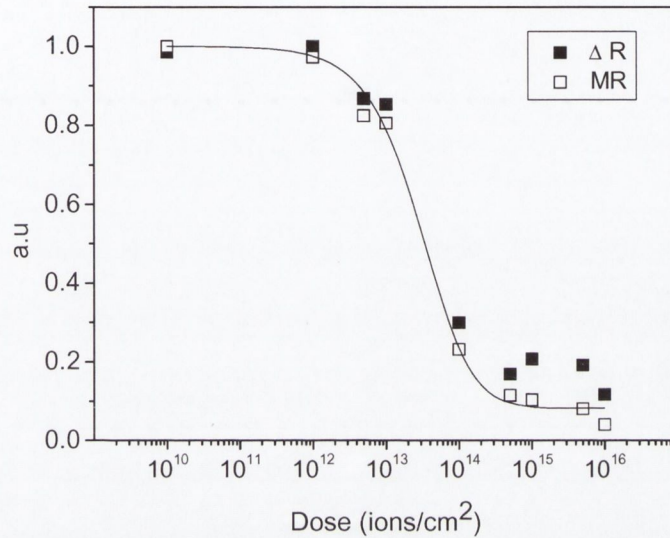


**Figure 5.6** Normalised MR and  $\Delta R$  as a function of ion dose (line is a guide).

Recently the effect of  $\text{Si}^+$  ion implantation on Co/Cu multilayers has been reported [10]. The authors report a monotonic decrease of GMR with ion dose which they attribute to intermixing of the layers. They also found that thermal annealing after implantation can restore the GMR to almost its pre-irradiation value due to a backdiffusion process in metastably intermixed regions. The effect of thermal annealing on our  $\text{Ga}^+$  ion implanted spin valves with properties similar to those shown in Fig. 2 has been investigated. The irradiated spin valves were magnetically annealed for one hour at a temperature of 210°C and fields of 0.8 T and 5.5 T. No improvement of the GMR and exchange bias was observed in our case.



### 5.3 Ga<sup>+</sup> ion implantation during FIB milling

The effect of Ga<sup>+</sup> ion implantation during FIB milling was also investigated. A test sample was devised consisting of a spin valve line of width  $w = 10 \mu\text{m}$  with transverse Cu contacts defining 5 segments of  $10 \times 4 \mu\text{m}$ . This structure was made by UV lithography as described in Chapter 2. The structure was subsequently milled with 30 keV Ga<sup>+</sup> ions at currents between 10 and 100 pA to give line widths ranging from  $7 \mu\text{m}$  to  $0.5 \mu\text{m}$  as shown in Figure 5.7.

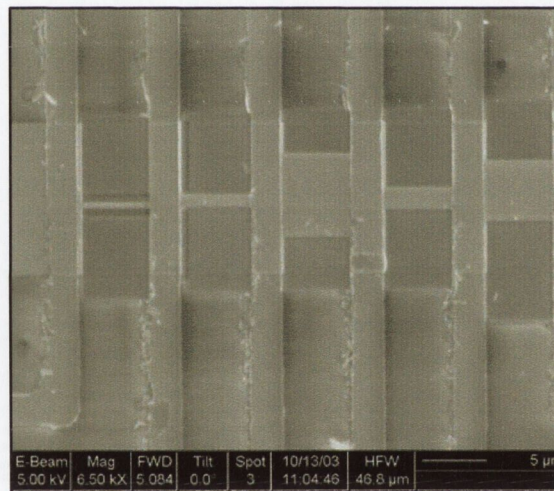


**Figure 5.7** SEM of spin valve lines FIB milled to different widths.

The measured magnetoresistance curves on these spin valves are shown in Figure 5.8. The  $10 \mu\text{m}$  line, which was not milled with the FIB, exhibits a similar GMR as the as-deposited spin valve of Figure 5.1 and its resistance is  $10 \Omega$ . As the line width is reduced by FIB milling, the GMR and exchange bias field decrease until at  $w = 500 \text{ nm}$  they are only 0.5% and 23 mT, respectively. Milling the spin valve from  $10 \mu\text{m}$  to  $7 \mu\text{m}$  already reduces the GMR and the exchange bias field to 65% and 50% of their original value.

This reduction might be due to  $\text{Ga}^+$  ion implantation and diffusion from the sides of the spin valve. However, in a recent paper on lateral  $\text{Ga}^+$  implantation in the sidewalls of FIB trimmed CoFeNi recording heads the lateral  $\text{Ga}^+$  penetration length was estimated to be 10 nm only [11]. A more likely explanation for the rapid degradation of the spin valve properties is that  $\text{Ga}^+$  ions are implanted from the top during FIB milling of micron size structures. The ion beam profile is Gaussian with exponential tails and as a result  $\text{Ga}^+$  ions are implanted at relatively large distances from the milling edge. At 1  $\mu\text{m}$ , e.g., the dose is expected to be two to three orders of magnitude lower than the focal point intensity [12]. Assuming that a dose of at least  $10^{17}$  ions/cm<sup>2</sup> is required to mill the spin valve stack, the area 1  $\mu\text{m}$  away from the milling edge will be irradiated with a dose of about  $10^{15}$  ions/cm<sup>2</sup>. The implantation of this amount of  $\text{Ga}^+$  ions already results in a considerable reduction of the GMR and the exchange bias field (Figure 5.3, Figure 5.4) and is therefore likely to contribute to the degradation of the properties of the spin valve lines.

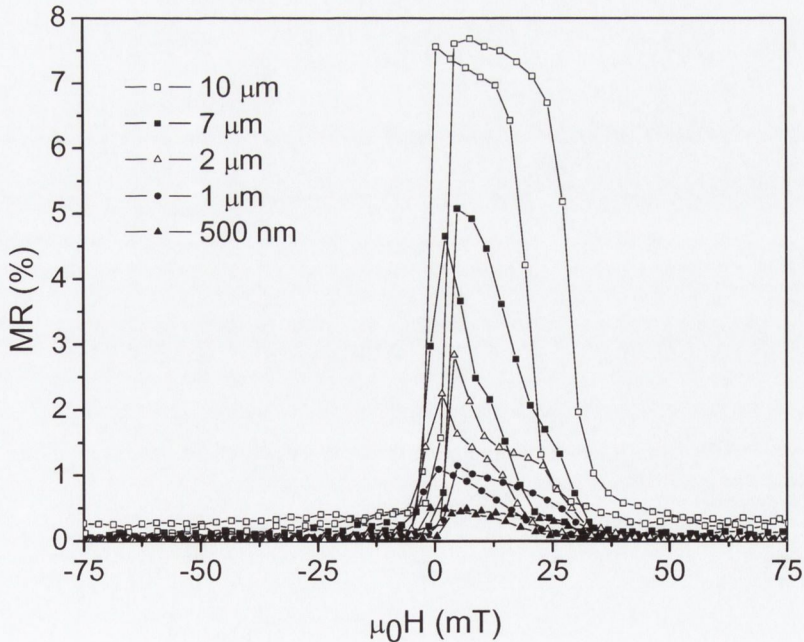


**Figure 5.8 Magnetoresistance of FIB milled spin valves with line widths ranging from 10  $\mu\text{m}$  to 0.5  $\mu\text{m}$ .**



The resistance of the milled spin valve lines increases linearly with decreasing line width (Figure 5.9a) but increases much more rapidly than expected for the line dimensions.  $\Delta R$  increases linearly with decreasing line width but levels off at the smallest line widths (Figure 5.9b). This suggests that the magnetic properties of the lines have been degraded as a result of implantation. The combination of reduced  $\Delta R$  and increased  $R$  results in a drastic reduction of the MR at smaller line widths (Figure 5.9c). This large increase of the resistance due to  $\text{Ga}^+$  implantation, increased edge roughness and/or local heating effects during milling is the predominant cause of the reduction of MR in the milled spin valve lines.

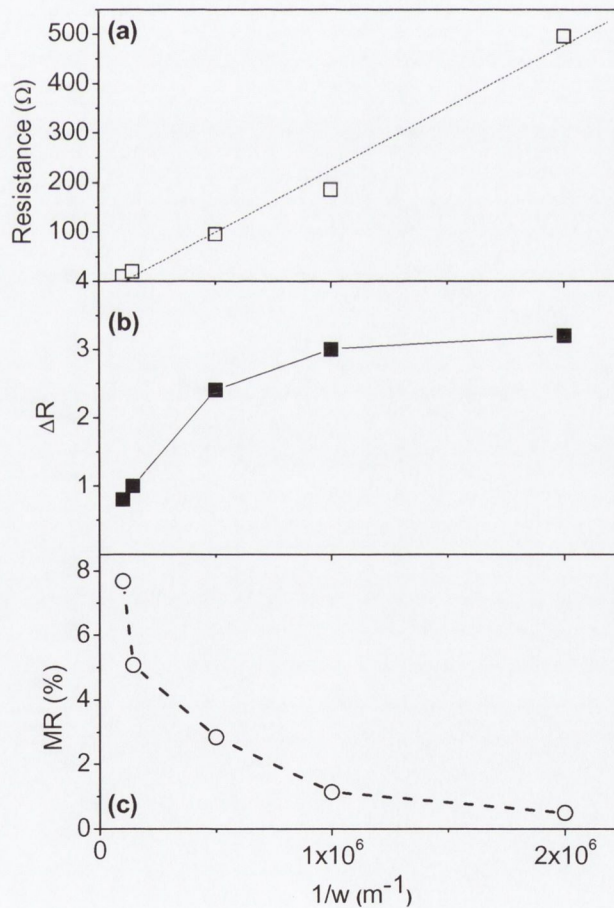


**Figure 5.9** (a) Resistance (b)  $\Delta R$  and (c) magnetoresistance as a function of  $1/\text{linewidth}$  for FIB milled spin valves

The effects of nanopatterning on pseudo spin valves and IrMn exchange biased spin valves have recently been investigated [13,14]. In this work, a hard mask of SiO<sub>2</sub>(50nm)/Au(20nm) was deposited on top of the spin valve. A nanowire array was then FIB milled into the hard mask and the structure milled through using Ar<sup>+</sup> ion milling. In this way, the spin valve is protected from Ga<sup>+</sup> implantation. The authors reported an increase in MR with decreasing line width which they attributed to a higher degree of antiparallel alignment as evidenced by higher  $\Delta R$  values. At smaller line-widths however (250nm) the MR was lower due to increased resistance. The increase in resistance was attributed to increased edge roughness and small amounts of Ga<sup>+</sup> implantation. The use of a hard mask such as SiO<sub>2</sub>, therefore seems a more appropriate manner of using FIB milling to create magnetic nanostructures.

#### 5.4 Conclusion

The effects 30 keV Ga<sup>+</sup> implantation on top-pinned IrMn spin valves have been investigated. Direct implantation of Ga<sup>+</sup> ions at doses less than 10<sup>14</sup> ions/cm<sup>2</sup> results in a gradual decrease of GMR which is partly due to a deterioration of the exchange bias. Implantation at higher doses causes a large increase in the film resistance and a substantial deterioration of GMR. At this point the magnetic properties of the system have been seriously and irreversibly degraded by the creation of defects in the entire spin valve stack. The suitability of FIB milling for the fabrication of small magnetic elements was studied by reducing the width of 10  $\mu\text{m}$  spin valve lines. Here the GMR and the exchange bias field decreased rapidly with decreasing line width. The degrading effects are stronger than expected from 30 keV Ga<sup>+</sup> ion implantation from the sides and suggests that the spin valves are simultaneously implanted from the top. From these results we conclude that direct FIB milling without an appropriate mask should not be used for the fabrication of micron and sub-micron size spin valves.



## 5.5 References

---

- [1] D. Ozkaya, R.M. Langford, W.L. Chan, A.K Petford-Long, J. Appl. Phys. **91**, 9937 (2002).
- [2] C. Chappert, H. Bernas, J. Ferre, V. Kottler, J.P. Jamet, Y. Chen, E. Cambril, T. Devolder, F. Rousseaux, V. Mathet, H. Launois, Science **280**, 1919 (1998).
- [3] A. Mougin, T. Mewes, M. Jung, D. Engel, A. Ehresmann, M. Schmoranzer, J. Fassbender, B. Hillebrands, Phys. Rev. B **63**, 060409 (2001).
- [4] S. Poppe, J. Fassbender, B. Hillebrands, Europhys. Lett. **66**, 430 (2004).
- [5] S. Blomeier, D. McGrouther, R. O'Neill, S. McVitie, J.N. Chapman, M.C. Weber, B. Hillebrands, J. Fassbender, J. Magn. Magn. Mater. **290**, 731 (2005).
- [6] D. McGrouther, J.N. Chapman, F.W.M. Vanhelmont, J. Appl. Phys. **95**, 7772 (2004).
- [7] J.G. Lin, M.R. Wu, D.H. Ngu, C.Y. Huang, S. Mao, J. Magn. Magn. Mater. **209**, 128 (2000).
- [8] D. Engel, I. Krug, H. Schmoranzer, A. Ehresmann, A. Paetzold, K. Röhl, B. Ocker, W. Maass, J. Appl. Phys. **94**, 5925 (2003).
- [9] Z.B. Guo, D. you, J.J. Qiu, K.B. Li, Y.H Wu, Solid State Comm. **120**, 459 (2001).
- [10] M. Cai, T. Veres, F. Schiettekatte, S. Roorda, R.W. Cochrane, J. Appl Phys. **95**, 2006 (2004).
- [11] C.M. Park, J.A. Bain, T.W. Clinton, P.A.A. van der Heijden, Appl. Phys Lett. **84**, 3331 (2004)
- [12] B. Schmidt, L. Bischoff, J. Teichert, Sens. Act. A. **61**, 369 (1997).
- [13] D. Morecroft, B.B. Van Aken, J.L. Prieto, D.J. Kang, G. Burnell, M. G. Blamire, J. Appl. Phys. **97**, 054302 (2005).
- [14] D. Morecroft, J.L. Prieto, G. Blamire, J. Appl. Phys. **97**, 10C518 (2005).

## **Chapter 6**

# **Femtotesla Magnetic field Measurement with a Spin Valve Sensor**

### 6.1 Introduction

The measurement of very small magnetic fields is important for applications in the field of biomagnetism. The technique of magnetoencephalography (MEG) [1], [2] detects magnetic fields of the order of a few femtoteslas ( $10^{-15}$  Tesla) at low frequency ( $< 50$  Hz) created by neural activity in the brain. MEG is a non-invasive technique and commercial systems are used in hospitals for the study of brain activity in patients with conditions such as epilepsy and also for pre-surgical brain mapping. The sensors used in a MEG system are currently low-temperature dc Superconducting Quantum Interference Devices (SQUIDs). The basic element of a SQUID is a Josephson junction [3]. This consists of two superconductors separated by a thin insulating barrier. If the barrier is thin enough, pairs of superconducting electrons can tunnel through the barrier and the current depends on the phase coherence of the electron wavefunctions. A dc SQUID consists of two such junctions connected in parallel, forming a superconducting loop. Magnetic flux through



the superconducting loop is quantized and results in interference of the phases across the junctions. In the presence of magnetic flux with a constant current applied through the junction, interference of the phase modulates the critical current of the junctions and therefore the voltage across the device. Hence, the SQUID behaves as a flux-to-voltage converter, with a non-linear, periodic response to an externally applied flux. A flux transformer is integrated into the SQUID design in order to transport flux to the active region [4]. Commercial MEG systems consist of arrays of SQUIDs (more than 100) placed at different positions around the head in order to map the response of the brain. The sensors are arranged inside a cryostat operated at low temperature. Sophisticated electronics are required to linearise the output of the SQUIDs and compile the signals from all of the sensors. In order to reduce noise, the cryostat and the room in which the system is housed are magnetically shielded using high permeability materials. The best sensitivity achieved with low- $T_c$  SQUIDs based on Nb is  $1\text{fT}/\sqrt{\text{Hz}}$  at 4.2 K [5] and about  $30\text{fT}/\sqrt{\text{Hz}}$  with high- $T_c$  SQUIDs made with YBCO at 77 K [6], [7], [8].

In this chapter a possible alternative to SQUID sensors for the detection of very small magnetic fields is presented. This mixed sensor consists of an efficient flux-to-field transformer and a sensitive magnetoresistive sensor. The flux to field transformer is a superconducting loop containing a micron-size constriction. The magnetoresistive sensor is a low-noise spin valve placed above or below the constriction in the superconducting loop. The spin valve detects the applied field amplified by a factor up to a few thousands, depending on the size and geometry of the device. The sensor can be operated up to 77 K and a small size prototype with the capability of measuring 32 fT has been demonstrated [9]. For applications such as MEG, the mixed sensor has the possibility of reaching the sensitivity of a SQUID. Although it still needs to be operated at cryogenic temperatures some advantages over SQUIDs are evident. The fabrication of Josephson junctions with



reproducible properties is difficult in the case of high- $T_c$  superconducting films such as YBCO. The processing of the mixed sensor is easier, based on conventional inexpensive lithographic techniques. Future improvements to the mixed sensor sensitivity at 77 K should therefore make it highly competitive with high  $T_c$  SQUIDs. Furthermore, the output of the mixed sensor is a voltage, linear with field, whereas the SQUID outputs a non-linear response requiring further electronic processing. The possible applications of the sensor extend beyond MEG and biomagnetism to areas such as magnetometry and the investigation of fundamental physical phenomena such as vortex motion in superconductors and magnetic interactions. A technique based on atomic resonance has also been proposed for subfemtotesla resolution [10]. However, for application in MEG, that apparatus may be too large to build a full array of sensors. A sensor device consisting of a superconducting loop and a Hall-sensor has also been reported [11], [12]. This device uses two superconducting YBCO loops to amplify the magnetic field acting on a bismuth Hall sensor. This device demonstrates resolution of  $1 \text{ nT}/\sqrt{\text{Hz}}$ , considerably less than the mixed sensor. The sensitivity of the device depends on the amplification of the superconducting loop and sensitivity of the Hall sensor which depends on the Hall coefficient of the material. As bismuth has one of the highest Hall coefficients of the pure elements, only limited improvements in sensitivity of this device can be envisaged.

The device concept for the mixed sensor was due to C. Fermon and M. Pannetier at CEA Saclay, Paris. My contribution to the work was the deposition and optimisation of the spin valve element of the YBCO/spin valve mixed sensor. The spin valve stacks were deposited on top of  $\text{Si}_3\text{N}_4$  covered YBCO films. This was done at T.C.D. using the Shamrock deposition tool. Patterning and measurement of the prototype device presented in this chapter were carried out by the Saclay team.



## 6.2 Design of the spin valve element of the mixed sensor

Spin valves have high magnetic field sensitivity which makes them attractive for use as sensors. Their behaviour in magnetic fields however, can limit their uses for very accurate measurements. One limitation is hysteresis of the free layer. Very low hysteresis is necessary if the output of the sensor is to be reproducible and not affected by random magnetic fields. Another limitation is the sensor linearity in the working region. In the case of the mixed sensor, this is less of a problem as the field range sensed is so small that the spin valve response is far from saturation and is linear. The main problem for the mixed sensor is the minimisation of the noise and in particular the magnetic noise since it impairs the sensitivity of the device.

### 6.2.1 Noise in spin valves

In spin valve stacks at low frequencies two sources of noise dominate, thermal noise and  $1/f$  noise. The thermal noise is due to spontaneous fluctuations induced by the thermal excitations and it is related to the resistance,  $R$ , by the Nyquist formula. Its voltage power spectral density is given by:

$$S_v(f) = 4k_B TR \quad (6.1)$$

where  $k_B$  is the Boltzmann constant. This noise has no magnetic origin and cannot be suppressed or modified but it is independent of the sensitivity of the sensor and depends only on its resistance.

In addition to the thermal noise, a  $1/f$  frequency dependent noise appears in all systems, both magnetic and non-magnetic. A general formula given by Hooge in 1969 describes its power spectral density:

$$S_v(f) = \frac{\gamma_H V^2}{N_C f} \quad (6.2)$$

The parameter  $\gamma_H$  is called the Hooge constant and is used as a comparison reference for 1/f noise. Its value is about  $10^{-2}$  to  $10^{-3}$  for good metallic systems but can be much higher when there are magnetic domains present.  $N_c$  is the number of charge carriers in the sample and for good metals can be approximated to the number of atoms. The 1/f noise is then inversely proportional to the volume of the sample and therefore becomes dominant in small structures.

### 6.2.2 Spin valve design

Appropriate design of both the spin valve stack and the physical shape and dimensions of the patterned device is vital for sensor performance. The spin valve stack is optimised for high MR and well-defined switching of the free layer with low coercivity and low offset. The deposition of the free and pinned layers with crossed anisotropies plays an important role as this ensures coherent rotation of the free layer and low hysteresis. Linearity of the response can be improved by incorporating a bias line into the patterned structure [13]. The presence of magnetic domains in the active region of spin valves is the main source of magnetic low-frequency noise. Appropriate design of the patterned sensor can suppress this. Two such optimised designs are the yoke shape and the short-circuited meander shown in Figure 6.1. Spin valves can be patterned using conventional UV lithography with the free layer aligned along the long arm of the yoke or meander and the pinned layer aligned perpendicular to the free layer. A second lift-off lithography step is used to pattern contacts. The meander is short-circuited at the corners to reduce magnetic noise due to domain formation during reversal. This configuration has higher resistance which can be advantageous for certain applications.

The yoke structure was chosen for the mixed sensor device as the entire active region could be placed directly above or below the constriction of the superconducting loop. The



shape anisotropy of the yoke structure means that the free layer magnetisation is aligned along the arm of the device and coherent switching of the free layer results in a free layer response with low hysteresis. The magnetotransport curve of patterned spin valve yoke of length  $60\ \mu\text{m}$  and width  $6\ \mu\text{m}$  is shown in Figure 6.2.

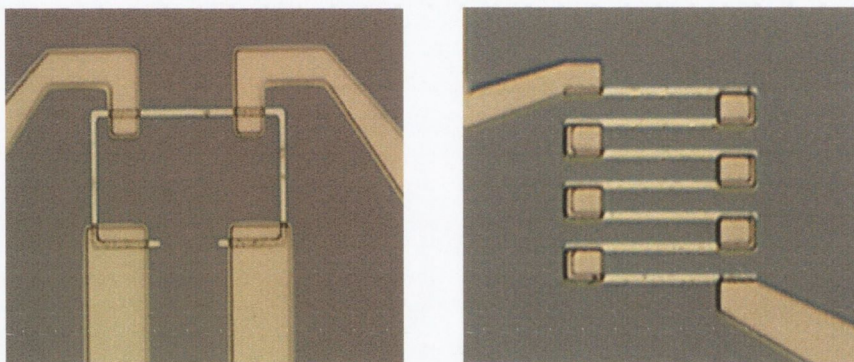


**Figure 6.1** Spin valves patterned into a yoke device (left) and a short-circuited meander (right).

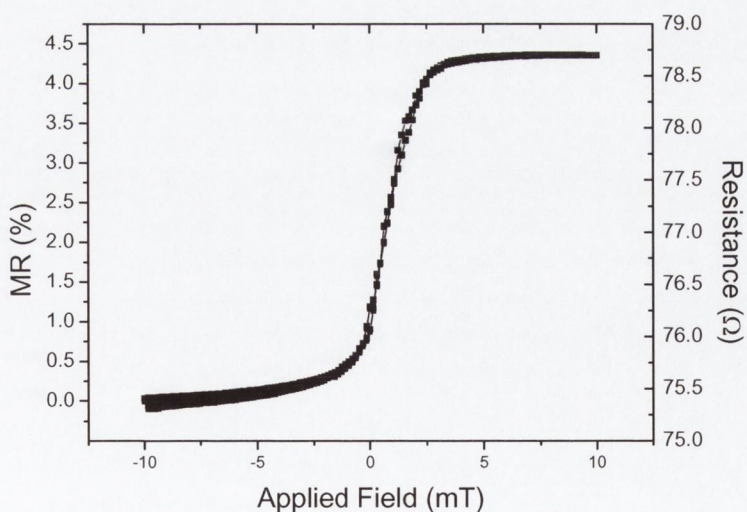


**Figure 6.2** Resistance and MR ratio of the free layer reversal of a spin valve yoke

Figure 6.3 shows a simulation [14] of the free layer of a yoke shaped spin valve at zero field after reversal from saturation. A vortex-like feature is evident in the left arm of the yoke but the important feature is that in the active region of the device, between the voltage contacts, the magnetisation is pointing in the same direction and there are no domains.

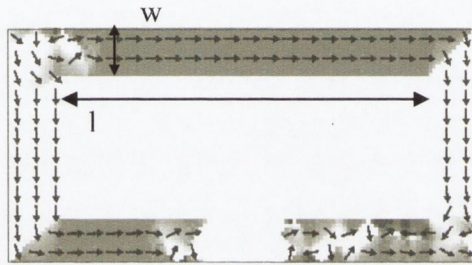


**Figure 6.3** Magnetic configuration of a yoke after saturation and reversal to zero magnetic field as obtained from micromagnetic simulations.

This is very important from the point of view of  $1/f$  noise which is very sensitive to the presence of domains. In order to confirm this, noise measurements were taken at three different points of the sensor response in Figure 6.2, saturation at 10 mT, and in the sensitive regions at 2 mT and 1 mT. Figure 6.4 shows the  $1/f$  noise at these three fields. No difference can be observed in these regimes, demonstrating that in this structure there is no extra magnetic noise caused by the formation of magnetic domains at low frequency [15].



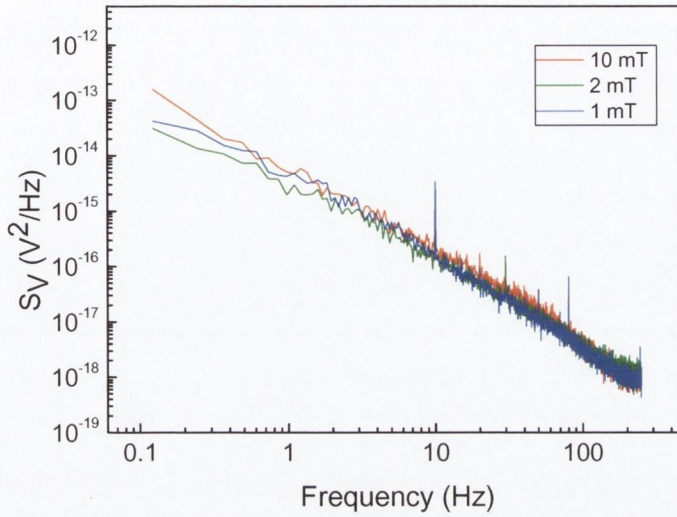


**Figure 6.4**  $1/f$  noise in a spin valve yoke at room temperature with a sensing current of 3 mA at different external applied fields.

### 6.2.3 Spin valve sensitivity

Sensor sensitivity is defined as the noise ( $V/\sqrt{Hz}$ ) divided by the slope of the magnetoresistance curve ( $V/T$ ) and is quoted in  $T/\sqrt{Hz}$ . The first way to increase the sensitivity is to increase the voltage output by increasing the current through the device. This is limited by the maximum power that the device can withstand. The second way is to increase the resistance of the sensor. This is done by increasing the length  $l$  while keeping the width the same. The thermal noise is proportional to the square root of the resistance which, in the case of the yoke-type sensor, is proportional to the square root of the length to width ratio ( $\sqrt{l/w}$ ) of the yoke. The  $1/f$  noise is proportional to  $1/\sqrt{volume} \approx 1/\sqrt{wxl}$  for the yoke sensor. So overall, the best signal-to-noise ratio is obtained by maximising  $l$  and  $w$  depending on the frequency range of the application. If the ratio  $w/l$  becomes too high, typically larger than 0.2, the free layer reversal becomes

less stable with domain formation and hysteresis. The sensitivity of the spin valve yoke sensor in Figure 6.2 is  $0.4nT/\sqrt{Hz}$  at room temperature.

### 6.3 The principle of the mixed sensor device

In the mixed sensor, a sensitive spin valve sensor and a flux to field transformer are combined. The transformer is made of a superconducting loop containing a micrometer-size constriction. The field to be sensed is applied perpendicular to the plane of the loop. This field generates a supercurrent in the loop which tends to expel the flux from entering the superconductor as a result of the Meissner effect. The field lines due to the supercurrent are locally enhanced at the constriction (Figure 6.5), and their horizontal component can be detected by a spin valve placed above or below the constriction, according to the direction they give to the free layer magnetisation relative to the hard layer magnetisation.

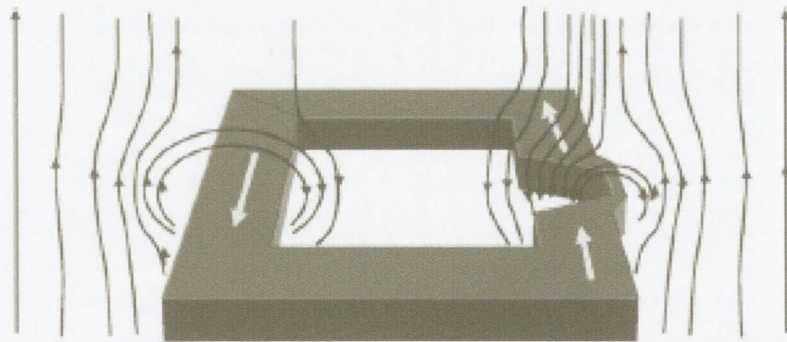


**Figure 6.5** Schematic of the superconducting loop when an external perpendicular field is applied. The supercurrent (white arrows) generates a high density of field lines with an in-plane component at the position of the constriction. The spin valve sensor is placed immediately above or below the constriction.



The device is shown in detail in Figure 6.6. The spin valve element of the device is patterned into an optimized yoke design as discussed in the previous section. In (A) the full device is shown where the spin valve yoke is placed over a constriction in the YBCO loop and four contacts for wire-bonding can be seen. The superconducting constriction and spin valve yoke are shown more clearly in the SEM micrograph (B). The yoke is 60  $\mu\text{m}$  long and 6  $\mu\text{m}$  wide. The constriction is 6  $\mu\text{m}$  wide and directly below the active, domain-free region of the yoke. When a field is applied perpendicular to the device, the in-plane component of the field generated by the loop can switch the magnetisation of the free layer of the spin valve (C). The spin valve is deposited in the crossed-anisotropy configuration with the free layer magnetisation aligned along the length of the yoke. The spin valve and its contacts are electrically isolated from the YBCO by a layer of insulating  $\text{Si}_3\text{N}_4$  as shown in the cross section (D).

The spin valve element of the mixed sensor device detects an in-plane field but the device as a whole is sensitive to perpendicular applied fields. The key point is the enhancement of the applied field by the superconducting flux-to-field transformer such that it can be detected by the spin valve. Flux-to-field transformation is often done with soft magnetic materials designed as flux concentrators but this incurs an extra intrinsic noise. The superconducting loop is the more elegant solution. In applications such as biomagnetism, the signals are much lower than the sensitivity of the spin valve itself. Heart signals, for example, are of the order of a few picotesla ( $10^{-12}$  Tesla). The loop therefore, needs to enhance the signal by a factor of a hundred to a thousand, depending on the spin valve and the application, in order for the device to be useful. Optimisation of the loop dimensions has been carried out using theoretical modelling and magneto-optical imaging [16], [17], [18]. This has shown that the maximum gain of the system is obtained by making the loop as large as possible with a width/radius ratio of 0.7 and by keeping the constriction width

as small as possible. Simulations also reveal that the maximum in-plane field is located immediately above or below the constriction, where the spin valve is placed, as depicted in the schematic in Figure 6.5.

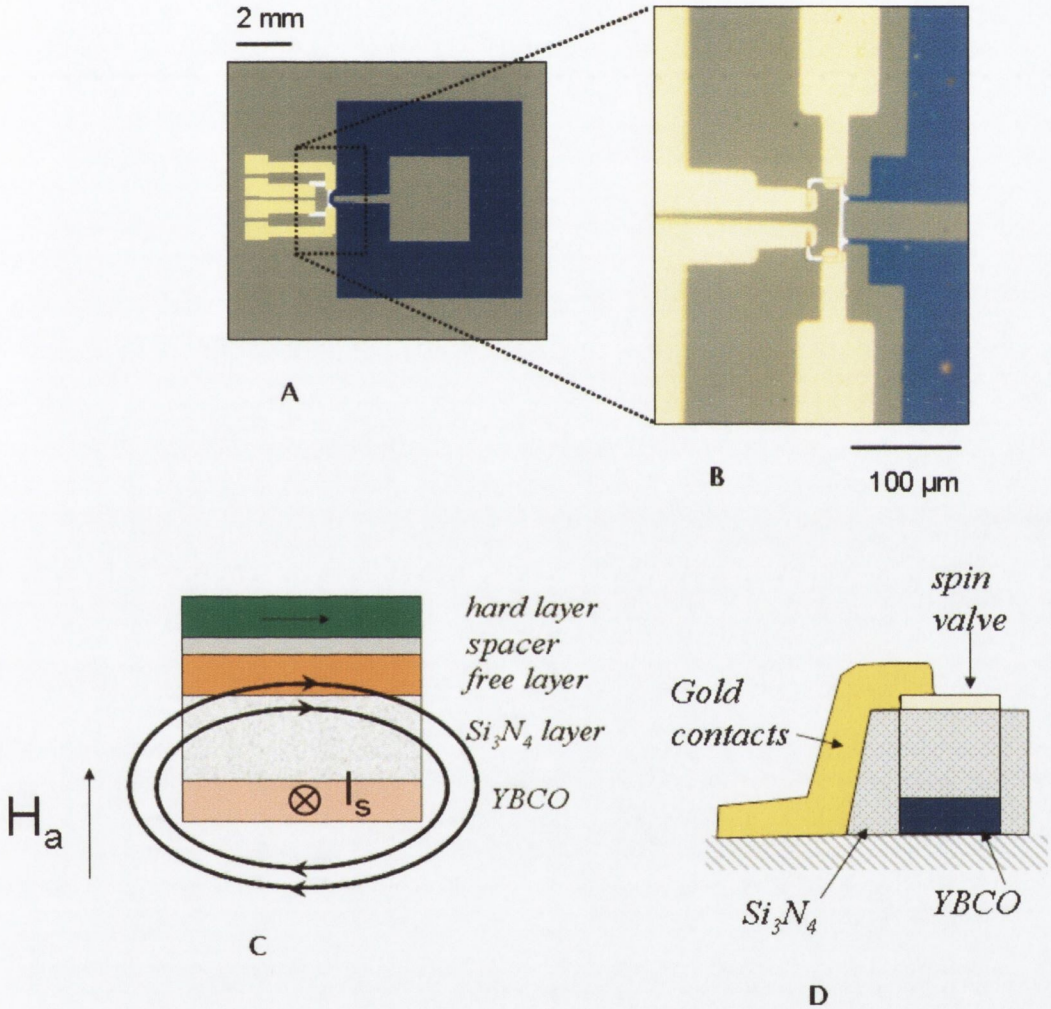


**Figure 6.6** Schematic views of YBCO mixed sensor device. (A) Schematic showing YBCO superconducting loop with yoke-shaped spin valve sensor and four contacts for measurement. (B) Optical micrograph of the constricted area of the loop under the active part of the spin valve. (C) Cross-section of the spin valve stack showing the in-plane components of the field created by the YBCO flux-to field transformer. (D) Cross-section of the device showing electrical isolation of the spin valve and the contacts from the loop by the Si<sub>3</sub>N<sub>4</sub> layer.

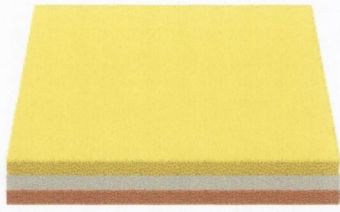


## 6.4 Sample preparation

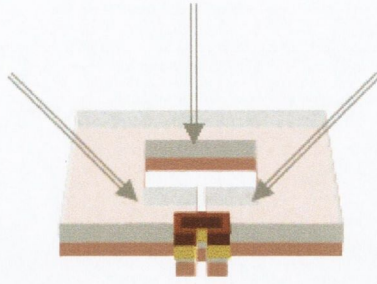
The first prototypes of the mixed sensor were made using the low- $T_c$  superconductor niobium as the superconducting loop material. The Nb devices were made using commercially available spin valve stacks [19]. Fabrication of the Nb devices was straightforward as the niobium loop could be deposited on top of a pre-defined spin valve yoke. In order to test the device at higher temperatures, sensors using the high  $T_c$  superconductor YBCO were designed. The higher  $T_c$  of YBCO also means that larger currents can be passed through the device and the noise levels can be reduced. YBCO, however, needs to be deposited epitaxially on a sapphire substrate in order to get the superconducting phase. For that reason, that spin valve stack needed to be deposited on top of the YBCO. Optimisation of this process was carried out at T.C.D.

The YBCO used is a commercial [20] 100nm thick layer, grown on sapphire, with a  $T_c$  of 88 K. A  $\text{Si}_3\text{N}_4$  insulating layer is sputtered on top of the YBCO and smoothed by polishing. The spin valve stack of structure:

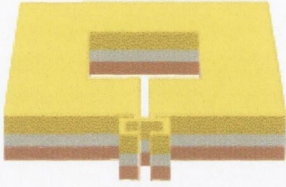
$\text{Ta}(5\text{nm})/\text{NiFe}(3.5\text{nm})/\text{CoFe}(1.2\text{nm})/\text{Cu}(2.9\text{nm})/\text{CoFe}(2.5\text{nm})/\text{IrMn}(10\text{nm})/\text{Ta}(10\text{nm})$  is deposited on top of the  $\text{Si}_3\text{N}_4$ . The device is then patterned using conventional optical lithography as shown in Figure 6.7. The entire pattern is first defined and etched down to the substrate. The pattern is defined with the free layer of the spin valve aligned with the length of the yoke. Photoresist is then removed from the loop but remains on the yoke. Another etching step removes the spin valve stack from the loop. Angular deposition of  $\text{Si}_3\text{N}_4$  at the edges follows for electrical insulation. The photoresist is then removed from the yoke and a standard lift-off procedure used to define the contacts.



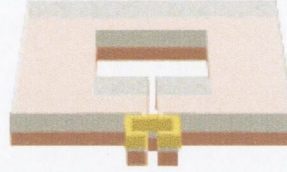
1 Deposition of spin valve stack on YBCO/Si<sub>3</sub>N<sub>4</sub>



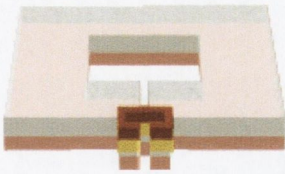
4 Angular deposition of Si<sub>3</sub>N<sub>4</sub> for edge passivation



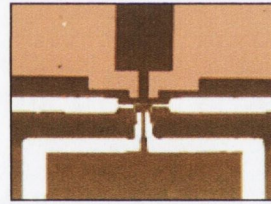
2 Definition of loop and yoke shape and dry etching of the whole structure



5 Removal of photoresist



3 Selective etching leaving spin valve only at yoke position



6 Deposition of contact pads by lift-off

**Figure 6.7 Schematic of patterning process for the YBCO-based mixed sensor device.**



### 6.5 Femtotesla resolution with an YBCO-spin valve mixed sensor

For measurement, the device is cooled down in a liquid helium cryostat, containing superconducting coils to generate a static bias field parallel to the substrate as well as a small copper coil at the back of the sample holder to generate a field perpendicular to the substrate. The MR response of the spin valve element is first measured at room temperature to ensure that the perpendicular field has no effect. The response of the spin valve is then calibrated in an in-plane field from room temperature down to 4.2 K. A constant in-plane field is applied during cooling in order to compensate the shift from zero of the spin valve and centre the response in the middle of the linear region. Figure 6.8 shows the magnetoresistance as a function of in-plane field at 4.2 K and Figure 6.9 the MR as a function of temperature down to 4.2 K. The MR increases from 4.5 % at room temperature to 9 % at 4.2 K. In the linear part of the MR curve, the slope at 4.2 K is 3.11 % per mT.

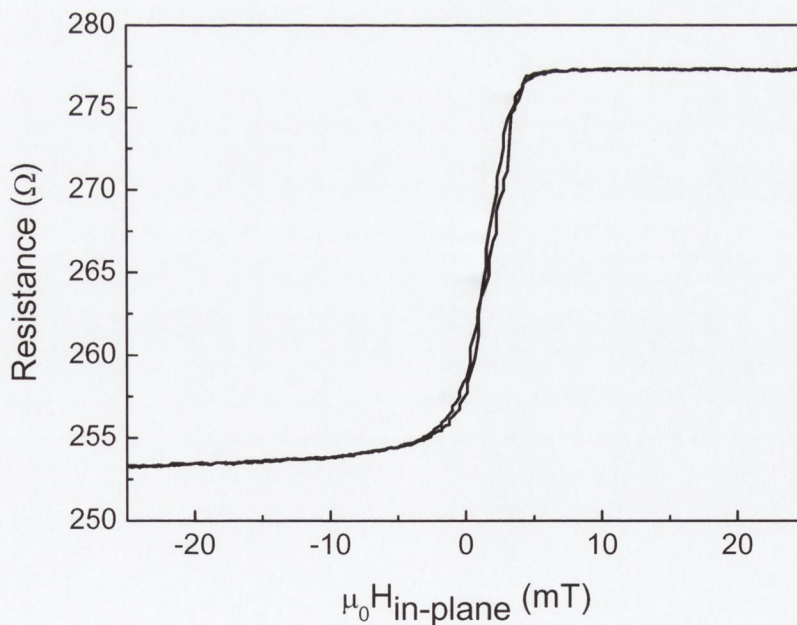


**Figure 6.8** Magnetoresistance of the spin valve yoke of an YBCO-based mixed sensor at 4.2 K.

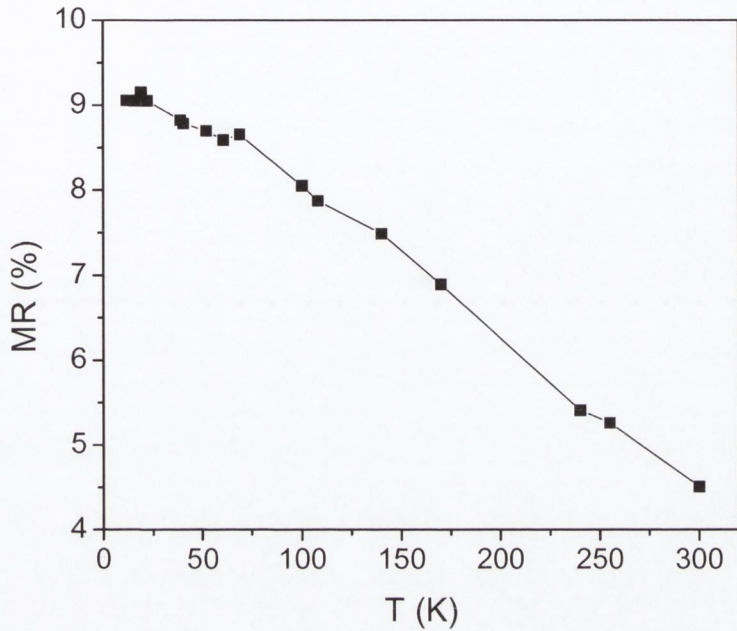


**Figure 6.9 Magnetoresistance ratio as a function of temperature.**

At 4.2 K, a perpendicular field is then applied to the device. With the YBCO now in the superconducting state, this field creates an in-plane, locally enhanced field above the constriction which switches the free layer of the spin valve. The MR variation on the YBCO device as a function of the perpendicular applied field is shown in Figure 6.10. As the perpendicular field is increased, the MR of the spin valve changes due to the rotation of the free layer. The upper plateau in Figure 6.10 corresponds to the saturation of the spin valve with free and pinned layers antiparallel and the lower plateau corresponds to free and pinned layer parallel. From the variation in the MR, we can see that the entire response of the spin valve is explored. At 4.2 K, this can be done without reaching the critical current of the YBCO. The critical current of the superconductor is reached shortly after the saturation of the spin valve. The maximum slope variation in resistance of the YBCO device at 4.2 K is 310 % per mT. When compared with the in-plane spin valve response at



the same temperature (Figure 6.8) which is 3.11% per mT, the gain of the device is calculated to be close to 100.

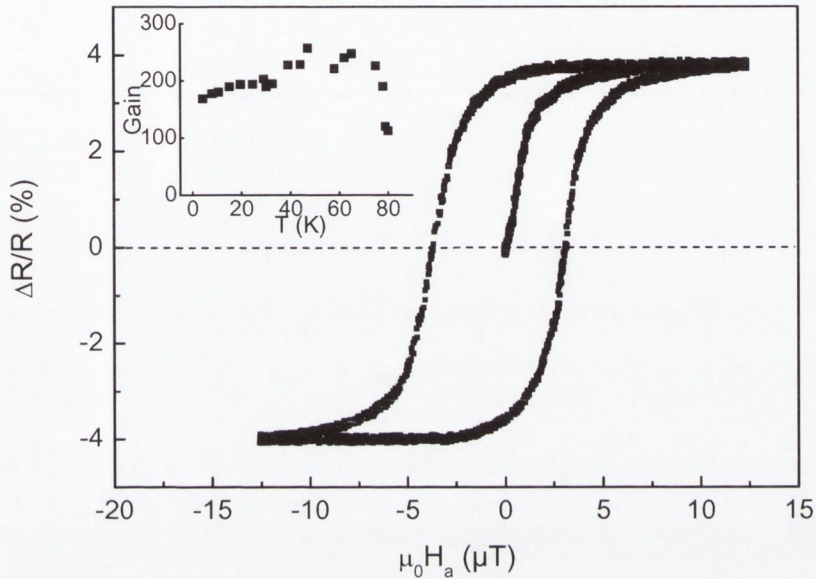


**Figure 6.10** Magnetoresistance as a function of perpendicular applied field at 4.2 K on the YBCO device. The inset shows the gain as a function of temperature.

The measurement of the intrinsic noise of the mixed sensor is difficult as the thermal noise is about  $0.1nV/\sqrt{Hz}$  and the noise of the preamplifier is about  $1nV/\sqrt{Hz}$ . For this reason, the mixed sensor was coupled to positive feedback circuit. A similar technique is used in the read out of DC SQUIDS [21]. The positive feed back circuit consists of a copper wire coil connected to a voltage source in series with the spin valve. A change in resistance of the spin valve in the presence of an applied out-of-plane field creates a current through the feedback circuit. The current through the copper coil creates an additional field that amplifies the gain of the sensor. The amplification is tuneable by the voltage source [9]. The noise spectra of the YBCO device recorded at 4.2 K and 77 K as shown in Figure

6.11. At 4.2 K, a higher current can be passed through the device, thereby reducing the  $1/f$  noise of the spin valve. At 4.2 K and with a 15mA sensing current the sensitivity level of the device is  $32 \text{ fT} / \sqrt{\text{Hz}}$ . This is comparable to the performance of high- $T_c$  SQUIDS.

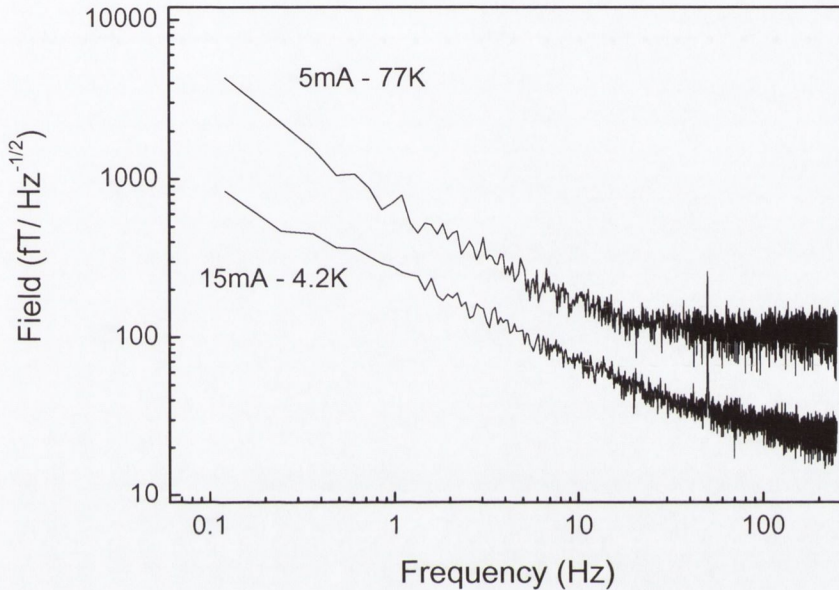


**Figure 6.11** Noise spectra of the YBCO mixed sensor at 4.2K and 77K with 15 mA and 5 mA of sensing current respectively.

### 6.6 Femtotesla resolution with a Nb-spin valve mixed sensor

For comparison, the response of a Niobium mixed sensor made with a commercially available spin valve is shown in Figure 6.12. As the perpendicular field is increased, the MR of the spin valve changes as the free layer rotates. However, in this case, the critical current of the Nb is reached before the spin valve reaches full parallel or antiparallel alignment. The inset of Figure 6.12 shows the response of the sensor as a function of temperature. The point at which the response becomes zero (6.5 K) is a measure of the critical temperature of the Nb constriction. The slope of this device corresponds to a



resistance variation of 213 % per mT as compared with 2 % for an in plane field at the same temperature leading to a gain of 108. The noise spectrum of the device at 4.2 K is shown in Figure 6.13. With a sensing current of 1 mA, the sensitivity of the device is  $540 \text{ fT} / \sqrt{\text{Hz}}$ .

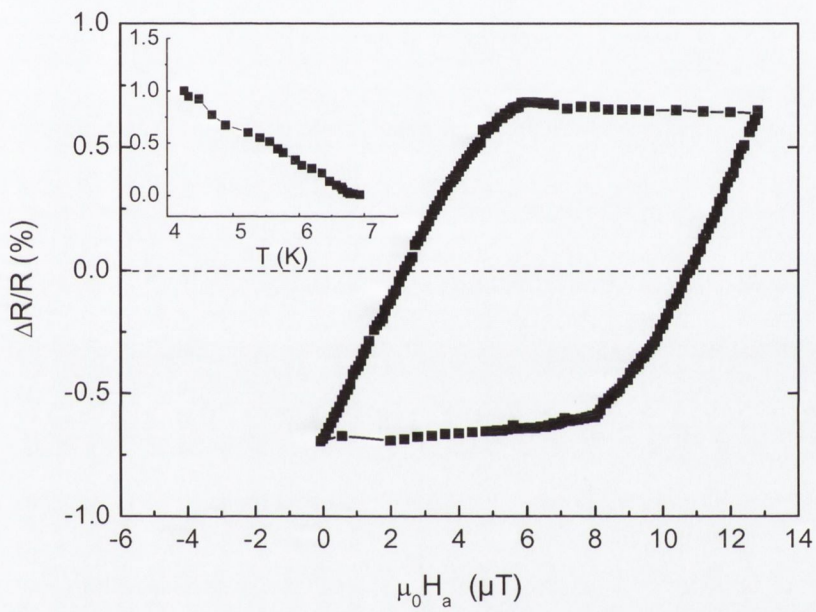


**Figure 6.12** Magnetoresistance as a function of perpendicular applied field at 4.2 K for the Nb based mixed sensor.

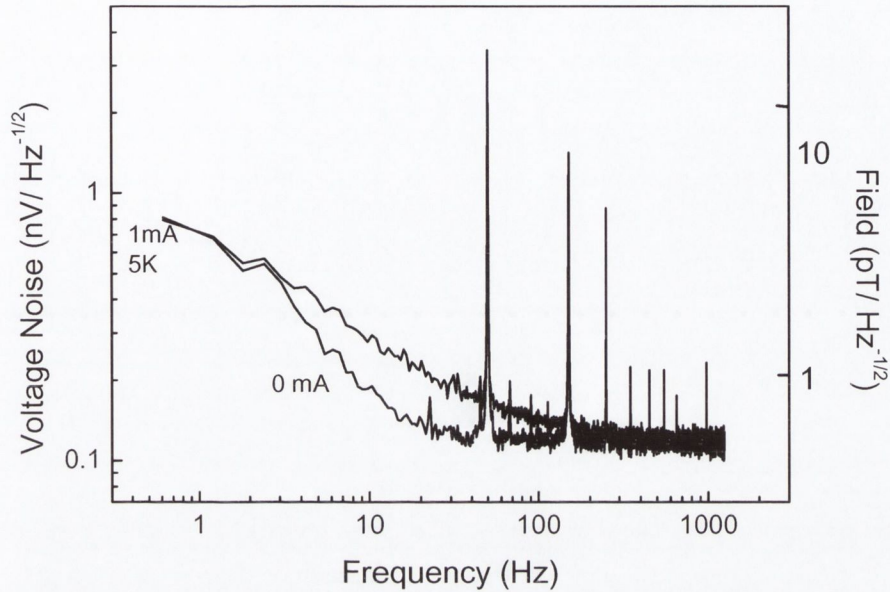


**Figure 6.13** Noise spectra of the Nb device at 5 K with 0 mA and 1 mA sensing current.

## 6.7 Conclusion

Sensitivities of  $32fT/\sqrt{Hz}$  have been demonstrated with the YBCO mixed sensor at 4.2 K. Performance of the device depends on the local enhancement of the applied field by the flux-to-field transformer and on the sensitivity of the sensing element. Performance can be improved by optimizing the dimensions of the superconducting loop. In particular, a gain of 4000 can theoretically be achieved with a 25 mm loop and a 1  $\mu\text{m}$  constriction. These dimensions are achievable with standard lithography techniques. With a spin valve element and this optimized loop, sensitivities could reach  $1fT/\sqrt{Hz}$  thermal noise at 77 K.



In order to improve the sensitivity of the magnetoresistive element of the mixed sensor, a magnetic tunnel junction (MTJ) could be implemented. The MTJ consists of two ferromagnetic layers separated by thin insulating layer acting as a tunnel barrier. Current is passed perpendicular to the plane in this device and tunneling magnetoresistance (TMR) ratios of up to 70 % are obtained with  $\text{Al}_2\text{O}_3$  barriers [22]. In the last year, magnetic tunnel junctions with MgO barriers have been reported with TMR ratios of over 200 % at room temperature [23]. These structures would vastly increase the device sensitivity. The possible drawback of the MTJ is that although sensitivity is higher, smaller currents must be used to avoid breakdown of the barrier layer resulting in higher noise levels. Ultimately, one might use TMR sensors with half metallic electrodes. This kind of system, based on manganite compounds, exhibits low field magnetoresistance of 1800 % at 4.2 K [24], [25]. They can be epitaxially grown on high  $T_c$  films, producing a high-quality film. With the proper substrate, manganite films with extremely low  $1/f$  noise have been produced [26]. These TMR systems should be good candidates to reach the subfemtotesla range with the mixed sensor.

The first prototypes of the YBCO mixed sensor have demonstrated femtotesla resolution placing them in competition with high- $T_c$  SQUIDs. Further optimisation of the device, possibly with the use of magnetic tunnel junctions, should leave it well placed as a subfemtotesla magnetic field sensor with a range of application in the fields of biomagnetism and magnetometry.

## 6.8 References

---

- [1] R. Salmelin, R. Hari, O.V. Lounasmaa, M. Sams, *Nature*, **368**, 463 (1994).
- [2] C. Del Gratta, V. Pizzella, F. Tecchio, G.L. Romani, *Rep. Prog. Phys.* **64**, 1759 (2001).
- [3] H. Weinstock, *SQUID Sensors : Fundamentals. Fabrication and Applications*. Kluwer Academic, Dordrecht, Netherlands (1996).
- [4] V. Pizzella, S.D. Penna, C.D. Gratta, G.L. Romani, *Supercond. Sci. Technol.* **14**, R79 (2001).
- [5] J. Gallop, B.W. Petley, *Supercond. Sci. Technol.* **16**, 1575 (2003).
- [6] H.J. Barthelmeß, B. Schiefenhövel, M. Schilling, *Physica C*, **368**, 37 (2002).
- [7] H.J. Barthelmeß, M. Halverscheid, B. Schiefenhövel, E. Heim, M. Schilling, R. Zimmermann, *IEEE Trans. Appl. Superconduct.* **11**, 657 (2001).
- [8] S. Krey, H.J. Barthelmeß, M. Schilling, *J. Appl. Phys.* **86(11)**, 6602 (1999).
- [9] M. Pannetier, C. Fermon, G. Le Goff, J. Simola, E. Kerr, *Science* **304**, 1648 (2004).
- [10] I.K. Kominis, T.W. Kornack, J.C. Allred, M/V. Romalis, *Nature* **422**, 596 (2003).
- [11] S. Linzen, F. Schmidt, F. Schmidl, M. Mans, O. Hesse, F. Nitsche, G. Kaiser, S. Müller, P. Seidel, *Physica C*. **372**, 146 (2002).
- [12] S. Schmidt, S. Linzen, F. Schmidl, M. Mans, P. Seidel, *Supercond. Sci. Technol.* **15**, 488 (2002).
- [13] C. Fermon, M. Pannetier, N. Biziere, B. Cousin, *Proc. EMSA* (2005).
- [14] <http://math.nist.gov/oommf/>
- [15] M. Pannetier, C. Fermon, G. Le Goff, J. Simola, E. Kerr, J.M.D. Coey, J. Magn. *Magn. Mater.* **290**, 1158 (2005).
- [16] M. Pannetier, C. Fermon, P. Védérine, M.S. Welling, R.J. Wijngaarden, *Proc. EMSA Conf.*, Cardiff, U.K. (2004).



- 
- [17] M. Pannetier, C. Fermon, G. Le Goff, J. Simola, E. Kerr, M.S. Welling, R.J. Wijngaarden, *IEEE, Trans. Appl. Superconduct.* **15**, 892 (2005).
- [18] M. Pannetier, C. Fermon, G. LeGoff, E.Kerr, *Proc. EMSA Conf., Cardiff, U.K., Jul.* (2004).
- [19] Spin valves were commercially available from IPHT (Jena, Germany).
- [20] Commercial YBCO films were deposited by Theva GmbH, Germany.
- [21] H. Seppä, A. Ahonen, J. Knuutila, J. Simola, V. Vilkmán, *IEEE Trans. Magn.* **27**, 2488 (1991).
- [22] D. Wang, C. Nordman, J.M. Daughton, Z. Qian, J. Fink, *IEEE Trans. Mag.* **40**, 2269 (2004).
- [23] S.S.P. Parkin, C. Kaiser, A. Panchula, P.M. Rice, B. Hughes, M. Samant, S. Yang, *Nature Mat.* **3**, 862 (2004).
- [24] M. Viret, M. Drouet, J. Nassar, J.P. Contour, A. Fert, *Europhys. Lett.* **39(5)**, 545 (1997).
- [25] M. Bowen, M. Bibes, A. Barthélémy, J.P. Contour, A. Anane, Y. Lemaître, A. Fert, *Appl. Phys. Lett.* **82(2)**, 233 (2003).
- [26] P. Reutler, A. Bensaïd, F. Herbstritt, C. Höfener, A. Marx, R. Gross, *Phys. Rev. B.* **62**, 11619 (2000).

## Chapter 7

### Conclusions and Future Work

Several aspects of spin valve structures have been addressed in this thesis. The deposition of spin valve films has been developed and optimised using DC magnetron sputtering in a Shamrock deposition system. IrMn top-pinned spin valves of structure Ta(5nm)/NiFe(3.5nm)/CoFe(1.2nm)/Cu(2.9nm)/CoFe(2.5nm)/IrMn(10nm)/Ta(5nm) have been developed with GMR values of up to 8 %. Polarised neutron reflectometry has been used to characterise the structure and measure the individual layer thicknesses and magnetic moments. These were found to be in good agreement with the nominal values. Analysis of the neutron spin-flip signal allowed the stability of the pinned layer to be examined as a function of applied field and temperature. This revealed that when small fields are applied perpendicular to the easy axis of the pinned layer, some of the CoFe rotates towards the direction of the field. This can be due to inhomogeneous pinning across the CoFe layer. The blocking temperature of the IrMn film is 200 °C, as estimated from the decrease of the spin flip signal with temperature. This is lower than expected for IrMn spin valves and limits the high temperature application of the structure. The long term thermal stability of the spin valve was investigated by measuring the reflectivity over



time at elevated temperatures. No changes in reflectivity were observed after prolonged heating at 185 °C and we conclude that the spin valve has not suffered any significant structural changes at this temperature. Further work in this area should include a characterisation of spin valves with a synthetic antiferromagnet. Similar experiments investigating the stability of the pinned layer with temperature and field would allow a direct comparison between SAF and standard spin valves for sensor applications. The SAF is expected to be more thermally stable and more resistant against externally applied fields. The behaviour of the magnetic layers in the SAF could be monitored with high precision using PNR.

The effects of post-deposition magnetic annealing on spin valves have been investigated. Standard top and bottom spin valves and spin valves with a synthetic antiferromagnet have been annealed at temperatures ranging from 180 °C to 300 °C in fields ranging from 0.05 T to 5.5 T. It was found that the exchange bias of the IrMn bottom-pinned spin valves was enhanced by annealing in a large magnetic field. The annealing field effects for the IrMn bottom-pinned spin valves are attributed to a realignment of the pinned interfacial spins in the IrMn layer. The application of a large magnetic field during cooling increases the component of the pinned interfacial moment along the field direction and this results in a larger exchange bias. For IrMn top-pinned spin valves and spin valves with a synthetic antiferromagnet no clear magnetic field effects were measured. For top-pinned spin valves the study on annealing field effects is complicated by a thermal deterioration of the magnetotransport properties during annealing and for spin valves with a synthetic antiferromagnet the pinning strength does not depend largely on the spin structure in the IrMn layer and is determined by the coupling across the thin Ru layer. In order to continue this work, the bottom SAF structures should be optimized further through the use of a NiFe

buffer layer under the IrMn. This would promote (111) texture in the free layer leading to lower coercivity and independent switching of the free and pinned layers.

The effects 30 keV Ga<sup>+</sup> implantation on top-pinned IrMn spin valves have been investigated. Direct implantation of Ga<sup>+</sup> ions at doses less than 10<sup>14</sup> ions/cm<sup>2</sup> results in a gradual decrease of GMR which is partly due to a deterioration of the exchange bias. Implantation at higher doses causes a large increase in the film resistance and a substantial deterioration of GMR. At this point the magnetic properties of the system have been seriously and irreversibly degraded by the creation of defects in the entire spin valve stack. The suitability of FIB milling for the fabrication of small magnetic elements was studied by reducing the width of 10 μm spin valve lines. Here the GMR and the exchange bias field decreased rapidly with decreasing line width. The degrading effects are stronger than expected from 30 keV Ga<sup>+</sup> ion implantation from the sides and suggest that the spin valves are simultaneously implanted from the top. From these results we conclude that direct FIB milling without an appropriate mask should not be used for the fabrication of micron and sub-micron size spin valves. In future, implanted samples should be assessed using techniques such as transmission electron microscopy (TEM) and secondary ion mass spectroscopy (SIMS) in order to determine the Ga<sup>+</sup> ion distribution within the spin valves. The use of a hard mask such as SiO<sub>2</sub>/Au should be investigated for the fabrication of sub-micron spin valves. Spin valves fabricated in this manner could then be compared with those patterned using electron beam lithography.

Finally, spin valves have been implemented in a novel application, the mixed sensor. This sensor combines a superconducting loop with a micron sized constriction and a spin valve. A perpendicular field creates a supercurrent in the loop which creates a locally enhanced in-plane field at the constriction. This field can be detected by a spin valve placed above



or below the constriction. The spin valve element of the sensor has been optimized for a low noise linear response, with low hysteresis. A process for depositing spin valves on YBCO/Si<sub>3</sub>N<sub>4</sub> films has been developed using the Shamrock deposition tool. A prototype YBCO/spin valve mixed sensor has been demonstrated and exhibits a resolution of  $32 fT / \sqrt{Hz}$ . This is comparable to the noise level of high T<sub>c</sub> SQUIDs. This sensor is suitable for application in several areas including magnetometry and biomagnetism. Future improvements in sensitivity of the sensor can be envisaged through replacement of the spin valve element of the sensor with a magnetic tunnel junction.

## Publications

1. *Ultra-sensitive field sensors - an alternative to SQUIDS*

M. Pannetier, C. Fermon, G. Le Goff, J. Simola, E. Kerr, M. Welling, R.J. Wijngaarden, IEEE Trans. Appl. Supercond. **15(2)**, 892 (2005).

2. *Effects of Ga<sup>+</sup> ion implantation on the magnetoresistive properties of spin valves*

E. Kerr, S. van Dijken, R.M. Langford, J.M.D. Coey, J. Magn. Magn. Mater. **290**, 124 (2005).

3. *Influence of the annealing field strength on exchange bias and magnetoresistance of spin valves with IrMn*

E. Kerr, S. van Dijken, J.M.D. Coey, J. Appl. Phys. **97(9)**, 093910 (2005).

4. *Noise in magnetic systems - applications to very sensitive magnetoresistive sensors*

M. Pannetier, C. Fermon, G. Le Goff, J. Simola, E. Kerr and J.M.D. Coey, J. Magn. Magn. Mater. **290**, 1158 (2005).

5. *Femtotesla Magnetic Field Measurement with magnetoresistive sensors*

M. Pannetier, C. Fermon, G. Le Goff, J. Simola, E. Kerr, Science **304**, 1648 (2004).